Technische Universität München
Max-Planck-Institut für extraterrestrische Physik
Garching bei München

Elemental Abundances in the Intra-Cluster Medium and in Active Galactic Nuclei

Italo Balestra

Vollständiger Abdruck der von der Fakultät für Physik der Technischen Universität München zur Erlangung des akademischen Grades eines

Doktors der Naturwissenschaften

genehmigten Dissertation.

Vorsitzender:		Univ.-Prof. Dr. A. J. Buras
Prüfer:	1.	Hon.-Prof. Dr. G. Hasinger
	2.	Univ.-Prof. Dr. St. Paul

Die Dissertation wurde am 12.10.2007 bei der Technischen Universität München eingereicht und durch die Fakultät für Physik am 12.11.2007 angenommen.

Summary

In this thesis, we use the X-ray telescopes *Chandra* and XMM-*Newton* for the study of elemental abundances of the two most powerful X-ray emitters in the Universe: the intra-cluster medium (ICM), permeating clusters of galaxies, and active galactic nuclei. We aim at tracing the evolution in the chemical composition of these objects in order to derive conclusions on the past history of the accumulation of metals in the Universe. We find significant evidence of a decrease in the average Fe content of the ICM as a function of redshift, implying an evolution of more than a factor of 2 from $z \simeq 0.4$ to $z \simeq 1.3$. We find indications for solar or twice solar metallicities from photoionization models in two X-ray bright, nearby, Narrow-Line Seyfert 1 galaxies, confirming results based on optical/UV diagnostics.

Zusammenfassung

In dieser Arbeit verwenden wir Daten der Teleskope Chandra und XMM-Newton für die Studie der Elementhäufigkeiten in den zwei stärksten Röntgenstrahlungsquellen im Universum: das Intra-Cluster Mittel (ICM), und aktive Galaxienkerne. Unser Ziel ist die Entwicklung der chemischen Zusammensetzung dieser Objekte zu verfolgen, und daraus die Geschichte der Anreicherung der Metalle im Universum abzuleiten. Wir finden signifikante Hinweise auf eine Abnahme des durchschnittlichen Eisengehalts des ICM als Funktion der Rotverschiebung. Im Intervall $z \simeq 0.4$ bis $z \simeq 1.3$ fällt der Eisengehalt um mehr als die Hälfte ab. In zwei nahe gelegen Narrow-Line Seyfert 1 Galaxien, die starke Röntgenemission aufweisen, finden wir mit Hilfe von Fotoionisationsmodellen Anzeichen für Metallizitäten die ein bis zwei mal den Sonnenwert betragen. Damit bestätigen wir die Resultate der optischen und UV-Verfahren.

Elemental Abundances in the Intra-Cluster Medium and in Active Galactic Nuclei

Italo Balestra

01/09/2007

Contents

Chapter 1

Preface

Several types of astrophysical objects emit X-rays, from galaxy clusters, through black holes in active galactic nuclei (AGN) to galactic objects such as supernova remnants, stars, and binary stars containing a white dwarf (cataclysmic variable stars), neutron star or black hole (X-ray binaries). However, the most powerful extragalactic X-ray sources in the sky are clusters of galaxies and AGN, which can reach total X-ray luminosities of about 10^{46} erg s^{-1} for the brightest clusters of galaxies and up to 10^{48} erg s^{-1} in the case of the brightest AGN.

Clusters of galaxies are the largest virialized structures in the universe, which are formed by subsequent mergers of smaller scale structures, such as galaxy groups or individual galaxies. The infalling material, which contains cold baryons in form of galaxies and hot baryons in form of gas, gains kinetic energy as it falls into the cluster's gravitational potential well, traced by the dark matter distribution. The infalling gas collides with that already present and is shock heated to temperatures of about $10^7 - 10^8$ K, depending on the size of the cluster. This very hot gas, which constitutes the hot intra-cluster medium (ICM), emits X-rays by thermal bremsstrahlung and line emission from several *metals*[1] (see also Appendix A).

Active galactic nuclei are galaxies whose central region (i.e. $\lesssim 1\,pc^3$) is observed to outshine all the stars in the galaxy itself (i.e. $\sim 10^{11}\,L_\odot$). The only viable explanation and the current paradigm for the extreme AGN luminosities is accretion of matter onto a super-massive black hole. What powers AGN is the convertion of mass into energy. Energy is generated by gravitational infall of material which is heated to high temperatures in a dissipative accretion disk, where viscous forces act as friction, resulting in the dissipation of heat and consequently in the emission of radiation. The viability of accretion as a source of energy relative to other mechanisms (such as nuclear processes) depends on the efficiency η of conversion of mass to energy ($L = dE/dt = \eta\, dM\, c^2/dt = \eta \dot{M} c^2$). The potential energy of a mass m at a distance r to the central source of mass M is $U = GMm/r$, and the rate at which the potential energy of infalling matter can be converted to radiation is $L \approx dU/dt = GM\, dm/r\, dt = GM\dot{M}/r$. Therefore $\eta \propto M/r$, which is a measure of the "compactness" of the central source and which is maximized in the case of a black hole.

In this thesis, we exploit the different capabilities of the two X-ray telescopes *Chandra* and XMM-*Newton* for the study of elemental abundances of the two most powerful X-ray emitters in the Universe: the hot intra-cluster medium permeating clusters of galaxies and AGN. We aim at tracing the evolution in the chemical composition of these objects in order to derive conclusions on the past history of the accumulation of metals in the Universe.

The study of the elemental abundances of the ICM is aimed at tracing the evolution of its content of metals with cosmic time, investigating at the same time the dependency of the *metallicity*[2] with temperature.

In the study of the metal abundances of AGN, we focus on the local Universe to trace the evolution of metals as a function of the accretion rate, which may follow the history of mass accretion of super-massive black holes in the center of galaxies. In particular, we study the properties of narrow line Seyfert 1 galaxies (NLS1), a subclass of AGN which is believed to be powered by accretion of matter at high rates onto super-massive black holes of relatively small masses and which shows typically higher metal abundances compared to objects accreting mass at lower rates.

[1] As it is customary in astrophysics, throughout this work, will refer to any element other than hydrogen and helium as a *metal*.

[2] The abundance of a certain *metal* is referred to as its *metallicity*.

Figure 1.1: Artist's impressions of the two X-ray telescopes *Chandra* (*left*) and XMM-*Newton* (*right*).

1.1 Modern X-ray telescopes

In the last 40 years a number of X-ray instruments have been launched above the atmosphere (which is opaque to X-rays) to study X-ray sources. X-ray telescopes typically reflect X-rays at grazing incidence using mirrors coated with a high-Z[3] material. The modern X-ray telescopes use charged-couple devices (CCD) to record the positions of X-ray photons and obtain low resolution energy measurements. Reflection and transmission gratings are instead used to disperse X-rays and achieve higher resolution spectroscopy.

Since 1999, after the launch in orbit of the two X-ray telescopes *Chandra* and XMM-*Newton*, extraordinary improvements were brought in the field of X-ray astronomy.

Chandra, thanks to its superior spatial resolution ($\sim 0.5''$), has represented a giant leap forward with respect to previous X-ray missions. Still providing the best X-ray images at a sub-arcsec resolution, *Chandra* has allowed to detect otherwise undetected structures and features in the spatial extent and distribution of the X-ray emitting sources or to study extremely faint sources in crowded fields.

XMM-*Newton*, instead, thanks to a much larger effective area, is capable of obtaining higher quality spectra and therefore to allow for a more detailed spectral analysis. In addition, the reflection gratings spectrometers (RGS) provide an excellent instrument for high-resolution spectroscopy, also in the case of relatively faint sources.

Below, we first discuss and compare some of the important characteristics of the two X-ray telescopes and the relevant instrumentation that is used in this thesis. Then, we discuss the analysis techniques that are used to interpret the data collected from these satellites.

1.1.1 *Chandra* and XMM-*Newton*: an overview

In this section we briefly summarize and compare the main characteristics of *Chandra* and XMM-*Newton* in order to give an insight into the capabilities of the two X-ray telescopes.

The main constituents of an X-ray telescope are the focusing mirrors and the X-ray detectors. The mirrors, which are usually coated with a high-Z material, reflect X-rays at grazing incidence angle and focus them on a detector. Modern X-ray detectors are semiconductor detectors, (i.e. charge-coupled devices, CCD), where radiation is measured by means of the number of charge carriers set free by the passage of an X-ray photon. Ionizing radiation produces free electrons and holes. The number of electron-hole pairs is proportional to the energy transmitted by the radiation to the semiconductor. As a result, a number of electrons are transferred from the valence band to the conduction band, and an equal number of holes are created in the valence band. Under the influence of an electric field, electrons and holes travel to the electrodes, where they result in a pulse that can be measured. As the amount of energy required to create an electron-hole pair is known, and is independent of the energy of the incident radiation, measuring the number of electron-hole pairs allows the energy of the incident radiation to be found.

Furthermore, reflection and transmission gratings allow to disperse X-rays by a constructive periodic surface where the X-ray wave will interfere constructively for a given angle of incidence. Both the reflection

[3]Here, by high-Z material we refer to a high atomic number material.

Table 1.1: X-ray Telescope Mirrors.

Mirror characteristic	ROSAT	ASCA	Chandra	XMM
Aperture diameter [cm]	83	40 (1 module)	120	70 (1 module)
Mirrors	4 nested	118 nested (1 module)	4 nested	58 nested
Geometric area [cm^2]	1140	1400 (2 modules)	1100	6000 (3 modules)
Effective area at 1 keV [cm^2]	350	400	800	4650
Grazing angles [$'$]	83-135	21-45	27-51	18-40
Focal length [m]	2.4	3.8	10	7.5
Mirror coating	Au	Au	Ir	Au
Highest energy focused [keV]	2	12	10	10
On axis resolution [$''$]	4	75	0.5	15

Table 1.2: Overview of Chandra and XMM characteristics of different detectors.

Detector characteristic	EPIC MOS	EPIC pn	RGS	ACIS-I	ACIS-S
Bandpass [keV]	$0.15-12$	$0.15-15$	$0.35-2.5$	$0.1-10$	$0.1-10$
Field of view [$'$]	30×30	30×30	5×5	16.9×16.9	8.3×50.6
PSF (FWHM/HEW) [$''$]	5/14	6/15	N/A	0.2/0.5	0.2/0.5
Pixel size [μm ($''$)]	40 (1.1)	150 (4.1)	81	24 (0.492)	24 (0.492)
Spectral resolution at 1 keV	$\sim$70 eV	$\sim$80 eV	$\sim$0.04 Å	$\sim$60 eV	$\sim$110 eV

grating spectrometers (RGS) on board XMM-*Newton*, and the high and low energy transmission gratings (HETG and LETG) on board *Chandra* can be used to obtain high resolution X-ray spectra.

In Table 1.1 the mirror characteristics of four different X-ray telescopes (i.e. ROSAT, ASCA, Chandra and XMM) are compared, while in Table 1.2 we give an overview of the principal characteristics of *Chandra* and XMM-*Newton* X-ray detectors. Here, we mention some of the most important characteristics in order to make a direct comparison between the capabilities of the two X-ray satellites:

Spectral Resolution: the spectral resolution or resolving power ($\lambda/\Delta\lambda$ or $E/\Delta E$) affects the ability to extract useful information from the spectrum. CCD devices typically have resolving powers near 10 or 20 at 1 keV. Dispersive instruments, such as those using a grating, have achieved a higher spectral resolution. The RGS instruments achieve high resolving power (150 to 800) over a range from 5 to 35 Å (0.33 to 2.5 keV), in the first spectral order.

Angular Resolution: Angular resolution is an important factor for spatially-resolved spectroscopy. XMM-*Newton* (with FWHM of $6''$ for the pn) and *Chandra* (with FWHM of $0.5''$), for example, have been able to perform spatially-resolved photometry on kiloparsec scales for nearby clusters of galaxies.

Effective Area and Exposure Time: The effective collecting area and the exposure time of the observation determine the number of photons collected. The larger effective area is that of the EPIC cameras on board XMM-*Newton* (4650 cm^2 at 1 keV). The effective area for dispersive instruments is smaller, for the RGS it peaks around 15 Å (0.83 keV), for the first order, at about 150 cm^2 for the two spectrometers (R1 and R2).

1.1.2 Analysis Techniques

X-ray photons that are recorded in detectors after being reflected and dispersed by optics have three quantities that are measured: two detector coordinates, x and y and one energy measurement p[4]. These

[4]The arrival time t is also recorded. However, unless it is necessary to study spectra that are variable in time, we can consider the spectrum integrated over the total exposure time of the observation.

are indirectly related to the position of the photon on the sky ϕ and ψ and the photon's intrinsic energy e. For dispersive spectrometers the relationship between these three variables and their detector counterparts are very indirect and the full convolution has to be considered. For non-dispersive spectrometers, the relationship is more direct so approximations can be used. For example, it is customary to assume that $(x, y) \approx (\phi, \psi)$ when extracting a spectrum to perform spatially-resolved spectro-photometry or to assume that $p \approx e$ to construct an image.

The detection probability D for a photon emitted from solid angle position $\mathbf{\Omega}$ and energy e with measured values of detector coordinates (x, y) and CCD pulseheight p is given by

$$D(x, y, p) = \int de\ d\Omega\ R(x, y, p \mid e, \mathbf{\Omega})\ \frac{d^2F(e, \Omega)}{d\Omega de} \tag{1.1}$$

where $\frac{d^2F}{d\Omega de}$ is the spatially-varying spectral source model and R is the instrument response function. The approach normally used is to simplify the response function above by assuming the following separation,

$$R(x, y, p \mid e, \phi, \psi) \sim R_M(p \mid e)A(e) \tag{1.2}$$

where R_M is the response matrix and A is the ancillary response.

The response matrix $R_M(p \mid e)$ maps the energy space (e) into detector pulse height space (p). Since detectors are not perfect, this involves a spreading of the observed counts by the detector resolution, which is expressed as a matrix multiplication.

The ancillary response $A(e)$ contains the combined telescope/filter/detector areas ("effective area") and the quantum efficiency as a function of energy averaged over time. When the input spectrum is multiplied by the ancillary response, the result is the distribution of counts that would be seen by a detector with perfect (i.e. infinite) energy resolution. The response matrix is then needed to produce the final observed spectrum.

The response matrix and an ancillary response file are used in spectral codes like XSPEC (Arnaud 1996). These codes multiply a source spectrum on a grid by the response matrix, which relates the input spectrum to the model observed spectrum. The model observed spectrum can be compared to the real data by statistical tests, typically a binned χ^2 calculation or Cash statistics applied to the unbinned data, which is preferable for small number of counts (Nousek & Shue 1989).

Chapter 2

Chemical enrichment of the intra-cluster medium

2.1 Introduction

Clusters of galaxies are the largest virialized structures in the Universe arising from the gravitational collapse of rare high peaks of primordial density perturbations (e.g. Peebles 1993; Coles & Lucchin 1995; Peacock 1999; Rosati et al. 2002; Voit 2005). As a result of adiabatic compression and shocks generated by supersonic motion during shell crossing and virialization, a hot ($\sim 10^7$ K) thin ($\sim 10^{-3}$ cm^{-3}) gas permeating the cluster gravitational potential well is formed. The typical total mass of a cluster of galaxies is of the order of $10^{14}-10^{15}$ M$_\odot$, 85% of which is in dark matter and 15% in baryons. The baryonic content of galaxy clusters is distributed among a hot X-ray emitting phase (generally referred to as the ICM) and a cold component mostly traced by stars. Such a cold component is only 10% of the total baryons and is responsible for the metal enrichment through star formation activity. In fact, metals are produced in stars and are injected into the ICM by Supernovae (SNe) explosions through subsequent episodes of star formation (e.g. Matteucci & Vettolani 1988). The primordial, low-metallicity gas collapsed in the cluster potential wells, is eventually enriched in metals as a function of the environment and cosmic time, and the chemical enrichment is paralleled by a corresponding heating of the diffuse baryons.

The ICM typically reaches temperatures of several 10^7 K (several keV), therefore, emits mainly via thermal bremsstrahlung in the X-rays. At such temperatures most of the elements are either fully ionized or in a high ionization state. Strong emission lines may originate by collisional excitation of K- and L-shell transitions in highly ionized elements, such as H- and He-like iron, oxygen, silicon or sulfur. In the isothermal approximation, the line intensities depend on the abundances of heavy elements, while the continuum intensity is mainly due to hydrogen and helium. Therefore the equivalent width of a line, under the reasonable assumption of collisional equilibrium (see also the Appendix for the validity of this assumption in the ICM), gives a direct measurement of the abundance of the corresponding element.

The presence of emission lines in the spectrum of the X-ray emitting hot gas inside clusters of galaxies is an unambiguous evidence of the chemical enrichment of the ICM and a clear signature of star formation in cluster galaxies. Measurements of the metal content of clusters of galaxies provide an invaluable *fossil record of their past star formation history*. A knowledge of the history of the ICM metal enrichment is also necessary to understand the mode and epoch of cluster formation, and the thermodynamic evolution of the cluster baryons in their hot and cold phase. In this respect, measuring the properties of the ICM at high redshift is important to constrain the physical processes involved in the diffusion of energy and metals within clusters. In particular, the chemical evolution of the ICM sets constraints on the SNe rate in the cluster galaxies (see Ettori 2005). SNe explosions are, in fact, the main contributor to the metal enrichment and are also expected to provide a source of ICM heating (e.g. Pipino et al. 2002; Tornatore et al. 2004).

In addition, much emphasis has been given recently to the evolution of global scaling relations for the ICM, such as the luminosity-temperature relation and the entropy-temperature relation (Holden et al. 2002; Vikhlinin et al. 2002; Ettori et al. 2004; Pratt et al. 2006; Maughan et al. 2006). Such scaling relations represent a further signature of galaxy formation and super-massive black holes activity, whose relative contribution to the ICM energetic is under investigation.

A large fraction (∼80%) of the local clusters exhibit central surface brightness peaks (see Bauer et al. 2005), which are the observational signature of a *cool core*. Cool-core clusters are relatively relaxed clusters (i.e. the radiative cooling time is shorter than the estimated age). In fact, the central regions of a cluster of galaxies must remain relatively relaxed both to establish and to maintain a cool core. Strong disturbances to the cluster, such as those caused by merging, for instance, could mix the cluster gas and disrupt the cool core.

The determination of an average value of the ICM iron content is a hard task due to the different metal distribution inside cool-core and non cool-core clusters (De Grandi et al. 2004; Vikhlinin et al. 2005; Baldi et al. 2007). The former show a central peak of Iron abundance with $Z_{Fe} \simeq 0.6 - 0.8\, Z_{\odot}$ and a plateau at $Z_{Fe} \simeq 0.3\, Z_{\odot}$ in the outer regions (see Tamura et al. 2004; Vikhlinin et al. 2005), while the latter a somewhat lower value ($Z_{Fe} \simeq 0.2 - 0.3\, Z_{\odot}$) constant with radius. The Iron-rich cores have typically a size of 100 kpc (see De Grandi et al. 2004; Vikhlinin et al. 2005; Baldi et al. 2007). However, when distant clusters are analyzed their metallicity is averaged over larger regions, thus changing the relative weight of the iron-rich cores. Therefore, it is important to take into account effects due to different physical apertures when comparing different samples from the literature.

De Grandi et al. (2004) also found that the cluster iron mass is tightly correlated to the X-ray luminosity and that the iron mass excess in the cool-core clusters can be entirely produced by the Brightest Cluster Galaxy (BCG). This suggests a strong connection between the formation of the giant BCG and its hosting cluster.

Studies of local cluster samples have also found an increase of the iron abundance in clusters with temperatures $\lesssim 5$ keV (Arnaud et al. 1992; Finoguenov et al. 2001; Baumgartner et al. 2005), whose physical interpretation is still matter of debate.

Single observations of high-z ($z > 1$) clusters confirmed that $Z_{Fe} \simeq 0.3\, Z_{\odot}$ or higher is common in the ICM (Rosati et al. 2004; Hashimoto et al. 2004). This implies that the last episode of star formation in clusters of galaxies must have taken place at earlier epochs in order to significantly enrich the diffuse medium with metals. Therefore, the study of the iron abundance at high redshift is expected to place strong constraints on the star formation history in cluster galaxies and on its effects on the thermodynamics of the ICM.

In this work, we present a significantly improved analysis compared to a previous work by Tozzi et al. (2003, hereafter T03) by substantially extending the sample (56 clusters instead of the 19 presented in T03) and by using the most recent *Chandra* calibrations in order to have an up-to-date data reduction at the time of writing. This increase in statistics allows us to investigate the relation between the iron abundance and global temperature of the ICM at high redshift and to derive a more robust measurement of the cosmic evolution of the average iron abundance in the ICM, which is then compared with predictions from the cosmic star formation rate.

2.2 Sample selection and data reduction

2.2.1 *Chandra* data

In Table 2.1, we present the list of *Chandra* observations analyzed in this paper. The selected sample consists of all the public *Chandra* archived observations of clusters with $z \geq 0.4$ as of June 2004, including 9 clusters with $0.3 < z < 0.4$. Some of them were already presented in T03. Data reduction is performed using the CIAO 3.2 software package with a recent version of the Calibration Database (CALDB 3.0.0) including the correction for the degraded effective area of ACIS-I chips due to material accumulated on the ACIS optical blocking filter at the epoch of the observation. We also applied the time-dependent gain correction[1], which is necessary to adjust the "effective gains", which have been drifting with time due to an increasing charge transfer inefficiency (CTI). Most of the observations were carried out with the ACIS-I instrument, while for some clusters (see Table 2.1) the Back Illuminated S3 chip of ACIS-S was also used.

We started to process data from the level=1 event file. For observations taken in the VFAINT mode, we run the tool `acis_process_events` to flag probable background events using all the information of the pulse heights in a 5×5 event island (as opposed to a 3×3 event island recorded in the FAINT mode) to help in distinguishing between genuine X-ray events and artificial events that are most likely associated with cosmic rays. With this procedure, the ACIS particle background can be significantly reduced compared

[1] http://asc.harvard.edu/ciao/threads/acistimegain/

Table 2.1: *Chandra* archive clusters sample.

Cluster	z	Obs. Id.[a]	Exp. [ks][b]	Mode[c]	R_{ext} [″][d]	Net Cts[e]
MS 1008.1 − 1224	0.306	926	44	I–V	108.5	9260
MS 2137.3 − 2353	0.313	928	33	S–V	79.0	33000
Abell 1995	0.319	906	56.4	S–F	103.0	30100
MACS J0308.9 + 2645	0.324	3268	24.4	I–V	123.0	11200
ZwCl 1358.1 + 6245	0.328	516	48.3	S–F	88.5	19800
MACS J0404.6 + 1109	0.355	3269	21.6	I–V	157.0	3100
RX J0027.6 + 2616	0.367	3249	9.8	I–V	108.0	960
MACS J1720.2 + 3536	0.391	3280	20.8	I–V	103.0	6670
ZwCl 0024.0 + 1652	0.395	929	39.5	S–F	64.0	3150
V 1416 + 4446	0.400	541	31.0	I–V	73.8	2130
MACS J0159.8 − 0849	0.405	3265	17.6	I–V	118.0	8100
MACS J2228.5 + 2036	0.412	3285	20	I–V	137.7	6070
MS 0302.7 + 1658	0.424	525	10.0	I–V	59.0	635
MS 1621.5 + 2640	0.426	546	30.0	I–F	118.0	3280
MACS J0417.5 − 1154	0.440	3270	12	I–V	138.0	7400
MACS J1206.2 − 0847	0.440	3277	23	I–V	138.0	11720
RX J1347.5 − 1145	0.451	3592	57.5	I–V	128.0	62700
V 1701 + 6414	0.453	547	49.0	I–V	64.0	2745
CL 1641 + 4001	0.464	3575	45.0	I–V	49.0	1040
MACS J1621.4 + 3810	0.465	3254	9.7	I–V	78.0	1600
MACS J1824.3 + 4309	0.487	3255	14.8	I–V	84.0	530
MACS J1311.0 − 0311	0.492	3258	14.8	I–V	79.0	2100
V 1525 + 0958	0.516	1664	50	I–V	79.0	2100
MS 0451.6 − 0305	0.539	529,902	56	I/S–V	98.4	16850
MS 0015.9 + 1609	0.541	520	67.0	I–V	98.4	16200
MACS J1149.5 + 2223	0.544	1656,3589	38	I–V	148.0	9400
MACS J1423.8 + 2404	0.545	1657	18.5	I–V	79.0	3600
MACS J0717.5 + 3745	0.548	1655,4200	78	I–V	144.0	29000
V 1121 + 2327	0.562	1660	70.0	I–V	69.0	2050
SC 1120 − 1202	0.562	3235	68	I–V	49.0	730
RX J0848.7 + 4456	0.570	927,1708	184.5	I–V	30.0	850
MACS J2129.4 − 0741	0.570	3199	17.6	I–V	98.0	3000
MS 2053.7 − 0449	0.583	551,1667	88	I–V	54.1	2150
MACS J0647.7 + 7015	0.584	3196	19.2	I–V	88.5	3170
RX J0956.0 + 4107	0.587	5294	17.2	I–V	64.0	500
CL 0542.8 − 4100	0.634	914	50	I–F	78.7	2220
RCS J1419.2 + 5326	0.640	3240	9.7	S–V	44.0	470
MACS J0744.9 + 3927	0.686	3197,3585	40	I–V	98.0	6100
RX J1221.4 + 4918	0.700	1662	78	I–V	78.7	2900
RX J1113.1 − 2615	0.730	915	103	I–F	39.4	1200
RX J2302.8 + 0844	0.734	918	108	I–F	54.0	1600
MS 1137.5 + 6624	0.782	536	117	I–V	49.2	4150
RX J1317.4 + 2911	0.805	2228	110.5	I–V	24.5	240
RX J1350.0 + 6007	0.810	2229	58	I–V	64.0	750
RX J1716.4 + 6708	0.813	548	51	I–F	54.0	1520
RX J0152.7 − 1357 S	0.828	913	36	I–F	52.7	570
MS 1054.4 − 0321	0.832	512	80	S–F	78.7	10000
RX J0152.7 − 1357 N	0.835	913	36	I–F	58.0	830
1WGA J1226.9 + 3332	0.890	932,3180	41	S–V	64.0	2400
CL 1415.1 + 3612	1.030	4163	89	I–V	39.4	1320
RDCS J0910 + 5422	1.106	2227,2452	170	I–V	24.6	440
RX J1053.7 + 5735 E*	1.134	4936	94	S–V	28.2	300
RX J1053.7 + 5735 W*	1.134	4936	94	S–V	28.2	450
RDCS J1252 − 2927*	1.235	4198,4403	188.4	I–V	34.5	850
RDCS J0849 + 4452*	1.261	927,1708	184.5	I–V	23.6	360
RDCS J0848 + 4453	1.273	927,1708	184.5	I–V	19.7	130

Notes: [a] observation identification number; [b] effective exposure time after removal of high background intervals; [c] detector (ACIS-I or -S) and telemetry (FAINT or VFAINT) used; [d] extraction radius; [e] number of net detected counts in the $0.3 - 10$ keV band; * denotes clusters for which we also use XMM-*Newton* observations (see Table 2.2).

to the standard grade selection[2]. Real X-ray photons are hardly affected by such cleaning (only less than 2% of them are rejected, independent of the energy band, provided there is no pileup). We also applied the CTI correction[3] to the observations taken when the temperature of the focal plane was 153 K. This procedure allows us to recover the original spectral resolution that is partially lost because of the CTI. The correction applies only to ACIS-I chips, since the ACIS-S3 did not suffer from radiation damage.

For data taken in the FAINT mode we ran the tool `acis_process_events` only to apply the CTI and the time-dependent gain correction. From this point on, the reduction was similar for both the FAINT and the VFAINT exposures. The data were filtered to include only the standard event grades 0, 2, 3, 4, and 6. We checked visually for hot columns left from the standard cleaning. Only in a few cases did hot columns have to be removed by hand. We identify the flickering pixels as the pixels with more than two events contiguous in time, where a single time interval was set to 3.3 s. For exposures taken in VFAINT mode, there were practically no flickering pixels left after filtering out "bad" events. We finally filtered time intervals with high background by performing a 3σ clipping of the background level using the script `analyze_ltcrv`[4]. Removed time intervals always amount to less than 5% of the nominal exposure time for ACIS-I chips. Some ACIS-I observations show large flares on the ACIS-S3 chip (which is on by default but not used in the data analysis), but the corresponding time intervals are not removed since the flares do not affect the ACIS-I chips. In any case, our spectral analysis is not strongly affected by residual flares, since we always compute the background from source-free regions around the clusters from the same observation (see below), thus taking into account any possible spectral distortion of the background itself induced by the flares.

As in T03, we performed a spectral analysis extracting the spectrum of each source from a region defined in order to maximize the signal-to-noise ratio (S/N, see Appendix A.1 for details on how this is computed). This choice of the extraction region allows the global properties of the clusters to be measured using the majority of the signal. This strategy is optimized for the highest redshift objects, and it is homogeneously adopted for the whole sample. The region of maximum S/N is obtained through the following procedure: the spectrum of each source is extracted from a circular region around the centroid of the photon distribution. For a given radius, we find the center of the region that includes the maximum number of net counts in the $0.5 - 5$ keV band, where the bulk of the source counts are detected. Then, we compute the S/N, repeating this procedure for several radii. Finally we choose the extraction radius R_{ext}, defined as the radius for which the S/N is maximum. As shown in Fig. 2.1, in most cases R_{ext} is between 0.15 and 0.3 times the virial radius R_{vir}, estimated, after Evrard et al. (1996), as

$$R_{vir} = 3.95 \left(\frac{T_{vir}}{10\,\mathrm{keV}}\right)^{\frac{1}{2}} F(z)\ \mathrm{Mpc}\,. \tag{2.1}$$

Here the virial temperature T_{vir} is approximated with the spectral temperature T_{spec} measured within R_{ext}, and

$$F(z) = (\Delta(z)/\Delta_0)^{-1/6}\,[\Omega_0\,(1+z)^3 + 1 - \Omega_0]^{-1/2}\,, \tag{2.2}$$

where $\Delta(z)$ is the density contrast of the virialized halo with respect to the critical density. For simplicity we assume a constant value here for $(\Delta(z)/\Delta_0)^{-1/6}$ (see Bryan & Norman 1998). From Fig. 2.1 we note that the typical extraction region, depending both on the redshift through the surface brightness dimming and on the brightness distribution of each source, does not show a clear trend with redshift, with the exception of the highest-z bin where $R_{ext} \leq 0.15\,R_{vir}$. The fraction of net counts included in the extraction region always amounts to $80 - 90\%$ of the total detected for each cluster. We also note that R_{ext} is roughly 3 times the core radius measured with a beta model (see Ettori et al. 2003 for the spatial analysis of a subsample of our clusters).

For each cluster, we used the events included in each of the extraction regions defined above to produce a spectrum (pha) file. The background is always obtained from empty regions of the chip in which the source is located. This is possible since all sources have an extension of less than 3 arcmin, as opposed to the 8 arcmin size of the ACIS-I/-S chips. The background file is scaled to the source file by the ratio of the geometrical area. The background regions should partially overlap with the outer virialized regions of the clusters. However, the cluster emission from these regions is negligible compared to the instrumental background and does not affect our results. Our background subtraction procedure, on the other hand, has the advantage of providing the best estimate of the background for that specific observation. By comparing

[2]http://asc.harvard.edu/cal/Links/Acis/acis/Cal_prods/vfbkgrnd/
[3]http://cxc.harvard.edu/ ciao/threads/acisapplycti/
[4]http:// cxc.harvard.edu/ciao/threads/filter_ltcrv/

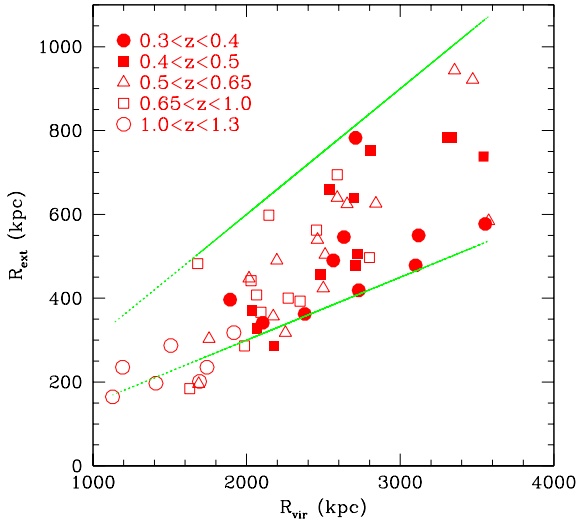

Figure 2.1: Extraction radius (R_{ext}) versus virial radius (R_{vir}) for the whole sample. Lower and upper lines show $R_{ext} = 0.15\,R_{vir}$ and $R_{ext} = 0.3\,R_{vir}$, respectively.

Table 2.2: Additional XMM-*Newton* observations at $z > 1$.

Cluster	z	Exp. [ks][a]	Detector[b]	R_{ext} ["][c]	Net Counts[d]
RX J105346.6 + 573517 E	1.134	94.5	PN+2MOS	32	708
RX J105346.6 + 573517 W	1.134	94.5	PN+2MOS	32	875
RDCS J1252 − 2927	1.235	65.0	PN+2MOS	34.5	1570
RDCS J0849 + 4452	1.261	112.0	PN+2MOS	29.5	630

Notes: [a] effective exposure time after removal of high background intervals; [b] detectors used; [c] extraction radius; [d] number of net detected counts in the 0.3 − 10 keV band.

the count rate in the source and in the background at energies higher than 8 keV, we finally checked that variations in the background intensity across the chip did not affect the background subtraction, where the signal from the clusters is null. The response matrices and the ancillary response matrices of each spectrum were computed respectively with `mkacisrmf` and `mkwarf` for the same regions from which the spectra were extracted. For those observations for which the CTI correction cannot be applied (when the temperature of the detector is larger than 153 K), we used `acisspec` instead.

2.2.2 XMM-*Newton* data

As in T03, we used the XMM-*Newton* data to boost the S/N only for the most distant clusters in our current sample, namely the clusters at $z > 1$. In Table 2.2 we list the four XMM-*Newton* observations of high redshift ($z > 1$) clusters included in our analysis. For each observation we used both the European Photon Imaging Camera (EPIC) PN and the two MOS detectors. The XMM-*Newton* observations and data reduction relative to RDCS J0849 and the two clumps of RX J1053 have already been presented in T03, while those relative to RDCS J1252 are described in Rosati et al. (2004).

2.3 Results

In this section we present the main results of our analysis. The section is subdivided into five subsections. In Sect. 2.3.1 we provide a general description of our spectral analysis and a comparison with the previous results obtained in T03. In Sect. 2.3.2 we describe the single source analysis and the main properties of the sample. In Sect. 2.3.3 the correlation between iron abundance and temperature is discussed. In Sect. 2.3.4 we present our results on the evolution of the average iron abundance as a function of redshift

obtained through two independent methods (*combined fits* and *weighted means*). Finally, in Sect. 2.3.5 we present a comparison with the *local* iron abundance of the ICM.

2.3.1 Spectral analysis

The spectra were analyzed with XSPEC v11.3.1 (Arnaud 1996) and fitted with a single-temperature `mekal` model (Kaastra 1992; Liedahl et al. 1995) in which the ratio between the elements was fixed to the solar value as in Anders & Grevesse (1989). These values for the solar metallicities have more recently been superseded by the new values by Grevesse & Sauval (1998) and Asplund et al. (2005), who introduced a 0.676 and 0.60 times lower iron solar abundance, respectively (photometric value). However, we prefer to report iron abundances in units of solar abundances by Anders & Grevesse (1989) since most of the literature still refers to them. We also performed the fits using solar abundances by Asplund et al. (2005). The iron abundances in these units (reported in the fifth column of Table 3) can be obtained with an accuracy of about 10% simply by rescaling the values measured in solar units by Anders & Grevesse (1989) by a factor of 1.6. This shows that we are not affected by the presence of metals other than iron. Finally, we model Galactic absorption with `tbabs` (Wilms et al. 2000).

It has recently been shown that a methylene layer on the *Chandra* mirrors increases the effective area at energies higher than 2 keV (Marshall et al. 2004)[5]. This has a small effect on the total measured fluxes, but it may be non-negligible on the spectral parameters (i.e., it may artificially reduce the temperatures). In order to correct for it, we introduced a "positive absorption edge" (XSPEC model `edge`) in the fitting model at 2.07 keV with $\tau = -0.15$ (Vikhlinin et al. 2005).

The fits were performed over the energy range $0.6 - 8.0$ keV. Due to uncertainties in ACIS calibration below 0.6 keV, we excluded less energetic photons from the spectral analysis in order to avoid systematic bias. The effective cut at high energies is generally lower than $7 - 8$ keV, since the S/N for a thermal spectrum rapidly decreases above 5 keV.

The free parameters in our spectral fits are temperature, metallicity, and normalization. Local absorption is fixed to the Galactic neutral hydrogen column density (N_H in Table 2.3), as obtained from radio data (Dickey & Lockman 1990), and the redshift to the value measured from optical spectroscopy (z in Table 2.3). We used Cash statistics applied to the source plus background[6], which is preferable for low S/N spectra (Nousek & Shue 1989).

Eventhough our analysis procedure is similar to the one used in T03, new calibrations (including the treatment of the positive edge at 2.07 keV) may cause some differences in the new temperature and iron abundance values compared to the previous analysis. To investigate such differences, we show in Fig. 2.2 the temperatures and iron abundances published in T03, plotted against the new values (presented in this paper) for the 17 clusters observed with *Chandra* in both samples, plus RDCS 1252 (Rosati et al. 2004). The new best-fit temperatures (upper panel) seem to be slightly higher than in T03, while iron abundances (lower panel) are much less affected by the new calibrations. As a further check we recomputed the average values of the iron abundance in the same redshift bins used in T03 and we find consistent results (see Fig. 2.3). The only noticeable difference is the hint of a decrease with z, well below the 2σ confidence level in T03, which is now slightly enhanced. Therefore, the most significant improvements with respect to T03 are due to the new clusters included in the current sample. In particular, we recall that the $z \simeq 1.2$ point was entirely dominated by the XMM data on RX J1053, since in T03 there was no statistically significant detection of the iron line at $z > 1$ from *Chandra* data only. The situation at $z > 1$ has improved thanks to the *Chandra* observations of CL 1415 and RDCS 1252. Finally, the statistics of the current sample mostly improved in the redshift range $0.3 < z < 0.6$.

2.3.2 Single source analysis

This section presents the results of the spectral analysis of each of the 56 clusters of our sample. The results of the spectral fits, referring to the region of radius R_{ext}, defined in Sect. 2.2, are listed in Table 2.3. Histograms of the redshift and temperature distribution of the sample are shown in Fig. 2.4.

The redshift distribution is peaked around $z \simeq 0.5$, while at $z > 1$ we have only 7 objects (we recall that we consider the two clumps of RX J1053 separately, see Hashimoto et al. 2004). In order to investigate the properties of the sample as a function of redshift, we divide the clusters in 5 redshift intervals (10 objects with $0.3 < z < 0.4$; 12 objects with $0.4 < z < 0.5$; 15 objects with $0.5 < z < 0.65$; 12 objects with

[5] http://cxc.harvard.edu/ccw/proceedings/03_proc/presentations/ marshall2
[6] http://heasarc.gsfc.nasa.gov/docs/xanadu/xspec/manual/ XSappendixCash.html

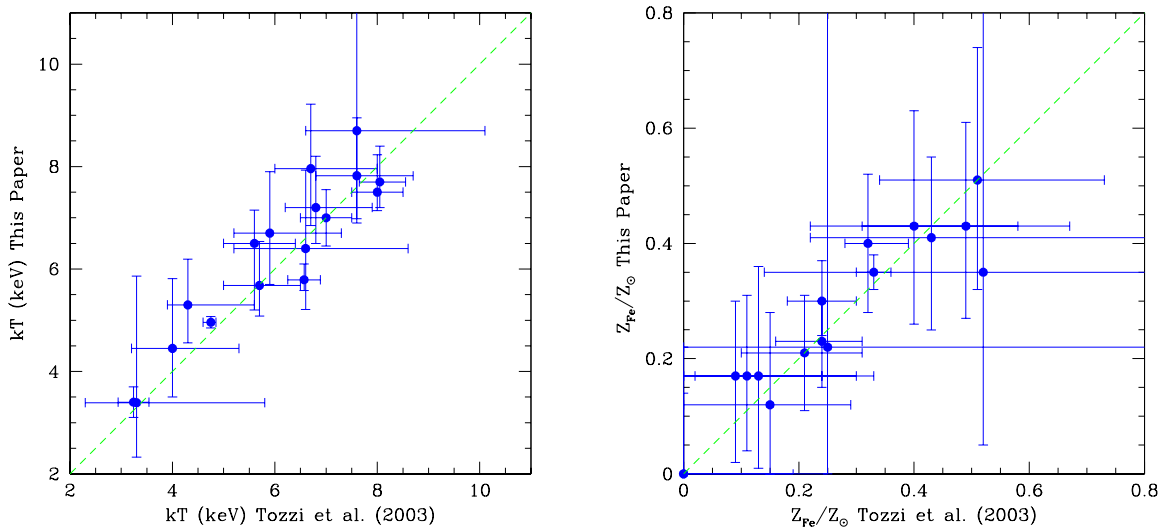

Figure 2.2: Comparison between the temperature (*left panel*) and iron abundance (*right panel*) values measured in T03, and those measured in this work after the most recent *Chandra* calibrations have been applied. Dashed lines show the locus of equal temperature and abundance values.

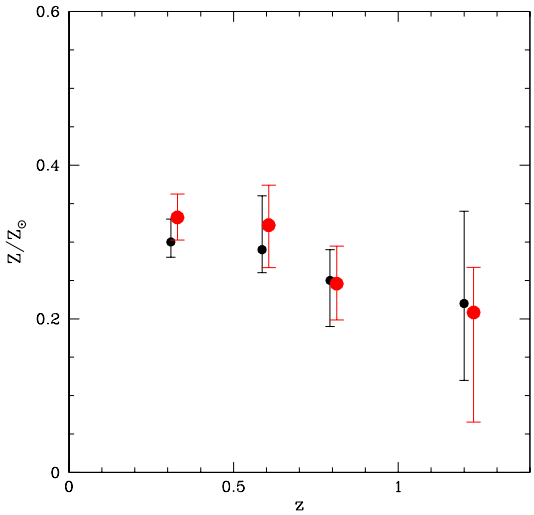

Figure 2.3: Average iron abundance in different redshift bins computed for the same sample of clusters analyzed in T03 using updated calibrations (red circles), compared with the previous results (black circles). The plot shows that the new calibrations and data reduction have a negligible effect on our results. Only clusters with $kT > 5$ keV are considered.

Table 2.3: Spectral fit results obtained with the `tbabs(mekal)` model.

Cluster	z	kT [keV][a]	$Z/Z_\odot$ (AG89)[b]	$Z/Z_\odot$ (A05)[c]	N_H [cm^{-2}][d]	χ^2_r [d.o.f.] [e]	NHP[f]
MS 1008.1 − 1224	0.306	$5.8^{+0.3}_{-0.2}$	$0.30^{+0.07}_{-0.06}$	$0.47^{+0.11}_{-0.10}$	7.26×10^{20}	1.23 [228]	0.009
MS 2137.3 − 2353	0.313	4.96 ± 0.11	0.35 ± 0.03	$0.56^{+0.06}_{-0.05}$	3.55×10^{20}	1.23 [289]	0.004
Abell 1995	0.319	8.60 ± 0.32	0.40 ± 0.06	$0.64^{+0.10}_{-0.10}$	1.42×10^{20}	1.22 [343]	0.003
MACS J0308.9 + 2645	0.324	11.2 ± 0.7	0.37 ± 0.06	$0.70^{+0.10}_{-0.12}$	1.18×10^{21}	1.07 [283]	0.194
ZwCl 1358.1 + 6245	0.328	6.70 ± 0.26	0.40 ± 0.06	$0.64^{+0.11}_{-0.10}$	1.92×10^{20}	1.23 [282]	0.006
MACS J0404.6 + 1109	0.355	$6.9^{+0.6}_{-0.8}$	$0.16^{+0.07}_{-0.11}$	$0.22^{+0.14}_{-0.20}$	1.43×10^{21}	1.01 [165]	0.451
RX J0027.6 + 2616	0.367	$9.1^{+2.6}_{-1.5}$	$0.57^{+0.27}_{-0.19}$	$1.02^{+0.34}_{-0.35}$	3.86×10^{20}	1.36 [52]	0.042
MACS J1720.2 + 3536	0.391	6.30 ± 0.33	$0.50^{+0.05}_{-0.06}$	$0.83^{+0.07}_{-011}$	3.40×10^{20}	0.74 [189]	0.997
ZwCl 0024.0 + 1652	0.395	4.38 ± 0.27	$0.75^{+0.20}_{-0.18}$	$1.22^{+0.32}_{-0.29}$	4.20×10^{20}	1.02 [128]	0.410
V 1416 + 4446	0.400	3.50 ± 0.18	0.88 ± 0.18	$1.50^{+0.35}_{-0.27}$	1.29×10^{20}	1.11 [98]	0.219
MACS J0159.8 − 0849	0.405	$9.2^{+0.6}_{-0.5}$	0.36 ± 0.05	$0.59^{+0.08}_{-0.09}$	2.08×10^{20}	1.13 [208]	0.097
MACS J2228.5 + 2036	0.412	7.9 ± 0.6	$0.41^{+0.06}_{-0.07}$	$0.59^{+0.09}_{-0.10}$	4.58×10^{20}	0.91 [196]	0.801
MS 0302.7 + 1658	0.424	$4.34^{+0.56}_{-0.44}$	$0.40^{+0.21}_{-0.18}$	$0.58^{+0.34}_{-0.28}$	1.11×10^{21}	0.98 [31]	0.490
MS 1621.5 + 2640	0.426	$6.9^{+0.7}_{-0.6}$	$0.35^{+0.08}_{-0.09}$	0.63 ± 0.14	3.58×10^{20}	0.90 [157]	0.804
MACS J0417.5 − 1154	0.440	11.3 ± 0.8	$0.29^{+0.06}_{-0.07}$	$0.45^{+0.10}_{-0.11}$	3.86×10^{20}	0.82 [209]	0.971
MACS J1206.2 − 0847	0.440	$11.0^{+0.7}_{-0.6}$	$0.18^{+0.05}_{-0.06}$	$0.25^{+0.10}_{-0.09}$	3.72×10^{20}	1.15 [271]	0.045
RX J1347.5 − 1145	0.451	14.0 ± 0.4	0.33 ± 0.04	$0.55^{+0.07}_{-0.06}$	4.92×10^{20}	1.20 [436]	0.003
V 1701 + 6414	0.453	$4.27^{+0.26}_{-0.25}$	$0.54^{+0.13}_{-0.12}$	$0.85^{+0.22}_{-0.20}$	2.46×10^{20}	0.95 [123]	0.649
CL 1641 + 4001	0.464	4.8 ± 0.6	$0.48^{+0.19}_{-0.16}$	$0.79^{+0.29}_{-0.24}$	1.10×10^{20}	0.98 [53]	0.509
MACS J1621.4 + 3810	0.465	6.5 ± 0.7	0.13 ± 0.08	$0.19^{+0.15}_{-0.16}$	1.09×10^{20}	1.46 [67]	0.549
MACS J1824.3 + 4309	0.487	$7.2^{+2.2}_{-1.3}$	$0.38^{+0.23}_{-0.25}$	$0.55^{+0.31}_{-0.33}$	4.46×10^{20}	1.03 [33]	0.423
MACS J1311.0 − 0311	0.492	8.0 ± 0.9	0.39 ± 0.09	$0.60^{+0.21}_{-0.19}$	1.87×10^{20}	0.97 [87]	0.571
V 1525 + 0958	0.516	$5.4^{+0.4}_{-0.5}$	0.35 ± 0.10	$0.54^{+0.21}_{-0.20}$	2.91×10^{20}	1.06 [107]	0.315
MS 0451.6 − 0305	0.539	$8.2^{+0.4}_{-0.3}$	0.34 ± 0.06	0.57 ± 0.10	4.97×10^{20}	1.24 [279]	0.004
MS 0015.9 + 1609	0.541	$9.3^{+0.5}_{-0.3}$	$0.33^{+0.06}_{-0.05}$	0.53 ± 0.09	4.07×10^{20}	1.01 [302]	0.460
MACS J1149.5 + 2223	0.544	$12.9^{+1.2}_{-1.0}$	$0.21^{+0.06}_{-0.07}$	$0.37^{+0.10}_{-0.11}$	2.28×10^{20}	1.04 [254]	0.317
MACS J1423.8 + 2404	0.545	$7.3^{+0.6}_{-0.5}$	$0.31^{+0.06}_{-0.08}$	$0.46^{+0.13}_{-0.10}$	2.38×10^{20}	1.11 [135]	0.174
MACS J0717.5 + 3745	0.548	13.3 ± 0.7	$0.18^{+0.05}_{-0.04}$	$0.29^{+0.11}_{-0.07}$	7.04×10^{20}	1.14 [404]	0.029
V 1121 + 2327	0.562	5.2 ± 0.5	$0.27^{+0.10}_{-0.08}$	$0.43^{+0.15}_{-0.07}$	1.32×10^{20}	0.99 [102]	0.499
SC 1120 − 1202	0.562	$5.7^{+1.3}_{-0.8}$	$0.23^{+0.20}_{-0.17}$	$0.33^{+0.33}_{-0.21}$	5.19×10^{20}	1.13 [45]	0.256
RX J0848.7 + 4456	0.570	3.4 ± 0.30	$0.51^{+0.23}_{-0.19}$	$0.79^{+0.36}_{-0.30}$	2.63×10^{20}	1.33 [46]	0.068
MACS J2129.4 − 0741	0.570	$8.7^{+0.7}_{-0.8}$	$0.51^{+0.08}_{-0.11}$	0.82 ± 0.14	4.82×10^{20}	0.85 [132]	0.890
MS 2053.7 − 0449	0.583	$5.68^{+0.57}_{-0.47}$	$0.16^{+0.11}_{-0.10}$	$0.24^{+0.18}_{-0.16}$	5.02×10^{20}	1.03 [100]	0.402
MACS J0647.7 + 7015	0.584	$15.5^{+2.3}_{-1.7}$	< 0.10	< 0.15	5.64×10^{20}	0.91 [118]	0.737
RX J0956.0 + 4107	0.587	$7.4^{2.5}_{-1.45}$	$0.13^{+0.28}_{-0.13}$	$0.21^{+0.45}_{-0.21}$	1.14×10^{20}	1.08 [27]	0.353
CL 0542.8 − 4100	0.634	$7.9^{+1.1}_{-0.8}$	$0.20^{+0.12}_{-0.09}$	$0.31^{+0.19}_{-0.15}$	3.73×10^{20}	1.19 [113]	0.081
RCS J1419.2 + 5326	0.640	$4.1^{+0.7}_{-0.6}$	$0.15^{+0.21}_{-0.15}$	$0.16^{+0.31}_{-0.16}$	1.18×10^{20}	1.35 [21]	0.131
MACS J0744.9 + 3927	0.686	9.2 ± 0.6	0.28 ± 0.06	$0.46^{+0.10}_{-0.12}$	5.71×10^{20}	1.22 [193]	0.021
RX J1221.4 + 4918	0.700	$8.4^{+0.9}_{-0.8}$	$0.29^{+0.13}_{-0.12}$	$0.48^{+0.21}_{-0.19}$	1.47×10^{20}	0.99 [141]	0.534
RX J1113.1 − 2615	0.730	$5.7^{+0.9}_{-0.6}$	$0.43^{+0.20}_{-0.17}$	$0.68^{+0.30}_{-0.27}$	5.50×10^{20}	0.69 [59]	0.966
RX J2302.8 + 0844	0.734	$8.0^{+1.3}_{-1.1}$	$0.12^{+0.16}_{-0.12}$	$0.19^{0.26}_{-0.19}$	4.85×10^{20}	0.85 [81]	0.833
MS 1137.5 + 6624	0.782	6.8 ± 0.5	0.26 ± 0.11	$0.43^{+0.18}_{-0.17}$	1.21×10^{20}	1.09 [151]	0.204
RX J1317.4 + 2911	0.805	$4.5^{+1.4}_{-1.0}$	$0.35^{+0.46}_{-0.30}$	$0.49^{+0.67}_{-0.46}$	1.10×10^{20}	0.71 [14]	0.768
RX J1350.0 + 6007	0.810	$4.4^{+0.7}_{-0.6}$	$0.56^{+0.27}_{-0.18}$	$0.96^{+0.35}_{-0.33}$	1.80×10^{20}	1.26 [51]	0.103
RX J1716.4 + 6708	0.813	$6.9^{+0.8}_{-0.7}$	$0.49^{+0.18}_{-0.16}$	$0.79^{+0.29}_{-0.26}$	3.72×10^{20}	0.77 [76]	0.934
RX J0152.7 − 1357 S	0.828	$8.7^{+2.4}_{-1.8}$	< 0.22	< 0.37	1.54×10^{20}	1.06 [32]	0.376
MS 1054.4 − 0321	0.832	$7.5^{+0.7}_{-0.4}$	$0.23^{+0.07}_{-0.08}$	$0.38^{+0.12}_{-0.12}$	3.61×10^{20}	1.15 [238]	0.056
RX J0152.7 − 1357 N	0.835	$6.7^{+1.2}_{-1.0}$	$0.17^{+0.19}_{-0.16}$	$0.25^{+0.30}_{-0.25}$	1.54×10^{20}	0.87 [45]	0.715
1WGA J1226.9 + 3332	0.890	$12.9^{1.4}_{-1.2}$	$0.02^{+0.12}_{-0.02}$	< 0.21	1.38×10^{20}	1.06 [97]	0.335
CL 1415.1 + 3612	1.030	$7.0^{+0.8}_{-0.7}$	$0.24^{+0.15}_{-0.13}$	$0.40^{+0.23}_{-0.21}$	1.09×10^{20}	0.79 [63]	0.891
RDCS J0910 + 5422	1.106	$6.4^{+1.5}_{-1.2}$	< 0.14	< 0.21	2.10×10^{20}	0.94 [28]	0.559
RX J1053.7 + 5735 E	1.134	$3.4^{+0.5}_{-0.4}$	$0.51^{+0.14}_{-0.15}$	$0.58^{+0.75}_{-0.22}$	5.7×10^{19}	1.11 [29]	0.317
RX J1053.7 + 5735 W	1.134	$7.2^{+1.2}_{-0.9}$	$0.32^{+0.14}_{-0.15}$	$0.51^{+0.23}_{-0.24}$	5.7×10^{19}	0.55 [31]	0.981
RDCS J1252 − 2927	1.235	$7.2^{+0.4}_{-0.6}$	$0.35^{+0.06}_{-0.09}$	$0.58^{+0.11}_{-0.15}$	5.95×10^{20}	1.01 [55]	0.454
RDCS J0849 + 4452	1.261	$6.2^{+1.0}_{-0.9}$	$0.16^{+0.13}_{-0.14}$	$0.21^{+0.27}_{-0.19}$	2.63×10^{20}	0.51 [24]	0.977
RDCS J0848 + 4453	1.273	$3.4^{+2.5}_{-1.1}$	$0.22^{+1.33}_{-0.22}$	$0.22^{+1.38}_{-0.22}$	2.63×10^{20}	1.04 [11]	0.411

Notes: [a] temperature; [b] iron abundance in solar units by Anders & Grevesse (1989) and [c] by Asplund et al. (2005); [d] local column density, always fixed to the Galactic value by Dickey & Lockman (1990); [e] reduced chi-square and degrees of freedom obtained after binning the spectra to 20 counts per bin; [f] null-hypothesis probability. Errors refer to the 1σ confidence level.

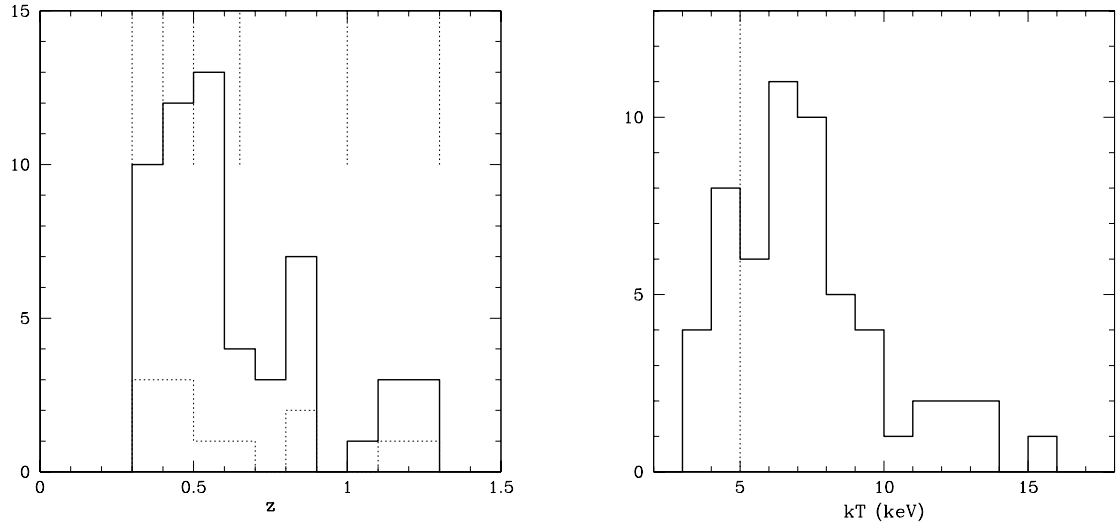

Figure 2.4: *(Left panel)* Histogram of the redshift distribution of the sample. The solid line refers to the whole sample, while the dotted line displays only clusters with $kT \leq 5$ keV (see Table 2.3). The vertical dotted lines indicate the five redshift intervals selected for the combined spectral analysis, as described in the text. *(Right panel)* Histogram of the temperature distribution of the sample. The vertical dotted line separates the moderate temperature ($kT < 5$ keV) clusters from the high temperature ($kT > 5$ keV) clusters.

$0.65 < z < 1.0$, and 7 objects with $1.0 < z < 1.3$). These intervals (Fig. 2.4) are defined in order to have a comparable number of objects in a reasonably narrow redshift range.

As shown in the temperature distribution (Fig. 2.4), we sampled mostly hot clusters ($kT > 5$ keV), while only 12 are in the *medium* temperature range ($3 < kT < 5$ keV). We would like to point out here that we derived a single spectral temperature for the region within R_{ext}. In principle, the spectral temperature can be significantly different from the emission-weighted and gas-mass-weighted temperature, in the presence of a thermally complex ICM (e.g. Mazzotta et al. 2004). In a few cases, the effect of the temperature gradient is strong enough to make the single-temperature fit unacceptable. To evaluate the goodness of each fit, we computed the χ^2 of each best-fit model after binning the spectrum to 20 counts per bin. We find that most of our spectra are well-fitted by a single-temperature `mekal` model (see 7th column in Table 2.3). However, when the number of the net detected counts becomes larger than $\sim 10^4$, the quality of the fits drops dramatically for about half of the clusters (see Fig. 2.5). If we consider a 1% null-hypothesis probability as the threshold for an acceptable fit, then we must reject the single-temperature model within R_{ext} for 5 clusters in our sample (namely MS 2137, A 1995, ZW 1358, RX J1347, and MS 0451). Note that we can also fit clusters with very disturbed morphology and high S/N (e.g. MACS J0717) with a single-temperature model, due to the very high temperatures involved, which provide composite spectra with much less features than spectra with low-temperature components. Indeed, the single-temperature model fails mostly when a strong cool-core with temperatures lower than 3 keV is present (e.g. Mazzotta et al. 2004), while it is still acceptable if the temperature range is well above this threshold.

Since we are focusing here on metallicity, we made a closer investigation of the best-fit Z_{Fe} values for the clusters with the lowest null-hypothesis probability. Since these clusters are also the ones with the highest S/N, we were able to perform a spatially resolved spectral analysis for about four concentric annuli. We find that the best-fit Z_{Fe} value measured with a single temperature mekal model within R_{ext}, is representative of the inner 400 kpc and is not dominated by the central bin. This result, implying that the presence of temperature gradient does not dramatically affect the measurements of iron abundance, is reinforced by the spectral simulations described in the Appendix B. Therefore we used the single-temperature best-fit values for all the clusters in our sample. The attempt to model the evolution of Z_{Fe} separately in the inner 100 kpc and the outer regions is deferred to a future paper.

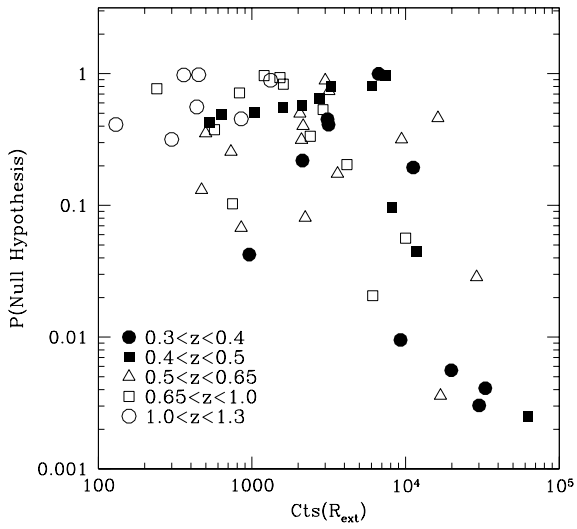

Figure 2.5: Null-hypothesis probability for the single-temperature best fits as a function of net detected counts for the whole sample.

Finally, we show in Fig. 2.6 the distribution of temperatures in our sample as a function of redshifts (error bars are at the 1σ confidence level). The Spearman test shows no correlation between temperature and redshift (Spearman's rank coefficient of $r_s = -0.095$ for 54 degrees of freedom, probability of null correlation $p = 0.48$). Fig. 2.6 shows that the range of temperatures in each redshift bin is about $6-7$ keV. Therefore, we are sampling a population of medium-hot clusters uniformly with redshift, with the hottest clusters preferentially in the redshift bin $0.4 < z < 0.6$.

The relations between temperature and iron abundance at different redshifts are shown in Fig. 2.7. For three clusters we can only derive upper limits on the iron abundance of the ICM, two of them at $z < 0.8$. For five clusters we measure positive iron abundances, which are still consistent with no detection at the 1σ c.l.. Overall, we detect the presence of the iron line in the large majority of the clusters, and measure the iron abundance with a typical error of 30% at the 1σ c.l. for $z < 0.6$, and 50% or larger at $z > 0.6$.

2.3.3 The iron abundance-temperature correlation

Our analysis (Fig. 2.8) suggests higher iron abundances at lower temperatures in all the redshift bins. This trend is somewhat blurred by the large scatter. We find a more than 2σ negative correlation for the whole sample, with a Spearman's rank coefficient of $r_s = -0.31$ for 54 degrees of freedom (probability of no correlation $p = 0.018$). The correlation is more evident when we compute the weighted average of the metallicity in six temperature intervals (see Table 2.4), as shown by the shaded areas in Fig. 2.8. The weighted mean is computed as $T_{wa} = \Sigma T_i w_i$ in each temperature bin, where $w_i = 1/\sigma_i^2/\Sigma(1/\sigma_i^2)$, and σ_i is the 1σ error on the single measurement. We find that in each bin the scatter of the best-fit values around the mean is comparable to the statistical errors on the single measurements (reduced $\chi^2_\nu \simeq 1$ assuming a constant Z_{Fe} in the bin), with the exception of the third and sixth bins, where the intrinsic scatter is larger ($\chi^2_\nu \simeq 3$).

This trend is similar to what is found in the ASCA data of nearby clusters by Baumgartner et al. 2005 (see also Arnaud et al. 1992; Mushotzky & Loewenstein 1997; Finoguenov et al. 2001). In their paper, the average iron abundance for $kT > 5$ keV is constant and equal to $Z \simeq 0.3\, Z_\odot$, while it rises to very high values (well above $0.4\, Z_\odot$) in the temperature range $2-3$ keV, and drops below $0.3\, Z_\odot$ for $kT < 2$ keV. It is worth noting, however, that this behavior is different from that of Ni and α-elements. Here, we confirm that in our high-redshift sample the average measured iron abundance rises below 5 keV. A simple power law fit of the form

$$Z(T) = Z_{Fe}(0)\, T^{-\alpha_T} \tag{2.3}$$

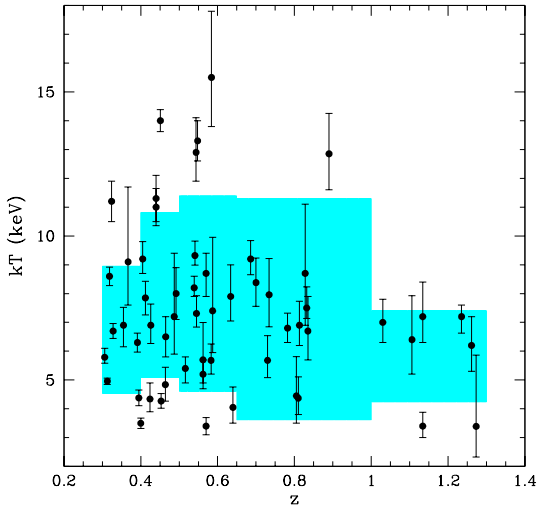

Figure 2.6: Temperature plotted vs redshift for the whole sample. Shaded areas show the *rms* dispersion around the weighted mean.

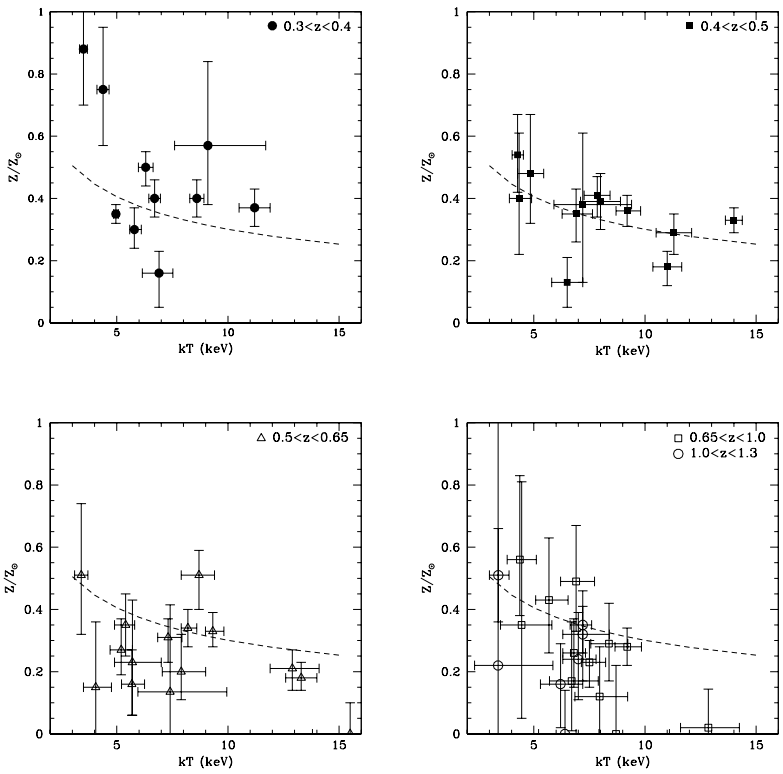

Figure 2.7: Iron abundance-temperature plots for the whole sample. The four panels show each redshift bin separately (last two bins in the fourth panel). The dashed line represents the best-fit metallicity-temperature relation ($Z/Z_\odot \simeq 0.88\,T^{-0.47}$) referring to the whole sample. Error bars refer to 1σ confidence level.

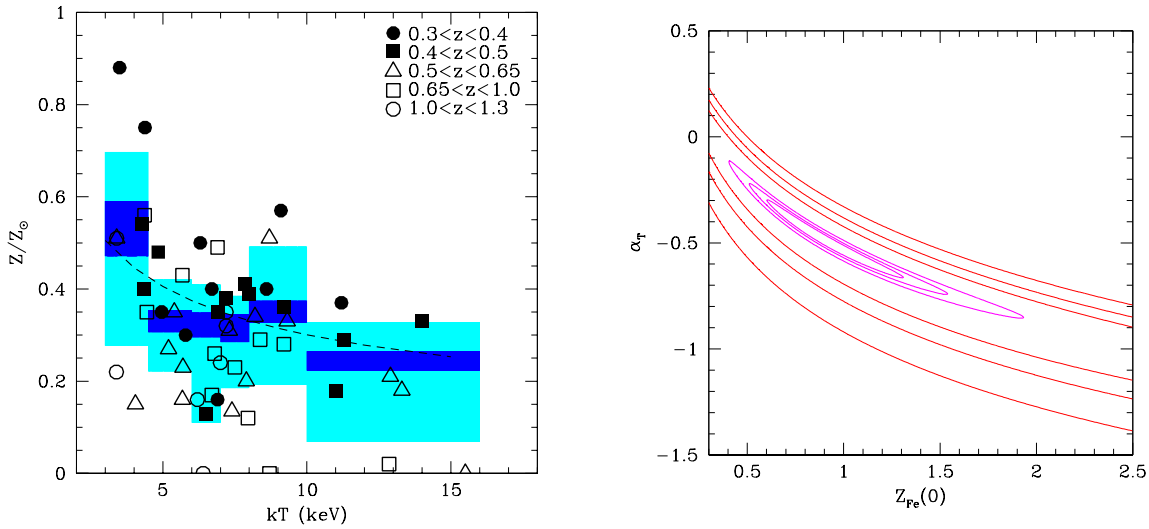

Figure 2.8: *(Left panel)* Scatter plot of best-fit iron abundance values (without error bars) versus temperature for the whole sample. The dashed line represents the best-fit metallicity-temperature relation ($Z/Z_{\odot} \simeq 0.88\,T^{-0.47}$). Shaded areas show the weighted mean (blue) and average iron abundance with *rms* dispersion (cyan) in 6 temperature bins (see Table 2.4). *(Right panel)* Best-fit confidence contour plot for the $Z - T$ relation modelled with a power law of the form $Z(T) = Z_{Fe}(0)\,T^{-\alpha_T}$. Inner contours display the 1, 2, and 3σ c.l. using errors on the weighted mean, while outer thick contours are obtained using the *rms* dispersion.

Table 2.4: Average iron abundance calculated in different temperature bins.

kT [keV][a]	$Z/Z_{\odot}$ [b] (weighted mean)	$\Delta Z/Z_{\odot}$ [c] (*rms*)
3.9 [10]	0.542 ± 0.060	0.23
5.4 [8]	0.329 ± 0.024	0.10
6.7 [11]	0.322 ± 0.027	0.17
7.5 [10]	0.317 ± 0.030	0.11
8.8 [9]	0.350 ± 0.024	0.16
12.7 [8]	0.244 ± 0.021	0.14

Notes: [a] average temperature in each bin (the number of clusters in each bin is shown in parenthesis); [b] weighted mean of the iron abundance; [c] *rms* dispersion.

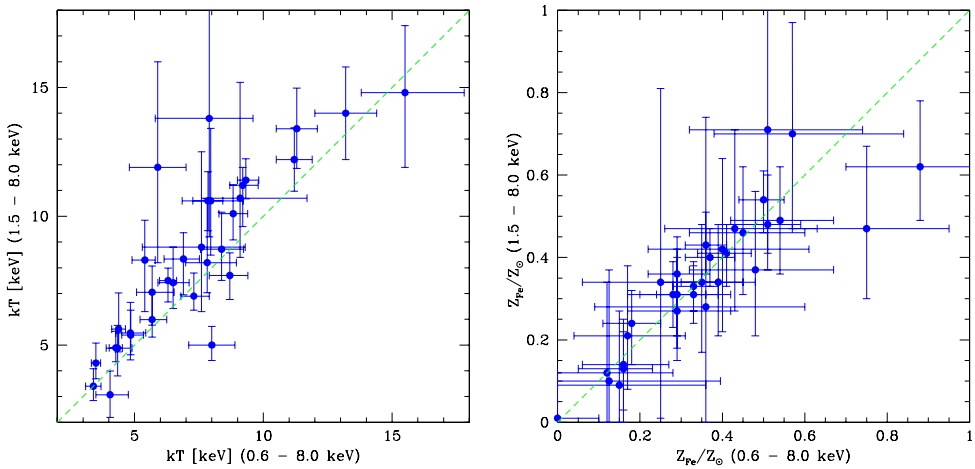

Figure 2.9: Best-fit temperatures (*left panel*) and iron abundances (*right panel*) obtained using the 1.5 – 8 keV energy range compared to the values obtained from the 0.6 – 8 keV (this paper). Dashed lines show the locus of equal temperatures and abundances. Only clusters with more than 2000 net counts (see Table 2.1) are considered here.

to our data gives $Z_{Fe}(0) = 0.88^{+0.5}_{-0.2}\, Z_\odot$ and $\alpha_T = -0.47^{+0.1}_{-0.2}$ with $\chi^2_\nu \simeq 1.8$ for 5 degrees of freedom (see the confidence contours in the slope-normalization plane in Fig. 2.8). This trend is consistent with what is found from ASCA data of a local sample of clusters for $kT > 3$ keV (see Baumgartner et al. 2005; Horner 2005). Interestingly, a similar correlation between temperature and metallicity is observed when a spatially-resolved analysis of the ICM can be performed in a single object, as in the case of the core of the Perseus cluster (see Sanders et al. 2004). However a physical explanation for this behavior is still missing.

We recall that the measure of the iron abundance in local clusters is based on both the K-shell and the L-shell complex, at 6.7 – 6.9 keV and between 1 and 2 keV, respectively. It has been pointed out that a diagnostic based mostly on the L-shell, as in the case of spectra with a significant low temperature component, is more uncertain (Renzini 1997). In our high redshift sample, we expect to be sensitive only to the iron K-shell complex. Indeed, when we fit the spectra cutting energies below 2 keV rest-frame, we find that the best-fit metallicities are consistent with those found within the 0.6 – 8 keV range (observed frame) used throughout the paper, as shown in Fig. 2.9. We notice that when the low energy range is removed, errors on the temperatures become larger, with a clear tendency to higher values. This trend is expected since higher temperature spectral shapes can be accommodated more easily than lower ones. On the other hand, iron abundances hardly change, except for the two most iron-rich clusters, ZW 0024 and V 1416. This may indicate that in these two objects the high iron abundance could be associated with a low temperature component. However, in these cases a separate analysis in two annuli is possible and we do not find a clear enhancement of the iron abundance in the inner regions.

The observed trend between Z_{Fe} and T is still a matter of debate. It may be linked to the observed decrease in the star formation efficiency with increasing cluster mass as reported in Lin et al. (2003). The modelization of this trend goes beyond the scope of this work.

2.3.4 The evolution of the iron abundance via combined spectral analysis

In Fig. 2.10 we show the iron abundance best-fit values for all the sources in the sample. When focusing on the highest redshift bin, it is worth noticing that at $z > 1$ we find clear detections of the Fe K line in the spectra of CL J1415 ($z = 1.030$, $Z_{Fe} > 0$ at the 90% c.l.), of RDCS J1252 ($z = 1.235$, $Z_{Fe} > 0.2\, Z_\odot$ at the 90% c.l.), and of the two clumps of RX J1053 ($z = 1.134$, $Z_{Fe} > 0.1\, Z_\odot$ at the 90% c.l.). In the spectra of the four other clusters, we do not have separate detections of the iron line, but all measurements are consistent within 1σ with $Z_{Fe} \simeq 0.3\, Z_\odot$. Therefore, at present, we have a much better estimate of the metal content of clusters at $z \simeq 1$ than in T03, where the iron line at $z > 1$ was only firmly detected in the two clumps of RX J1053.

We find a $\sim 3\sigma$ negative correlation between iron abundance and redshift, with a Spearman's rank

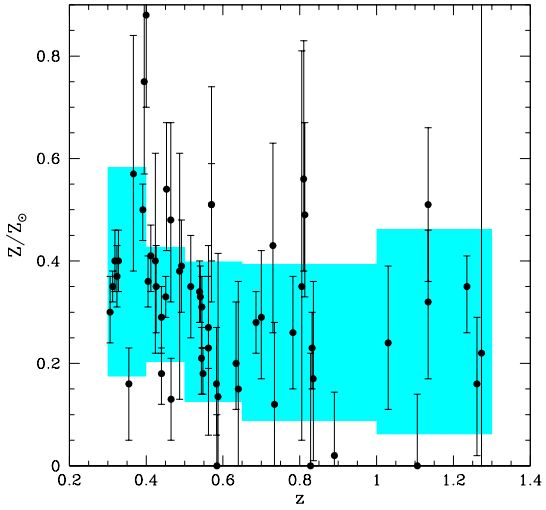

Figure 2.10: Iron abundance plotted versus redshift for the 56 clusters of the sample. Shaded areas show the *rms* dispersion around the weighted mean of the iron abundance in the 5 redshift bins defined in the text. Error bars refer to a 1σ confidence level.

coefficient of $r_s = -0.40$ for 54 degrees of freedom (probability of a null correlation $p = 0.0023$). This correlation is stronger than the weak hint (less than a 2σ c.l.) of anticorrelation found in T03. We verified that, if we calculate the Spearman's rank coefficient only for the 19 clusters analyzed in T03, using the newly revised temperature and abundances (consistent with the old ones as shown in Fig. 2.2), we again obtain very weak correlation ($r_s = -0.25$ for 17 degrees of freedom, probability of no correlation $p = 0.30$), which is therefore consistent with the results reported in T03. This confirms that our new results should not be ascribed to updated calibrations, but rather to the larger size of the sample, particularly at $z < 0.5$.

The decrease in Z_{Fe} with redshift becomes more evident by computing the average iron abundance as determined by a *combined* spectral fit in a given redshift bin. This technique is similar to the stacking analysis often performed in optical spectroscopy, where spectra from a homogeneous class of sources are averaged together to boost the S/N, thus allowing the study of otherwise undetected features. In our case, different X-ray spectra cannot be stacked due to their different shape (different temperatures). Therefore, a simultaneous spectral fit is performed leaving temperature and normalization free to vary for each object, and using a unique metallicity value for all the clusters in the subsample.

We note that the scatter of the best-fit values around the mean in each redshift bin is, in some cases, larger than the typical statistical errors on single measurements. This is expected on the basis of the $Z - T$ correlation, as found in Sect. 2.3.3. The reduced χ^2 obtained by assuming that measurements are scattered around the weighted average is between 2 and 3 in the first two bins, implying the presence of intrinsic scatter comparable to the typical statistical error, while it is ~ 1 above $z \simeq 0.5$, since here the typical statistical error is larger than the intrinsic scatter component. By assuming a unique value of Z_{Fe} in the combined fit, however, we intend to provide an average value of the metallicity over large cluster volumes as a function of redshift.

A plot of the combined iron abundance measured in each redshift bin is shown in Fig. 2.11. To verify the robustness of our results, we computed the weighted average from the single source fits in each redshift bin. The best-fit values resulting from the *combined* fits are always consistent with the weighted means (listed in Table 2.5) within 1σ, except for the bin at $z \sim 0.6$, which is lower. We also checked that, if the two clusters with the highest Z_{Fe} (i.e. ZW 0024 and V1416, see Sect. 3.3) are removed from the fit, the average Z_{Fe} value in the first redshift bin is only slightly changed (at the level of $\sim 3\%$).

From a visual inspection of Fig. 2.11, we notice a continuous trend of decreasing iron abundance from $z \simeq 0.3$ to $z \simeq 1.2$. While a constant value $\langle Z_{Fe} \rangle \simeq 0.25\, Z_\odot$ is a good fit at $z > 0.5$, the iron abundance is significantly higher at $z < 0.5$, the redshift range over which the statistics of our sample increased most with respect to T03. In addition, we now have a firm measurement of the average iron abundance at

Table 2.5: Average iron abundance in different redshift bins resulting from combined fit and weighted mean.

$\langle z \rangle$ [a]	$Z/Z_\odot$ [b] (combined fit)	$Z/Z_\odot$ [c] (weighted mean)	$\Delta Z/Z_\odot$ [d] (*rms*)
0.206 [9]	$0.427^{+0.003}_{-0.011}$	0.416 ± 0.009	0.08
0.350 [10]	$0.387^{+0.013}_{-0.012}$	0.379 ± 0.019	0.20
0.447 [12]	$0.330^{+0.017}_{-0.012}$	0.318 ± 0.020	0.11
0.572 [15]	$0.306^{+0.017}_{-0.033}$	0.260 ± 0.020	0.13
0.787 [12]	0.244 ± 0.025	0.251 ± 0.035	0.15
1.167 [7]	$0.265^{+0.05}_{-0.04}$	0.28 ± 0.048	0.15

Notes: [a] average redshift of each bin (the number of clusters in each bin is shown in parenthesis); [b] iron abundance from combined fit with 1σ errors; [c] iron abundance from weighted mean; [d] *rms* dispersion.

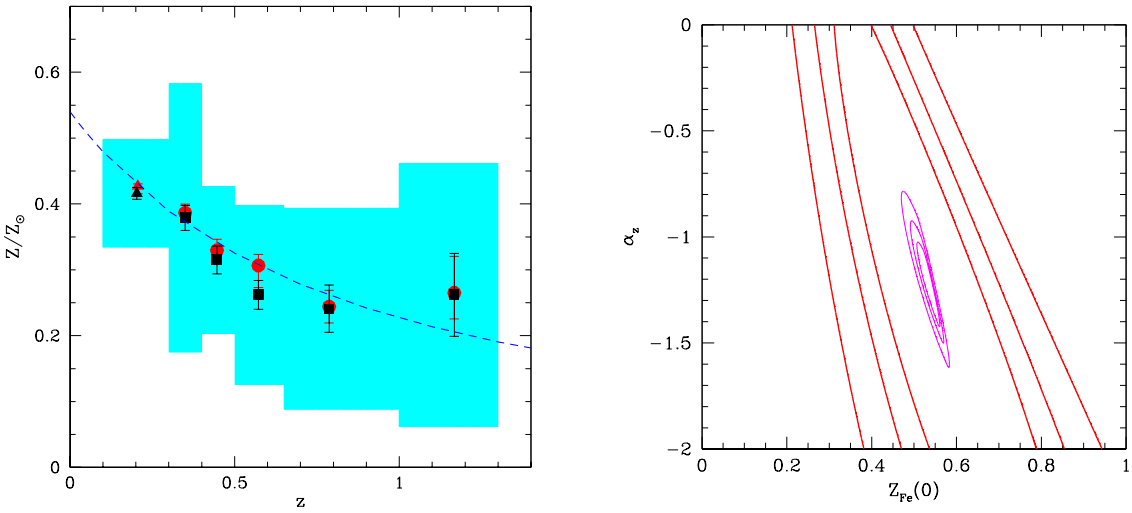

Figure 2.11: *(Left panel)* Mean iron abundance from combined fits within five redshift bins defined in the text (red circles) compared with the weighted average of single-source measurements in the same bins (black squares). The triangles at $z \simeq 0.2$ are based on the low-z sample described in Sect. 2.3.5. Error bars refer to the 1σ confidence level. Shaded areas show the *rms* dispersion. The dashed line indicates the best fit over the 6 redshift bins for a simple power law of the form $\langle Z_{Fe} \rangle = Z_{Fe}(0)\,(1+z)^{-\alpha_z}$ with $\alpha_z \simeq 1.25$. *(Right panel)* Best-fit confidence contours plot for the metallicity as a function of redshift (including the additional low-z point) modelled with a power law of the form $Z(z) = Z_{Fe}(0)\,(1+z)^{-\alpha_z}$. Thick inner contours display the 1, 2, and 3σ c.l. using the results of the combined fits, while thin outer contours are obtained using the *rms* dispersion.

redshift $z \simeq 0.8$ and $z \simeq 1.2$, reinforcing the results of T03; in particular, the iron abundance in the most distant clusters is still consistent with the value $Z_{Fe} = 0.3\,Z_{\odot}$ within 1σ.

Given the negative correlation between iron abundance and temperature found in our sample (see Sect. 2.3.3), we first verified whether the evolution with redshift is due to the presence of low-temperature clusters in the low redshift bins. By excluding clusters with $kT < 5$ keV from the plot, the same results are obtained, as expected from the lack of correlation betwen the average temperature and redshift found in Sect. 2.3.2.

We also note that this trend points towards $\langle Z_{Fe} \rangle \sim 0.5\,Z_{\odot}$ at low-z, which is higher than the often-reported value $Z_{Fe} \simeq 0.3\,Z_{\odot}$. The reason is that we are measuring Z_{Fe} in the inner regions of clusters, where it reaches values significantly higher than $0.3\,Z_{\odot}$, particularly in cool-core clusters (see Vikhlinin et al. 2005), which constitute about 2/3 of the local population. In order to show that the average iron abundance in low-z clusters, when analyzed with our procedure, confirm the trend seen in the high-z sample, we add a point at $\langle z \rangle \simeq 0.2$ including 9 clusters, as described in detail in Sect. 2.3.5.

A fit with a constant iron abundance value over the entire redshift range is unacceptable. If we model the evolution (including the additional low-z point, using the values from the combined fits) with a simple power law as

$$\langle Z_{Fe} \rangle \simeq Z_{Fe}(0)\,(1+z)^{-\alpha_z}\,, \tag{2.4}$$

the best-fit values obtained are $Z_{Fe}(0) = 0.54 \pm 0.04\,Z_{\odot}$ and $\alpha_z = 1.25 \pm 0.15$ ($\chi^2_{\nu} = 0.9$), implying a decrease by a factor of ~ 2 between $z = 0.3$ and 1.2. The evolution ($\alpha_z < 0$) is significant only at 1σ level when the *rms* dispersion is used instead of the errors on the combined fits (see confidence contours in Fig. 2.11). However, the *rms* dispersion is greatly overestimating the uncertainties on the average values. Consistent best-fit results are obtained if the lowest redshift point is excluded from the fit or if weighted mean values are used.

2.3.5 The "local" iron abundance of the ICM

An important issue to address is how our findings at $z > 0.3$ compare with the *local* iron abundance, which is traditionally quoted to be $Z_{Fe} \simeq 0.3\,Z_{\odot}$ (Renzini 1997) in the units following Anders & Grevesse (1989). The spatially-resolved spectroscopy of local clusters obtained with the *Chandra* and XMM-*Newton* satellites shows a complex distribution of the metals within the inner regions. The large differences in iron abundances and gradients from cluster to cluster lessens the meaning of the adoption of a single canonical value for the average iron content of the ICM in the local Universe. The value $Z_{Fe} \simeq 0.3\,Z_{\odot}$ is typically observed only in non cool-core clusters or in the outer regions (> 100 kpc) of cool-core clusters (see Tamura et al. 2004 for XMM-*Newton* and Vikhlinin et al. 2005 for *Chandra* data). The central peak of iron abundance reaches values of $Z_{Fe} \simeq (0.6 - 0.8)\,Z_{\odot}$ in the cores of cool-core clusters, which have a typical size of 100 kpc (see De Grandi et al. 2004; Vikhlinin et al. 2005), whereas Z_{Fe} decreases to $\simeq 0.3\,Z_{\odot}$ in the outer regions. On the other hand, the iron abundance appears to be constant, $Z_{Fe} \simeq 0.2 - 0.3\,Z_{\odot}$, in non cool-core clusters. As a result, particular care should be used when comparing our measurements with the local values of Z_{Fe} from the literature.

Since the extrapolation of the average Z_{Fe} at low-z points towards $Z_{Fe}(0) \simeq 0.5\,Z_{\odot}$, we need to explain the apparent discrepancy with the oft-quoted canonical value $\langle Z_{Fe} \rangle \simeq 0.3\,Z_{\odot}$. As mentioned in Sect. 2.3.4, the discrepancy is due to the fact that our average values are computed within $r \simeq 0.15\,R_{vir}$, where the iron abundance is boosted by the presence of metallicity peaks often associated to cool cores. The regions chosen for our spectral analysis, are larger than the typical size of the cool cores, but smaller than the typical regions adopted in studies of local samples.

This can be proved by analyzing the inner regions ($r < 0.15\,R_{vir}$) of a sample of clusters at $z < 0.3$. We selected a small subsample of 9 clusters at redshift $0.1 < z < 0.3$, including 7 cool-core and 2 non cool-core clusters, a mix that is representative of the low-z population. These clusters, listed in Table 2.6, have been also analyzed by Baldi et al. (2007) for a separate project aimed at obtaining spatially-resolved spectroscopy. Here we analyze a region within $r = 0.15\,R_{vir}$ in order to probe the same regions probed at high redshift. We used this small control sample to add a low-redshift point in our Fig. 2.11, which extends the Z_{Fe} evolutionary trend.

Table 2.6: Spectral fit results for the low-z sample with the `tbabs(mekal)` model.

Cluster	z	kT [keV][a]	$Z/Z_{\odot}$ [b]	N_H [cm^{-2}][c]	χ^2_r [d.o.f.][d]	NHP[e]
Abell 1413	0.143	7.1 ± 0.1	0.39 ± 0.02	2.18×10^{20}	1.55 [477]	10^{-13}
Abell 907	0.153	5.2 ± 0.1	0.53 ± 0.03	5.36×10^{20}	1.37 [431]	10^{-7}
Abell 2104	0.155	13.9 ± 0.5	$0.53^{+0.04}_{-0.07}$	8.69×10^{20}	1.35 [423]	10^{-6}
Abell 2218	0.176	7.9 ± 0.3	0.26 ± 0.03	3.26×10^{20}	1.09 [347]	0.111
Abell 963	0.206	7.0 ± 0.2	0.43 ± 0.03	1.40×10^{20}	1.09 [341]	0.113
Abell 2261	0.224	$7.5^{+0.4}_{-0.2}$	$0.51^{+0.03}_{-0.05}$	3.28×10^{20}	1.07 [329]	0.169
Abell 2390	0.228	9.1 ± 0.1	$0.40^{+0.03}_{-0.02}$	6.81×10^{20}	1.50 [479]	10^{-12}
Abell 1835	0.253	7.2 ± 0.2	$0.41^{+0.03}_{-0.04}$	2.32×10^{20}	0.99 [291]	0.527
ZwCl $1021.0+0426$	0.291	6.2 ± 0.1	$0.39^{+0.03}_{-0.03}$	3.02×10^{20}	1.51 [396]	10^{-10}

Notes: [a] temperature; [b] iron abundance in solar units by Anders & Grevesse (1989); [c] local column density, always fixed to the Galactic value by Dickey & Lockman (1990); [d] reduced chi-square and degrees of freedom obtained after binning the spectra to 20 counts per bin; [e] null-hypothesis probability. Errors refer to the 1σ confidence level.

2.4 Discussion

The main result of this work is that the cosmic average of Z_{Fe} in the central regions ($R < 0.3\,R_{vir}$) of clusters significantly decreases with redshift out to $z \simeq 0.5$, remaining constant out to $z \simeq 1.3$ at the level of $Z_{Fe} \simeq 0.25$. Given the complex thermal and chemical structures observed in bright local clusters, a main concern is whether our analysis might be affected by evolution in the occurrence of temperature/metallicity gradients in the cluster population. The assumption of a single-temperature `mekal` model for the inner $0.3\,R_{vir}$ may well be too simplistic, and it may introduce systematic biases in the recovered Z_{Fe} values. In order to clarify this issue, we investigate possible biases in our fitting procedure in Appendix B using a large set of simulated spectra in the typical S/N regime of our high-z clusters. We find that different S/N values do not introduce any significant bias. In particular, spectra with lower S/N (occurring mostly at high-redshift) tend to give slightly higher Z_{Fe} compared to the input values, therefore opposite to the observed trend (see Fig. B.1).

In Appendix B we also investigate the cases of a two-temperature ICM with a single Z_{Fe} and of a two-temperature ICM with higher Z_{Fe} associated with the colder component, analyzed with a single-temperature `mekal` model. Here the key parameter is the ratio of the emission measure of the two components. This quantity is difficult to model, so that here we assume a few representative values ranging from 0.3 to 0.75.

In both cases we measured slightly higher temperatures at higher redshifts, due to the fact that for high-redshift clusters, the signature of the cold component is partially redshifted below the adopted energy range ($E > 0.6$ keV). We also find a mild trend toward lower Z_{Fe} at $z \sim 1$ compared to $z \sim 0.6$. This effect is limited to be $\leq 30\%$, and therefore it cannot fully explain the observed decrease even under the extreme assumption that *all* the clusters in the sample had steep temperature gradients with a central abundance peak. To sum up, these simulations show that the presence of temperature and abundance gradients, *if their occurrence is constant through the population of clusters at different redshifts*, does not introduce significant bias into our measure of the evolution of Z_{Fe}.

Furthermore, we investigate whether the evolution of Z_{Fe} could be due to an evolving fraction of clusters with cool cores, which are known to be associated with iron-rich cores (see De Grandi et al. 2004) and which amount to more than 2/3 of the local clusters (see Bauer et al. 2005). For example, the evolution of the mass in iron in the central peak, which is about $20-30\%$ of the total, may be associated with the star formation product of the central galaxy alone (see De Grandi et al. 2004).

In order to use a simple characterization of cool-core clusters in our high-z sample, we computed the ratio of the fluxes emitted within 50 and 500 kpc ($C \equiv f(r < 50\,kpc)/f(r < 500\,kpc)$ computed as the integral of the surface brightness in the $0.5-5$ keV band (observer frame). This quantity ranges between 0 and 1 and it represents the relative weight of the central surface brightness. Higher values of C are expected if a cool core is present. If the decrease in Z_{Fe} with redshift is associated to a decrease in the number of cool-core clusters for higher z, we would expect to observe a positive correlation between Z_{Fe} and C and a negative correlation between C and redshift. In Fig. 2.12 we plot Z_{Fe} as a function of C for our sample. We find that in our sample there is no correlation between metallicity and C with a Spearman's coefficient of $r_s = 0.02$ (significance of $\sim 0.2\sigma$) nor one between C and redshift ($r_s = -0.11$,

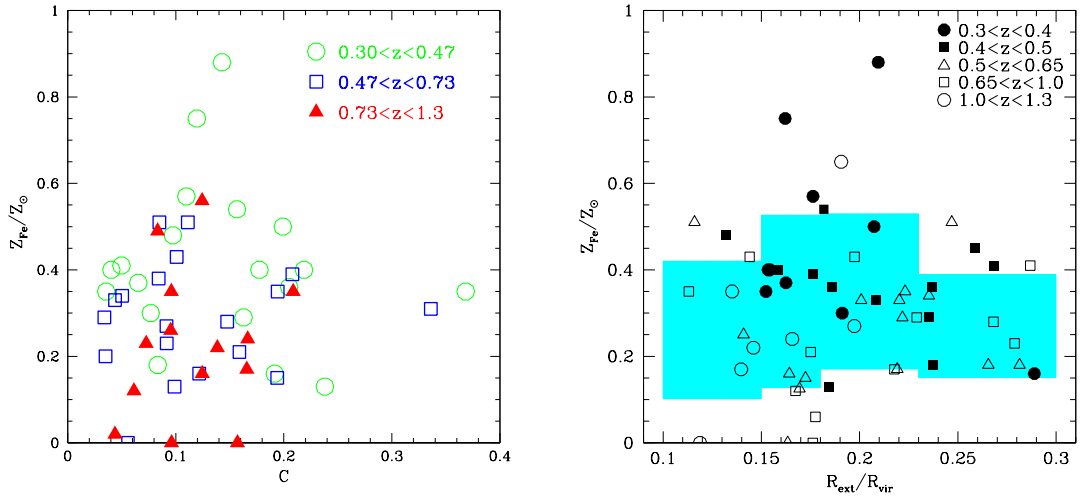

Figure 2.12: *(Left panel)* Iron abundance plotted versus $C \equiv f(r < 50\,kpc)/f(r < 500\,kpc)$. Clusters within different redshift bins are coded with different symbols. *(Right panel)* Iron abundance plotted versus the ratio R_{ext}/R_{vir}. Shaded areas show the *rms* dispersion around the average iron abundance in four bins.

a level of confidence of 0.8σ).

The absence of strong correlations between C and iron abundance or between C and redshift suggests that the mix of cool cores and non cool cores over the redshift range studied in the present work cannot justify the observed evolution in the iron abundance. We caution, however, that a possible evolution of the occurrence of cool-core clusters at high redshift may still partially contribute to the observed evolution of Z_{Fe}. In other words, whether the observed evolution of Z_{Fe} is contributed entirely by the evolution of the mass of iron or is partially due to a redistribution of iron in the central regions of clusters is an open issue to be addressed with a proper and careful investigation of the surface brightness of the high-z sample.

A final check is provided by the scatter plot of Z_{Fe} versus R_{ext}/R_{vir}, shown in Fig. 2.12. We do not detect any dependence of Z_{Fe} on the extraction radius adopted for the spectral analysis. In particular, we find that clusters with smaller extraction radii do not show higher Z_{Fe} values.

As a further confirmation, a recent work by Maughan et al. (2007) showed that the evolution of the iron abundance with redshift can be traced even if the central regions ($r < 0.15\,R_{500}$, corresponding to the typical size of a cool core) are excluded.

Together with the previous discussion of possible selection biases of our sample, all these tests concur to indicate that the observed evolution of the iron abundance is a genuine signature of some physical processes associated with the production and release of iron into the ICM.

This finding may be directly interpreted in terms of the cosmic star formation history (see Ettori 2005) for high assumed values of the time delay of SNe Ia (see Dahlen et al. 2004), which are expected to be the main contributors of iron. Other works (e.g. Mannucci et al. 2006) argue that the data on (i) the evolution of the SN Ia rate with redshift, (ii) the enhancement of the SN Ia rate in radio-loud early type galaxies, and (iii) the dependence of the SN Ia rate on the colors of the parent galaxies suggest the existence of two populations of progenitors for SN Ia. One population is expected to explode soon after the stellar birth on a time scale of 10^8 years and can significantly pollute the ICM with iron at high redshift. The second population contributes to late enrichment with an exponential decay time of ~ 3 Gyrs. Following the argument described in Ettori (2005), we note that the rates adopted by Mannucci et al. (2005) predict a flatter distribution of the iron abundance as function of redshift than the rates tabulated in Dahlen et al. (2004), with a milder negative evolution still partially consistent with our measurements. Using detailed chemical evolution models, Loewenstein (2006) has recently interpreted the significant enrichment of the ICM at $z \simeq 1$ as direct evidence of prompt star formation in spheroids with a top-heavy IMF. Moreover, these models generally predict a significant increase in the iron abundance between $z = 0$ and $z = 1$, in qualitative agreement with our results.

Alternatively, the evolution in Z_{Fe} occurring in the 5 Gyr spanned by our sample may be ascribed to some dynamical processes that transfer the metal-enriched gas from the intergalactic medium of the cluster galaxies to the hot phase of the ICM. Mechanisms such as ram pressure (Domainko et al. 2004; Cora 2006) or tidal stripping (e.g. Murante et al. 2004) are currently being investigated with numerical simulations (see also Valdarnini et al. 2003; Tornatore et al. 2004). The same mechanisms are often invoked to explain the morphological evolution of the cluster galaxies' population.

2.5 Conclusions

We have presented the spectral analysis of 56 clusters of galaxies at intermediate-to-high redshifts observed by *Chandra* and XMM-*Newton* (see Balestra et al. 2007). This work improves a previous analysis aimed at tracing the evolution of the iron content of the ICM out to $z > 1$ (Tozzi et al. 2003), by substantially extending the sample. The main results of this work can be summarized as follows:

- We determine the average ICM iron abundance with a $\sim 20\%$ uncertainty at $z > 1$ ($Z_{Fe} = 0.27 \pm 0.05\, Z_{\odot}$), thus confirming the presence of a significant amount of iron in high-z clusters. Z_{Fe} is constant above $z \simeq 0.5$, the largest variations being measured at lower redshifts.
- We find a significantly higher average iron abundance in clusters with $kT < 5$ keV, in agreement with trends measured in local samples. For $kT > 3$ keV, Z_{Fe} scales with temperature as $Z_{Fe}(T) \simeq 0.88\, T^{-0.47}$.
- We find significant evidence of a decrease in Z_{Fe} as a function of redshift, which can be parameterized by a power law $\langle Z_{Fe} \rangle \simeq Z_{Fe}(0)\,(1+z)^{-\alpha_z}$, with $Z_{Fe}(0) \simeq 0.54 \pm 0.04$ and $\alpha_z \simeq 1.25 \pm 0.15$. This implies an evolution of more than a factor of 2 from $z = 0.4$ to $z = 1.3$.

We carefully checked that the extrapolation towards $z \simeq 0.2$ of the measured trend, pointing to $Z_{Fe} \simeq 0.5\, Z_{\odot}$, is consistent with the values measured within a radius $r = 0.15\, R_{vir}$ in local samples including a mix of cool-core and non cool-core clusters. We also investigated whether the observed evolution is driven by a negative evolution in the occurrence of cool-core clusters with strong metallicity gradients towards the center, but we do not find any clear evidence of this effect. We note, however, that a proper investigation of the thermal and chemical properties of the central regions of high-z clusters is necessary to confirm whether the observed evolution by a factor of ~ 2 between $z = 0.4$ and $z = 1.3$ is due entirely to physical processes associated with the production and release of iron into the ICM, or partially associated with a redistribution of metals connected to the evolution of cool cores.

Precise measurements of the metal content of clusters over large look-back times provide a useful fossil record for the past star formation history of cluster baryons. A significant iron abundance in the ICM up to $z \simeq 1.2$ is consistent with a peak in star formation for proto-cluster regions occurring at redshift $z \simeq 4 - 5$. On the other hand, a positive evolution of Z_{Fe} with cosmic time in the last 5 Gyrs is expected on the basis of the observed cosmic star formation rate for a set of chemical enrichment models. Our data provide further constraints on the chemical evolution of cosmic baryons in the hot diffuse and cold phases.

Chapter 3

Metallicity of the ICM at high-z with XMM-*Newton*

The results presented in the previous Chapter were mostly based on *Chandra* data. The spatial resolution of *Chandra* has played an important role in that analysis allowing to resolve and, therefore, to remove the emission of point-like sources (i.e. AGN or quasars in the field) that may otherwise contaminate the continuum emission leading, for example, to wrong measurements of temperatures. However, the effective area of *Chandra* is about $5-6$ times smaller than that of XMM-*Newton*. To this respect, exploiting the XMM-*Newton* capabilities means to collect the largest possible number of photons, especially at intermediate redshift ($0.3 < z < 0.5$), in order to perform a more detailed spectral analysis. Distant clusters of galaxies observed by both X-ray satellites offer the unique opportunity to combine the larger collecting area of XMM-*Newton* with the spatial resolution of *Chandra*.

In this Chapter we present a compared *Chandra* and XMM-*Newton* analysis of the X-ray spectra of 17 clusters of galaxies at $z \geq 0.3$, which were observed by both satellites and which cover the same temperature range of the larger sample previously analyzed with *Chandra* (approximately $3 \geq kT \geq 15$ keV). With such a compared analysis, described in Sect. 3.2.2, we aim at reducing the uncertainties in the iron abundance determinantion of the ICM at high redshift thanks to the use of XMM-*Newton* and the consequent increase in the photon statistics. In Sect. 3.2.3 we make use of combined spectral analysis to estimate the average emission weighted abundances of metals other than iron at redshift $z \gtrsim 0.5$. Furthermore, the comparison of *Chandra* and XMM-*Newton* observations of high-z clusters offers a chance to investigate possible systematics in temperatures and iron abundances measured by different instruments in the low S/N regime of the observations of distant clusters of galaxies.

3.1 Sample selection and data reduction

The high-z clusters of galaxies analyzed in this Chapter are listed in Table 3.1. The selected clusters are all the high-z clusters presented in Chapter 2 for which at least one observation was also available in the XMM-*Newton* archive. We excluded MS $1621.5+2640$, V $1701+6414$ and RX J$1350.0+6007$ because their XMM-*Newton* observations were affected by too high background flaring and resulted in practically unusable exposures. We also discarded the XMM-*Newton* observations of the 3 clusters in the Lynx field (i.e. RDCS $0848+4456$, RDCS $0849+4452$ and RDCS $0848+4453$) because of their very low S/N.

Chandra observations and data reduction have been described in Chapter 2 (see Sect.2.2). We remind that the spectral analysis was performed over regions, whose size was defined in order to maximize the S/N of each source in the *Chandra* data (see Sect.2.2 and Appendix B.1 for details on how this was computed). This choice of the extraction region allowed the global properties of the clusters to be measured using the majority of the signal. This strategy was optimized for the highest redshift objects, and it was homogeneously adopted for the whole sample. In most cases the extraction radius selected was between 0.15 and 0.3 times the virial radius (see Sect.2.2).

Here, we select the same extraction regions for the XMM-*Newton* spectral analysis in order to make a straightforward comparison with the *Chandra* results.

3.1.1 XMM-*Newton* data preparation

The Observation Data Files (ODF) were processed to produce calibrated event files using the XMM-*Newton* Science Analysis System (`SAS v7.0.0`) processing task `EPCHAIN` and `EMCHAIN` for the PN and MOS, respectively.

Light curves for pattern=0 events in the $10-15$ keV band were produced for the PN and the two MOS to search for periods of high background flaring. The intervals of very high background were selected by eye and removed. Then a 3σ clipping was applied to clean the remaining data. Finally, we reextract light curves in the $0.3-10$ keV band to inspect visually and remove residual soft-proton induced flares. In Table 3.1 we list the resulting clean exposure times for the PN and the MOS.

We selected events with patterns 0 to 4 (single and double) for the PN and with patterns 0 to 12 (single, double and quadruple) for the MOS. We further removed events with low spectral quality (i.e. we applied the more restrictive screening `FLAG=0`[1]). In case of splitted or multiple observations we merged the event files for each detector separately. The resulting cleaned event files were used to create images of each detector. The images were then used to select the extraction regions for the source and the background spectra. Point-like sources can be easily removed through a comparison with the *Chandra* images. We removed circular regions of radius $15-20''$ centered at the *Chandra* position of each point-like source lying inside the extraction regions selected.

We extracted the background spectrum for each object in an annulus centered on the source position, with inner radius $3'$ and outer radius $5'$. The inner radius is large enough to avoid contamination from the fainter emission of the outskirts of the clusters. This is possible since all the clusters in our sample are at $z > 0.3$ and their angular size is always smaller than $\sim 2'$, therefore the emission outside a radius of $\sim 3'$ is not contaminated by the source. The outer radius was chosen to encompass the largest possible area avoiding, at the same time, to extend to regions which lie too far off-axis, so that the vignetting of the background photons could be neglected.

An alternative method of spectral analysis, which is often used for extended sources of larger angular size ($\gtrsim 3'-5'$), is to make use of a blank-sky background. However, it has been shown (e.g. Maughan et al. 2004) that the two methods (i.e. a *local* background or a blank-sky background) give consistent results.

Once the regions were defined, we used the `SAS` task `evselect` to extract the spectra of each cluster from the event files. Event energies were corrected for charge-transfer losses, and EPIC response matrices were generated using the `SAS` tasks `ARFGEN` and `RMFGEN`, where we take into account the spatial dependency of the response function by weighting the arf and rmf with an image of the source region[2].

3.2 Results

3.2.1 Spectral analysis

The spectra were analyzed with XSPEC v11.3.1 (Arnaud 1996) and were initially fitted with a single-temperature `mekal` model (Kaastra 1992; Liedahl et al. 1995) in which the ratio between the elements was fixed to the solar value as in Anders & Grevesse (1989). As already discussed in Sect. 2.3.1 these values for the solar metallicities have been superseded by new, more precise, measurements (e.g. Grevesse & Sauval 1998; Asplund et al. 2005), but, here, we prefer to use the units of solar abundances by Anders & Grevesse (1989) since most of the literature still refers to them. Finally, we model Galactic absorption with `tbabs` (Wilms et al. 2000).

The fits were performed over the widest possible energy range depending on the S/N of the observation. We always cut energies lower than 0.3 keV for the PN and 0.5 keV for the MOS, due to calibration uncertainties, while the high-energy cut varies with the S/N of the observation, since we are forced to exclude energy ranges where the background dominates over the source (see Table 3.2). Furthermore, due to the relatively low S/N of some observations, we notice that instrumental Kα emission lines[3] from Al (at ~ 1.5 keV) on the PN and from Al and Si (at ~ 1.7 keV) on the MOS detectors may affect the spectral analysis significantly, in particular, if an emission line is redshifted around these energies. Therefore, we always cut the energy range $1.48-1.54$ keV for the PN and $1.4-1.8$ keV for the MOS in our spectral analysis.

[1] http://heasarc.gsfc.nasa.gov/docs/xmm/abc/node7.html
[2] http://xmm.vilspa.esa.es/external/xmm_user_support/ documentation/sas_pkg_frame.shtml
[3] http://xmm.vilspa.esa.es/external/xmm_user_support/ documentation/uhb/node35.html

Table 3.1: *Chandra* and XMM-*Newton* archival observations of distant clusters of galaxies.

Cluster	z	R_{ext}[a] [″]	Chandra T_{exp}[b] [ks]	Chandra ACIS [cts][c]	XMM T_{exp}[b] [ks]	XMM PN [cts][c]	XMM MOS [cts][c]
MS 2137.3 − 2353	0.313	79.0	33	33000	7 (12)	12000	9700
ZwCl 0024.0 + 1652	0.395	64.0	40	3150	38 (48)	6500	4600
MACS J2228.5 + 2036	0.412	137.7	20	6070	18 (25)	19000	13300
MACS J1206.2 − 0847	0.440	138.0	23	11720	2 (15)	3800	13400
RX J1347.5 − 1145	0.451	128.0	58	62700	26 (34)	91000	61000
MS 0451.6 − 0305	0.539	98.4	56	16850	20 (27)	15700	10800
MS 0015.9 + 1609	0.541	98.4	67	16200	25 (34)	18000	12000
MS 2053.7 − 0449	0.583	54.1	88	2150	9 (17)	700	570
MS 1137.5 + 6624	0.782	98.4	117	4150	10 (20)	1350	1170
RX J0152.7 − 1357 S	0.828	52.7	36	570	42 (52)	2800	1400
MS 1054.4 − 0321	0.832	78.7	80	10000	21 (25)	4800	3000
RX J0152.7 − 1357 N	0.835	58.0	36	830	42 (52)	2880	1880
1WGA J1226.9 + 3332	0.890	64.0	10	2400	68 (87)	18000	10600
CL 1415.1 + 3612	1.030	39.4	89	1320	11 (16)	600	400
RX J1053.7 + 5735 E	1.134	28.2	94	300	648 (750)	4600[d]	4300[d]
RX J1053.7 + 5735 W	1.134	28.2	94	450	648 (750)	4600[d]	4300[d]
RDCS J1252 − 2927	1.235	34.5	188	850	114 (134)	2200	1100

Notes: [a] extraction radius in arcsec; [b] effective exposure time in ks after removal of high background intervals (the sixth column lists the PN effective exposure time; the MOS exposures are indicated in parenthesis); [c] number of net detected counts in the 0.3 − 10 keV band (the eighth column lists the sum of the net counts for the MOS1 and MOS2 detectors); [d] the net source counts for RX J1053.7 + 5735 refer to the sum of the eastern and western clumps (see Hashimoto et al. 2004).

The free parameters in our spectral fits are temperature, metallicity, and normalization. Local absorption is fixed to the Galactic neutral hydrogen column density, as obtained from radio data (Dickey & Lockman 1990), and the redshift to the value measured from optical spectroscopy (z in Table 3.1). We used Cash statistics applied to the source plus background[4], which is preferable for low S/N spectra (Nousek & Shue 1989).

3.2.2 Compared *Chandra* and XMM-*Newton* spectral analysis

In this section we present the results of the spectral analysis of the XMM-*Newton* data for the 17 clusters of the sample. In Table 3.2 we lists the results of the spectral fits referring to the region of radius R_{ext} (see Table 3.1), and we compare them with the *Chandra* results already presented in the previous Chapter.

The four plots in Fig. 3.1 show a comparison of the best-fit temperatures obtained from different detectors (i.e. ACIS-I/S of *Chandra*, EPIC PN and MOS of XMM-*Newton*). We find a slight tendency for the *Chandra* temperatures to be higher than the XMM-*Newton* ones below ~ 7 keV while there is an opposite tendency above ~ 7 keV. The slight systematic between the *Chandra* and XMM-*Newton* temperature measurements is almost entirely associated the PN data. In fact, the behavior for the XMM-*Newton* temperatures obtained from the combined PN+MOS fit and those from the PN only is almost identical, since the PN is dominating the statistics in the combined fits with the MOS. However, the systematic shifts in the temperatures are always small if compared to the statistical errors (of the order of $\sim 1 - 2\sigma$), with the only exception of RX J1347, where the determination of an average temperature is more problematic due to the presence of a strong temperature gradient and the high S/N of both *Chandra* and XMM-*Newton* observations. A spatially resolved spectral analysis would be more appropriate for this cluster. Indeed, we checked that a better agreement between temperature measurements can be achieved if the spectral analysis is performed over smaller size regions.

In general, temperatures from the combined fit of the two MOS detectors are in better agreement with those derived from the *Chandra* data. We also notice that the MOS temperatures are systematically above the PN temperatures. However, this effect is also small (of the order of $\sim 1\sigma$), again with the only

[4]http://heasarc.gsfc.nasa.gov/docs/xanadu/xspec/manual/ XSappendixCash.html

Table 3.2: Comparison of *Chandra* and XMM-*Newton* spectral fit results obtained with the `tbabs(mekal)` model.

Cluster	Par.	ACIS	PN	MOS1+2	PN+MOS	Energy PN (MOS)
MS 2137	kT[a]	4.96 ± 0.11	$4.62^{+0.15}_{-0.11}$	5.02 ± 0.15	4.83 ± 0.11	$0.3-7.0$ $(0.5-7.0)$
	Z[b]	0.35 ± 0.03	0.37 ± 0.05	0.41 ± 0.05	0.39 ± 0.04	
ZwCl 0024	kT	4.38 ± 0.27	4.01 ± 0.16	4.27 ± 0.21	4.10 ± 0.13	$0.3-6.0$ $(0.5-6.0)$
	Z	$0.75^{+0.20}_{-0.18}$	0.34 ± 0.06	0.15 ± 0.06	0.25 ± 0.05	
MACS J2228	kT	7.9 ± 0.6	8.28 ± 0.34	$8.88^{+0.37}_{-0.36}$	8.55 ± 0.25	$0.3-6.0$ $(0.5-6.0)$
	Z	$0.41^{+0.06}_{-0.07}$	0.22 ± 0.05	$0.26^{+0.06}_{-0.05}$	0.24 ± 0.04	
MACS J1206	kT	$11.0^{+0.7}_{-0.6}$	$13.5^{+4.5}_{-3.0}$	13.3 ± 1.0	13.3 ± 1.0	$0.3-3.0$ $(0.5-6.0)$
	Z	$0.18^{+0.05}_{-0.06}$	< 0.98	0.27 ± 0.09	0.26 ± 0.09	
RX J1347	kT	14.0 ± 0.4	9.22 ± 0.13	12.3 ± 0.3	10.35 ± 0.14	$0.3-7.5$ $(0.5-8.0)$
	Z	0.33 ± 0.04	0.23 ± 0.02	0.33 ± 0.03	0.28 ± 0.02	
MS 0451	kT	$8.2^{+0.4}_{-0.3}$	8.5 ± 0.3	9.9 ± 0.5	9.0 ± 0.2	$0.3-7.0$ $(0.5-7.0)$
	Z	0.34 ± 0.06	0.32 ± 0.06	0.23 ± 0.06	0.28 ± 0.04	
MS 0015	kT	$9.3^{+0.5}_{-0.3}$	$9.90^{+0.42}_{-0.40}$	10.86 ± 0.53	10.25 ± 0.35	$0.3-6.0$ $(0.5-6.0)$
	Z	$0.33^{+0.06}_{-0.05}$	$0.18^{+0.06}_{-0.05}$	0.25 ± 0.06	0.22 ± 0.04	
MS 2053	kT	$5.68^{+0.57}_{-0.47}$	$4.14^{+0.64}_{-0.56}$	$5.30^{+0.89}_{-0.72}$	$4.68^{+0.67}_{-0.40}$	$0.4-5.0$ $(0.5-5.0)$
	Z	$0.16^{+0.11}_{-0.10}$	$0.32^{+0.22}_{-0.16}$	$0.90^{+0.59}_{-0.40}$	$0.55^{+0.24}_{-0.19}$	
MS 1137	kT	6.8 ± 0.5	$7.7^{+1.1}_{-0.9}$	$7.4^{+1.0}_{-0.7}$	$7.38^{+0.81}_{-0.55}$	$0.3-6.0$ $(0.5-6.0)$
	Z	0.26 ± 0.11	< 0.10	$0.37^{+0.17}_{-0.15}$	$0.21^{+0.12}_{-0.10}$	
RX J0152 S	kT	$8.7^{+2.4}_{-1.8}$	$5.8^{+0.5}_{-0.4}$	$7.2^{+0.9}_{-0.7}$	6.4 ± 0.4	$0.3-5.0$ $(0.5-5.0)$
	Z	< 0.22	$0.33^{+0.14}_{-0.13}$	$0.31^{+0.15}_{-0.13}$	$0.31^{+0.09}_{-0.08}$	
MS 1054	kT	$7.5^{+0.7}_{-0.4}$	$7.8^{+0.6}_{-0.5}$	$9.3^{+0.9}_{-0.7}$	$8.48^{+0.45}_{-0.44}$	$0.3-6.0$ $(0.5-6.0)$
	Z	$0.23^{+0.07}_{-0.08}$	0.24 ± 0.10	$0.18^{+0.11}_{-0.10}$	0.21 ± 0.07	
RX J0152 N	kT	$6.7^{+1.2}_{-1.0}$	6.9 ± 0.6	$7.2^{+0.8}_{-0.6}$	7.0 ± 0.4	$0.3-5.0$ $(0.5-5.0)$
	Z	$0.17^{+0.19}_{-0.16}$	$0.14^{+0.11}_{-0.10}$	$0.37^{+0.13}_{-0.12}$	$0.26^{+0.09}_{-0.08}$	
1WGA J1226	kT	$12.9^{1.4}_{-1.2}$	11.2 ± 0.4	$12.8^{+0.8}_{-0.7}$	11.7 ± 0.3	$0.3-7.0$ $(0.5-7.0)$
	Z	$0.02^{+0.12}_{-0.02}$	0.08 ± 0.06	$0.25^{+0.08}_{-0.07}$	0.16 ± 0.05	
CL 1415	kT	$7.0^{+0.8}_{-0.7}$	$4.6^{+0.8}_{-0.5}$	$6.1^{+1.2}_{-0.9}$	$5.2^{+0.8}_{-0.6}$	$0.3-5.0$ $(0.5-5.0)$
	Z	$0.24^{+0.15}_{-0.13}$	$0.23^{+0.24}_{-0.19}$	$0.52^{+0.32}_{-0.24}$	$0.39^{+0.22}_{-0.19}$	
RX J1053 E	kT	$5.5^{+2.5}_{-1.5}$	$-$	$-$	$3.4^{+0.2}_{-0.1}$ *	$-$
	Z	< 0.23	$-$	$-$	$0.41^{+0.18}_{-0.16}$ *	
RX J1053 W	kT	$6.6^{+1.2}_{-1.0}$	$-$	$-$	4.4 ± 0.3 *	$-$
	Z	$0.65^{+0.26}_{-0.23}$	$-$	$-$	$0.62^{+0.15}_{-0.14}$ *	
RDCS J1252	kT	$7.2^{+0.4}_{-0.6}$	$4.4^{+0.4}_{-0.3}$	$7.3^{+1.3}_{-0.9}$	5.3 ± 0.4	$0.3-4.0$ $(0.5-4.0)$
	Z	$0.35^{+0.06}_{-0.09}$	$0.13^{+0.12}_{-0.10}$	$0.29^{+0.16}_{-0.15}$	$0.21^{+0.10}_{-0.09}$	

Notes: [a] Temperature in keV and [b] iron abundance in solar units by Anders & Grevesse (1989). * XMM-*Newton* results from Hashimoto et al. (2004). The last column lists the energy range selected for the spectral analysis for the PN (MOS in parenthesis). Errors refer to the 1σ confidence level.

exception of RX J1347. EPIC cross-calibration studies (Kirsch 2006) have indeed shown that there are systematic differences in the effective ares of PN and MOS that may be of the order of $5-10\%$ in certain bands, with the main differences in in the $0.3-2$ keV band (e.g. de Plaa et al. 2007).

In the four plots of Fig. 3.2 the iron abundances derived from different instruments are compared. Here, the scatter is large, but error bars are also large. In general, we do not find any clear systematic trend in the iron abundances measured by different instruments. The only noticeable discrepancies (however, only at the level of $\sim 2\sigma$) are between the iron abundance measurements of ZwCl 0024, which are most likely due to the limited photon statistics in the *Chandra* data (see also Zhang et al. 2005).

Therefore, to the purpose of the determination of the average iron content of the ICM as a function of redshift, since all the systematic errors on the iron abundance measurements are, generally, smaller than the 1σ statistical uncertainties from the fits, we can conclude that measurements of iron abundances obtained by averaging over different instruments will not be significantly affected by any systematics. While measurements of iron abundances, which are mostly based on the Fe K-shell transition at ~ 6.7 keV, are not influenced by the differences in the effective ares of PN and MOS in the $0.3-2$ keV band, the determination of abundances of other metals from the XMM-*Newton* data may still be affected by significant systematic errors (see de Plaa et al. 2007). However, as we will show in Sect. 3.2.3, these are always smaller than the statistical uncertainties.

The iron abundance-temperature correlation

In Fig. 3.3 the XMM-*Newton* iron abundance values, obtained from the combined fits of the PN and MOS data, are plotted as a function of the temperatures obtained from the same fits. For comparison they are overlayed on the weighted mean and *rms* dispersion of the iron abundance values which were calculated in different temperature bins from the spectral analysis of the *Chandra* data in the previous Chapter, Sect. 2.3.3.

Despite the smaller size (17 clusters instead of 56) and the different redshift distribution of the XMM-*Newton* sample, we performed the same tests used in the previous Chapter to assess correlations between different parameters in the *Chandra* data. In agreement with the *Chandra* results of Sect. 2.3.3, we find a significant ($\sim 3\sigma$) negative correlation between iron abundance and temperature for the XMM-*Newton* sample, with a Spearman's rank coefficient of $r_s = -0.57$ for 17 degrees of freedom (probability of no correlation $p = 0.02$). Therefore, the XMM-*Newton* data confirm that the average measured iron abundance of the ICM at high redshift is correlated with the temperature (see discussion in Sect. 2.3.3).

The evolution of the iron abundance

Fig. 3.3 shows the XMM-*Newton* results for the iron abundance best-fit values (from combined PN+MOS fits) as a function of redshift for the 17 clusters of the sample. In the same plot we display, for comparison, the average iron abundance measured in 6 redshift bins by the combined spectral analysis of the *Chandra* data described in Sect. 2.3.4. From a visual inspection of Fig. 3.3, we notice that, despite the large scatter, the XMM-*Newton* iron abundance values follow the trend of decreasing iron abundance measured by *Chandra*. We find a $\sim 1\sigma$ negative correlation between iron abundance and redshift, with a Spearman's rank coefficient of $r_s = -0.29$ for 17 degrees of freedom (probability of a null correlation $p = 0.28$). However, a constant value $\langle Z_{Fe} \rangle \simeq 0.3\, Z_{\odot}$ still gives a good fit to the 17 clusters observed with XMM-*Newton*. Therefore, with the present XMM-*Newton* sample we cannot assess the decline of the iron abundance with redshift with sufficient statistical significance and we need to extend the sample below $z \simeq 0.5$, as it was done in our previous works based on *Chandra* samples (see Tozzi et al. 2003; Balestra et al. 2007).

In order to investigate the effect of the increased statistics on the highest-redshift bin ($z > 1$), which is the measurement of Z_{Fe} with the largest uncertainties, we recalculated the weighted mean iron abundance in this bin including the new XMM-*Newton* spectral results. Compared to the previous estimate, given in Sect. 2.3.4, we added here the XMM-*Newton* observation of CL 1415 and longer exposures of RDCS 1252 and the two clusters in the Lockman Hole (eastern and western clumps of RX J1053). We obtain a slightly smaller iron abundance value with the same absolute error ($Z_{Fe} = 0.26 \pm 0.05\, Z_{\odot}$), which confirms the results obtained by the previous analysis of the *Chandra* data. The uncertainty is not reduced probably due to the increase in scatter introduced by the new Z_{Fe} measurements.

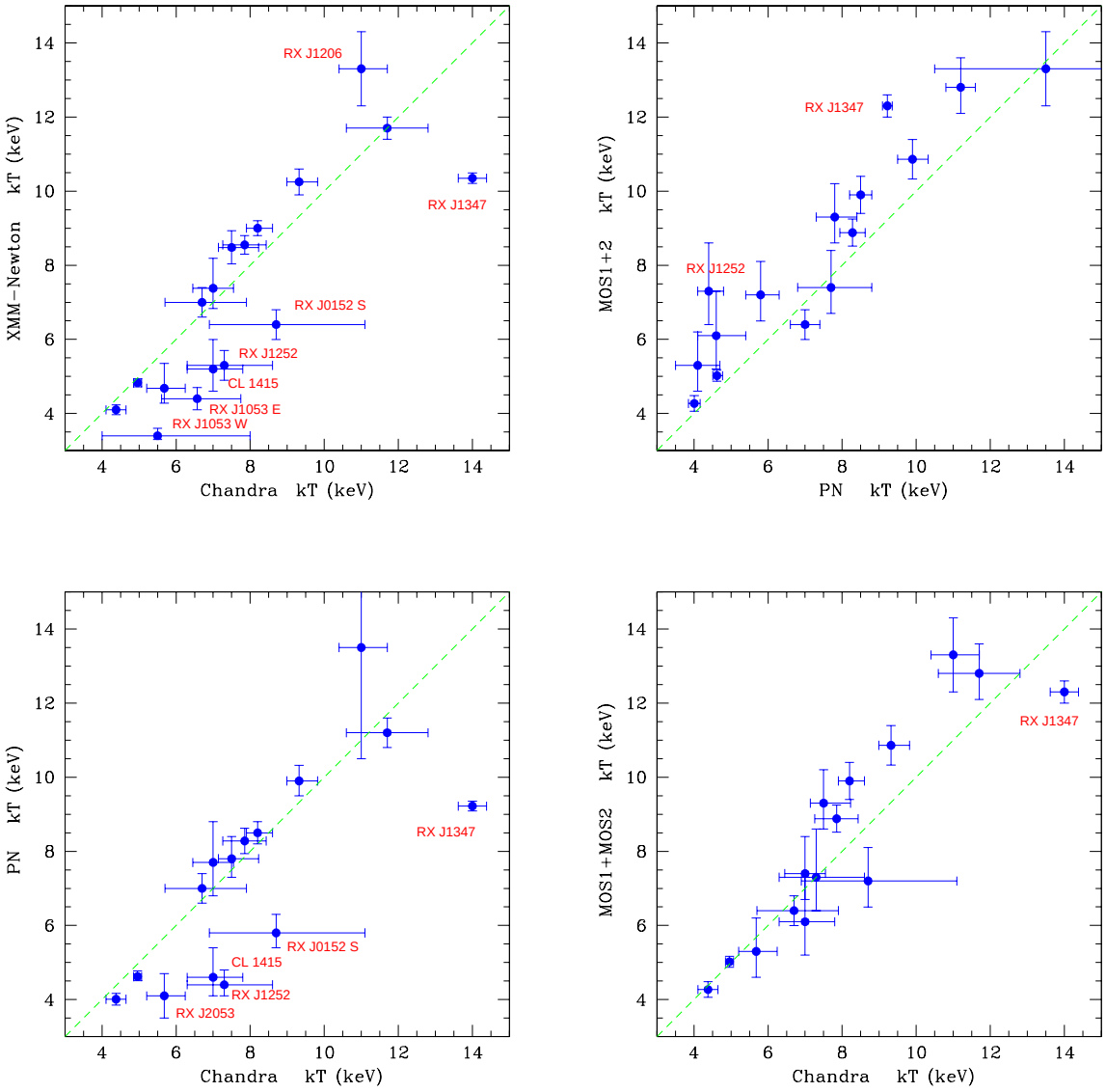

Figure 3.1: (*Top-left*) Temperature measured by XMM-*Newton* (EPIC PN+MOS) versus temperature measured by *Chandra* (ACIS-I/S). (*Top-right*) Temperature measured by the combined fit of the two MOS detectors versus temperature measured by the PN only. (*Bottom-left*) Temperature measured by the PN detector versus temperature measured by *Chandra* (ACIS-I/S). (*Bottom-right*) Temperature measured by the combined fit of the two MOS detectors versus temperature measured by *Chandra* (ACIS-I/S). Error bars refer to the 1σ confidence level.

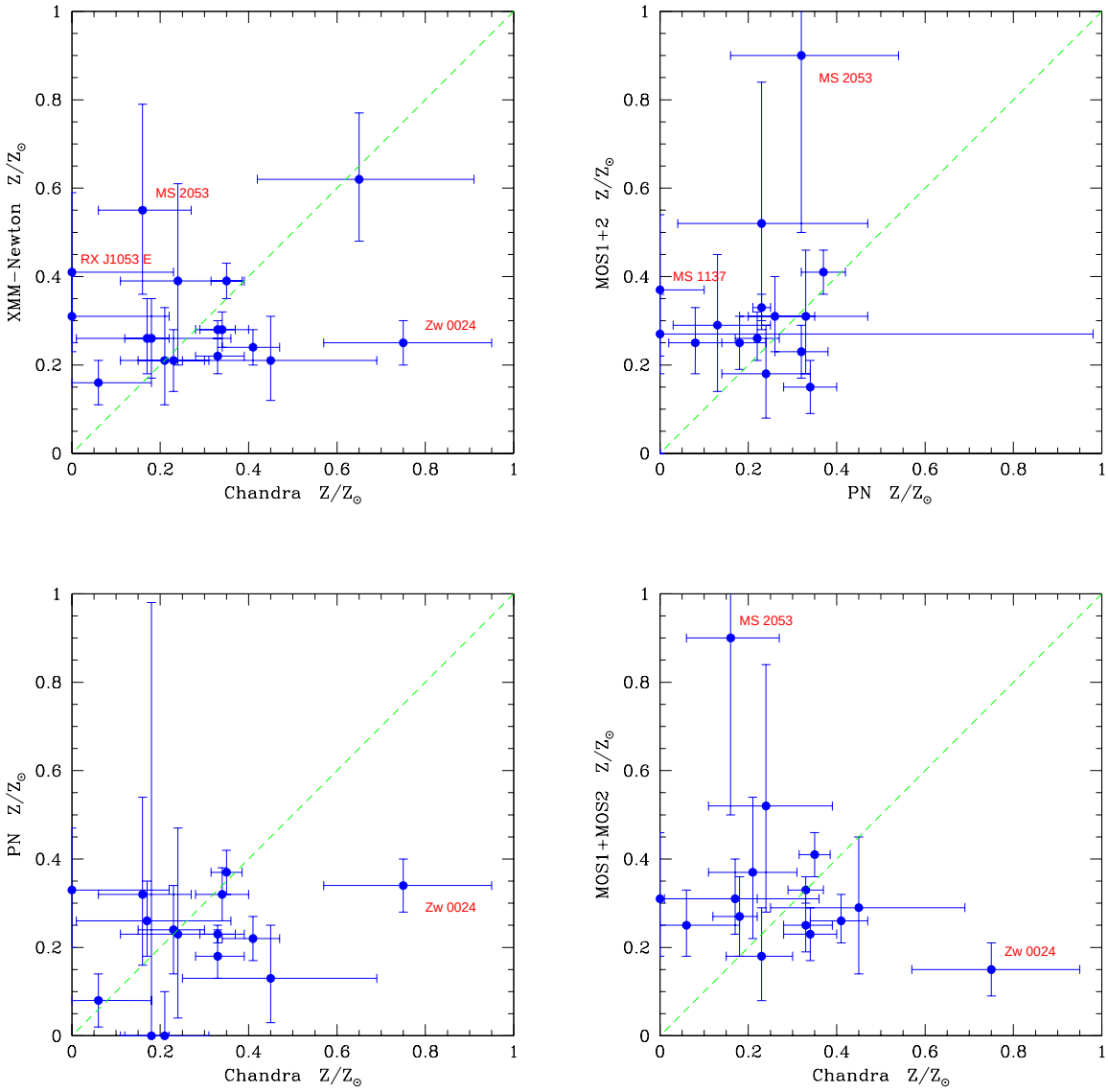

Figure 3.2: (*Top-left*) Iron abundance measured by XMM-*Newton* (EPIC PN+MOS) versus iron abundance measured by *Chandra* (ACIS-I/S). (*Top-right*) Iron abundance measured by the combined fit of the two MOS detectors versus iron abundance measured by the PN only. (*Bottom-left*) Iron abundance measured by the PN detector versus iron abundance measured by *Chandra* (ACIS-I/S). (*Bottom-right*) Iron abundance measured by the combined fit of the two MOS detectors versus iron abundance measured by *Chandra* (ACIS-I/S). Error bars refer to the 1σ confidence level.

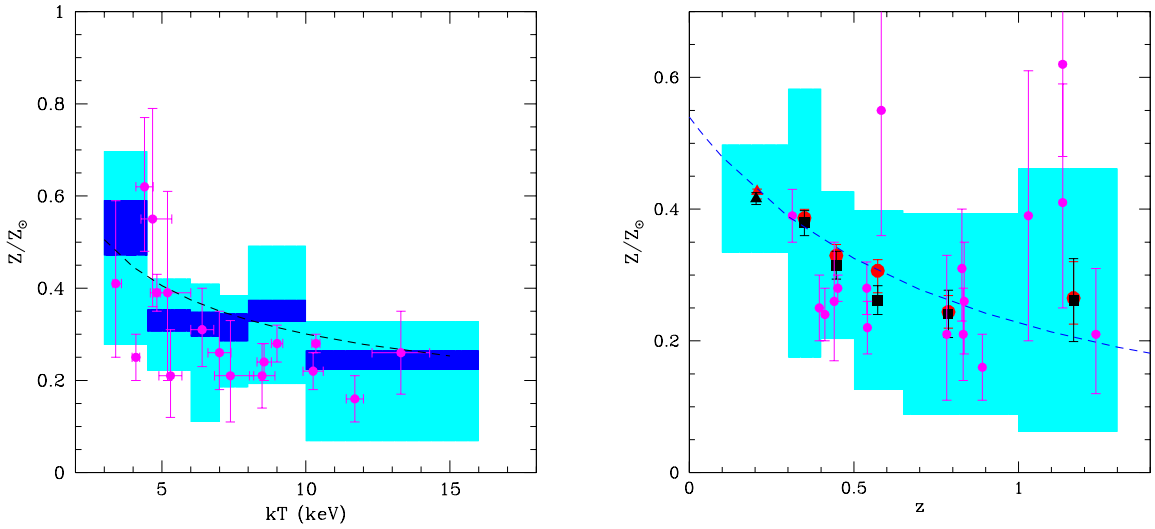

Figure 3.3: *(Left panel)* Iron abundance values versus temperature for the XMM-*Newton* sample (in magenta), compared with the best-fit metallicity-temperature relation (dashed line) derived from *Chandra* data. Shaded areas show the weighted mean (blue) and average iron abundance with *rms* dispersion (cyan) in 6 temperature bins referring to the *Chandra* data. *(Right panel)* XMM-*Newton* iron abundance measurements for single clusters (magenta circles) compared with the *Chandra* mean iron abundance from combined fits within five redshift bins (red circles) and weighted average of single-source measurements in the same bins (black squares). The triangles at $z \simeq 0.2$ are based on a low-z sample (see Baldi et al. 2007). Shaded areas show the *rms* dispersion of *Chandra* measures. The dashed line indicates the best fit over the 6 redshift bins considered in the analysis of the *Chandra* data (i.e. a simple power law of the form $\langle Z_{Fe} \rangle = Z_{Fe}(0)\,(1+z)^{-\alpha_z}$ with $\alpha_z \simeq 1.25$). In both panels error bars refer to the 1σ confidence level.

3.2.3 Abundances of other metals

To investigate the presence of other elements in the ICM at high redshift we performed spectral fits where we substitute the `mekal`, in the model described in Sect. 3.2.1, with the `vmekal` model (Mewe et al. 1985; Mewe et al. 1986; Kaastra 1992; Liedahl et al. 1995), to allow the ratios between the elements to vary.

In the fit we left the abundances of all the elements free to vary, except for H and He which were fixed to their cosmic composition. In most cases we can only derive upper limits on the abundances of metals. In Table 3.3 we list the best-fit values. We do not include in the Table unconstrained metal abundances (i.e C, N, Ar, Ca). We obtain detections at 1σ c.l., or larger (i.e. abundance measurements that differ from 0 at $> 1\sigma$ c.l.), for 8 elements other than Fe (i.e. O, Ne, Na, Mg, Al, Si, S, Ni) only for a few clusters (Mg in 10 clusters, Ne and Si in 7 clusters, O in 6 clusters, Na and Al in 4 clusters, S and Ni in 3 clusters). Apart from Na and Ni, all of these are α-elements which are mostly produced by core-collapse supernovae.

In order to evaluate the average content of α-elements in the ICM at high redshift we tried to apply the same technique used in Sect. 2.3.4, to boost the S/N for the weaker emission lines from elements other than Fe. However, in this case the task is much harder since single measurements of metal abundances have larger uncertainties, especially at $z \gtrsim 0.5$. Therefore, we concentrate only on the 5 clusters at $0.3 < z < 0.5$ (namely MS 2137, ZwCl 0024; RX J2228; RX J1206; RX J1347). We compute the average metal abundances as determined by a *combined* spectral fit in the redshift range $0.3 < z < 0.5$. The combined fit with the `vmekal` model is performed leaving temperature and normalization free to vary for each object, and linking each metal abundance to a single value for all the 5 clusters. The results of the fit are listed in Table 3.4, together with the weighted mean of the metallicities of the 5 clusters.

In Fig. 3.4 the abundances of oxygen, magnesium, silicon and sulphur, which are all the α-elements having at least two detections at more than 1σ c.l. in the redshift range $0.3 < z < 0.5$, are plotted as a function of redshift. The four plots show that, despite the large uncertainties, the average abundances of O, Si, and S can be estimated through our combined spectral analysis at $0.3 < z < 0.5$ and the spectral fit results are in agreement with the weighted mean values. The Mg abundance is more problematic, exhibiting a large scatter toward higher metallicities, which might also cause the mismatch between the result of the combined fit and the weighted mean value for this element. We notice, that for Mg abundances the scatter is much larger (a factor of ~ 2) than the typical error on the measurements, making the estimate of an average value less meaningful in this case. Therefore, we will not use our estimates of Mg abundances in the rest of our discussion.

It is worth noticing that, in the redshift range selected for the spectral analysis ($0.3 < z < 0.5$), the S (2.62 keV), Si (2.01 keV) and Mg (1.87 keV) lines are all shifted into energy bands that might be affected by systematics due to the abovementioned calibration uncertainties between PN and MOS detectors. However, the statistical errors are largely dominating, therefore we cannot investigate the effect of systematic errors on our abundance measurements, since this requires higher S/N spectra (see de Plaa et al. 2007).

An estimate of the average content of α-elements in the ICM at $0.3 < z < 0.5$ can be obtained from the combined fit described above, by linking the abundances of all the α-elements (i.e. O, Si, and S) to the same value for the 5 clusters. In this way, we obtain an average abundance of α-elements at $z \simeq 0.4$ equal to $0.17 \pm 0.09\, Z_{\odot}$, which gives $\alpha/\mathrm{Fe} \simeq 0.6$, still consistent with values observed in local clusters (see de Plaa et al. 2007).

Our estimates of the average content of α-elements in the ICM at $0.3 < z < 0.5$ can also be used, in combination with those of Fe and Ni abundances, to calculate the ratio of type Ia (SNIa) to core-collapse supernovae[5] (SNcc) at these redshifts. To this aim, we performed a series of combined fits for the 5 clusters at $0.3 < z < 0.5$, where we force the abundance ratios of O/Fe , Si/Fe, S/Fe, and Ni/Fe in the `vmekal` model to be equal to those obtained for a certain value of the fraction of type Ia supernovae (f_{SNIa}[6]), where we use the model described in Ettori (2005) for the total synthetized isotopic mass per SN event[7]. Therefore, we construct a grid of C-statistics probabilities for different values of the fraction of SNIa f_{SNIa}, from which we can derive a best-fitting value of $f_{SNIa} = 0.9 \pm 0.1$. This implies that, to reproduce the ratios of metal abundances observed in the inner regions of the 5 clusters of galaxies selected for our

[5] Type Ia supernovae are believed to arise from the explosion of a C–O white dwarf in a close binary system where the companion is either a red giant or a main-sequence star. Core-collapse supernovae, i.e. type II and Ibc supernovae, originate from the internal collapse and violent explosion of a massive short-lived star.

[6] $f_{SNIa} \equiv \frac{SNIa}{SNIa+SNcc}$, where $SNIa$ and $SNcc$ are the number of type Ia and core-collapse supernovae, respectively.

[7] See Table 1 of Ettori (2005); this model follows Nomoto et al. (1997) for the total synthetized isotopic mass per SNIa or SNcc event, with nucleosynthesis products of SNIa from the deflagration model W7 and SNcc yields integrated over the mass range $10 - 50 M_{\odot}$ with a Salpeter IMF.

Table 3.3: XMM-*Newton* spectral fit results obtained with the `tbabs(vmekal)` model.

Cluster	kT [keV]	O	Ne	Na	Mg	Al	Si	S	Fe	Ni
MS2137	$4.82^{+0.18}_{-0.35}$	$0.59^{+0.28}_{-0.26}$	< 0.7	21^{+13}_{-12}	$0.97^{+0.43}_{-0.42}$	< 7.4	< 0.31	0.48 ± 0.26	0.39 ± 0.04	$0.78^{+0.73}_{-0.70}$
ZwCl0024	4.13 ± 0.13	< 0.17	< 0.5	< 20	< 0.15	< 1.2	< 0.32	< 0.33	$0.26^{+0.05}_{-0.04}$	< 1.0
MACSJ2228	$8.73^{+0.27}_{-0.28}$	$0.62^{+0.49}_{-0.45}$	< 1.2	< 31	$2.15^{+0.73}_{-0.70}$	< 7	< 0.6	< 0.1	0.25 ± 0.04	< 0.8
MACSJ1206	10.6 ± 0.9	< 14	< 7.7	< 84	$4.2^{+1.7}_{-1.5}$	< 150	$1.88^{+0.97}_{-0.91}$	$1.93^{+1.15}_{-1.10}$	0.26 ± 0.09	< 25
RXJ1347	$10.50^{+0.15}_{-0.29}$	< 0.45	< 0.45	27 ± 10	1.17 ± 0.36	4.3 ± 3.0	$0.23^{+0.19}_{-0.18}$	< 0.5	$0.28^{+0.04}_{-0.02}$	$0.54^{+0.32}_{-0.31}$
MS0451	9.18 ± 0.26	$2.54^{+0.96}_{-0.86}$	$2.93^{+1.13}_{-1.04}$	< 59	$1.90^{+1.06}_{-0.99}$	< 13	$0.52^{+0.46}_{-0.44}$	< 0.3	0.31 ± 0.05	2.0 ± 0.9
MS0015	$10.64^{+0.40}_{-0.42}$	< 0.13	$0.99^{+0.88}_{-0.84}$	29^{+26}_{-25}	$3.08^{+0.98}_{-0.94}$	13 ± 7	< 0.8	< 1.4	0.23 ± 0.04	< 1.0
MS2053	$4.42^{+0.66}_{-0.48}$	9^{+15}_{-4}	< 7.4	0^*	< 1.7	< 46	< 3.6	< 5.9	$0.58^{+0.35}_{-0.36}$	< 11
MS1137	8.0 ± 0.9	< 1.4	$3.0^{+3.2}_{-2.4}$	100^{+95}_{-80}	$3.0^{+3.2}_{-2.7}$	< 16	< 1.7	< 1.8	$0.21^{+0.13}_{-0.11}$	< 2.5
RXJ0152S	6.7 ± 0.5	$2.9^{+3.2}_{-1.3}$	$5.0^{+4.1}_{-3.1}$	< 176	$3.3^{+2.7}_{-2.4}$	23^{+22}_{-18}	< 2.0	< 2.7	$0.36^{+0.13}_{-0.11}$	< 1.7
MS1054	$8.9^{+0.5}_{-0.9}$	< 4.7	$5.2^{+3.0}_{-2.5}$	< 117	$3.1^{+2.2}_{-2.0}$	< 23	$0.89^{+0.93}_{-0.84}$	< 1.5	0.21 ± 0.08	< 1.0
RXJ0152N	7.0 ± 0.5	$2.7^{+2.1}_{-2.0}$	$2.8^{+3.4}_{-2.7}$	< 18	< 1.5	24^{+18}_{-17}	$1.1^{+1.0}_{-0.9}$	$2.9^{+1.7}_{-1.5}$	$0.32^{+0.12}_{-0.10}$	< 2.3
1WGAJ1226	11.6 ± 0.3	0^*	< 1.1	< 14	< 1.2	0^*	$0.54^{+0.52}_{-0.51}$	< 0.9	0.16 ± 0.05	< 1.2
CL1415	5.09 ± 0.78	0^*	0^*	0^*	$4.7^{+5.5}_{-4.0}$	0^*	$3.0^{+2.4}_{-1.8}$	< 1.7	$0.32^{+0.17}_{-0.15}$	< 150
RDCSJ1252	5.4 ± 0.4	< 20	$8.6^{+3.0}_{-1.6}$	< 170	< 1.7	< 13	< 1.2	< 0.4	0.21 ± 0.10	< 4.2

Notes: Metal abundances are in solar units by (Anders & Grevesse 1989). * Unconstrained metal abundances are fixed to 0. Errors refer to the 1σ confidence level.

Table 3.4: Average metallicities for the 5 clusters at $0.3 < z < 0.5$ resulting from a combined fit with the `vmekal` model and from the weighted mean of single measurements.

Element	$Z/Z_\odot$ [a] (combined fit)	$Z/Z_\odot$ [b] (weighted mean)	$\Delta Z/Z_\odot$ [c] (*rms*)
O	0.23 ± 0.15	0.18 ± 0.13	0.30
Mg	0.93 ± 0.23	0.33 ± 0.13	1.43
Si	0.16 ± 0.14	0.16 ± 0.14	0.73
S	$0.12^{+0.14}_{-0.12}$	$0.07^{+0.09}_{-0.07}$	0.75
Fe	0.289 ± 0.014	0.30 ± 0.02	0.05
Ni	0.46 ± 0.25	0.47 ± 0.27	0.33

Notes: Metal abundances are in solar units by (Anders & Grevesse 1989). [a] Abundance from combined fit with 1σ errors; [b] abundance from weighted mean; [c] *rms* dispersion.

analysis at $0.3 < z < 0.5$, the relative fraction of SNIa must be larger than 80%. This result is consistent with other observational evidences that indicate a dominant contribution of SNIa in the central regions of galaxy clusters (e.g. Dupke & Arnaud 2001).

3.3 Discussion and conclusions

In this Chapter we presented the spectral analysis of 17 clusters of galaxies at high redshift ($z > 0.3$) observed by *Chandra* and XMM-*Newton*. This work improves our first analysis aimed at tracing the evolution of the iron content of the ICM out to $z \geq 1$ (Balestra et al. 2007), by collecting all the available XMM-*Newton* observations of the same high-z clusters analyzed in our previous work.

The main results of the analysis can be summarized as follows:

- We determine the average ICM iron abundance with a less than 20% uncertainty at $z > 1$ ($Z_{Fe} = 0.26 \pm 0.05\, Z_\odot$), thus confirming the presence of a significant amount of iron in the ICM at the highest redshifts probed to date, in agreement with the previous analysis of *Chandra* data.

- We find a significantly higher average iron abundance in clusters with $kT < 5$ keV, in agreement with trends measured in local samples and with our previous results based on *Chandra* data.

- We measure the average ICM abundance of iron ($Z_{Fe} = 0.29 \pm 0.02\, Z_\odot$), nickel ($Z_{Ni} = 0.46 \pm 0.25\, Z_\odot$), oxygen ($Z_O = 0.23 \pm 0.15\, Z_\odot$), silicon ($Z_{Si} = 0.16 \pm 0.14\, Z_\odot$), and sulphur ($Z_S = 0.12^{+0.14}_{-0.12}\, Z_\odot$) at $0.3 < z < 0.5$. These are the first measurements of abundances of elements other than Fe in the ICM at high redshift. From the ratios of O/Fe, Si/Fe, S/Fe, and Ni/Fe we infer that the fraction of supernovae type Ia at $0.3 < z < 0.5$ must be larger than 80%, which is in agreement with several evidences indicating that the dominant contribution to the metal enrichment of the central regions of the ICM is from SNIa.

In the present work, we obtained the first detections of metals other than Fe (i.e. O, Si, S, and Ni) in the ICM at high redshift ($0.3 < z < 0.5$). The measurements of abundances of α-elements at high redshift open the possibility to investigate the evolution with redshift of the relative contribution to the ICM enrichment by SNcc, which produce a relatively higher fraction of α-elements, and by SNIa, contributing mainly to Fe and Ni enrichment (see Chapter 4, Sect. 4.1). Uncertainties are still large since our present results are based on a very small sample. However, in the next future the XMM-*Newton* archive can be exploited by collecting all the available observations of high-z ($z \lesssim 0.5$) clusters and our analysis technique can be applied to a much larger sample of galaxy clusters. The increase in statistics will allow us to reduce the uncertainties on the metal abundance determinations and, therefore, to draw firmer conclusions on the relative contribution of SNIa and SNcc to the ICM enrichment as a function of cosmic time.

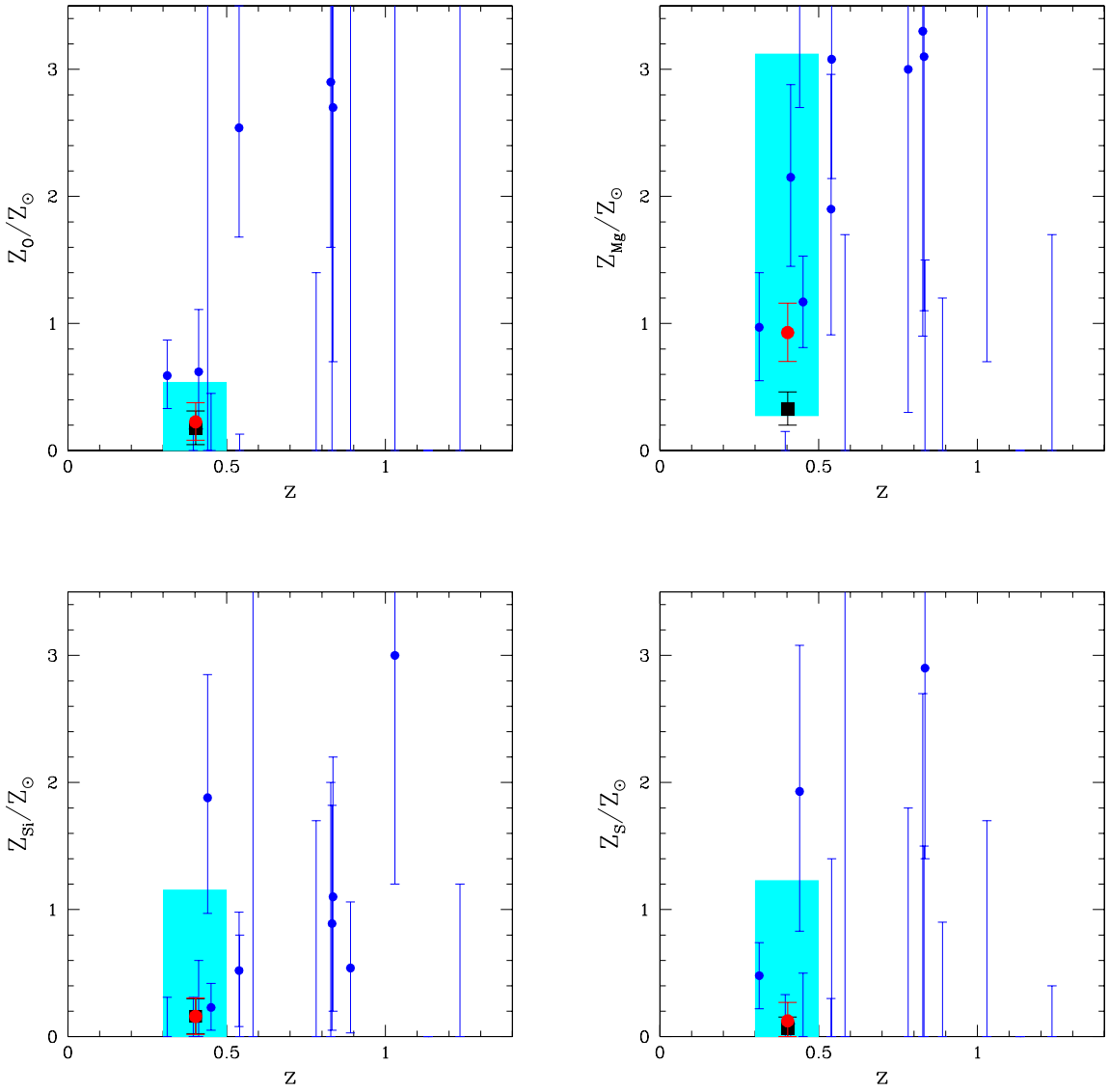

Figure 3.4: Oxygen (*top-left*), magnesium (*top-right*), silicon (*bottom-left*) and sulphur (*bottom-right*) abundances as a function of redshift. Mean elemental abundances from combined fits within $0.3 < z < 0.5$ (red circles) and weighted average of single-source measurements in the same redshift interval (black squares) are also plotted, together with the *rms* dispersion around the mean value (shaded areas) in the same redshift interval. Error bars refer to the 1σ confidence level.

Chapter 4

Modelling the iron enrichment of the ICM

The primordial cosmic gas is composed of hydrogen ($\sim$ 75% by mass), helium ($\sim$ 24%), and traces of other light elements, like deuterium, helium-3, lithium and beryllium. When this gas collapses into the dark matter halos typical of galaxy clusters ($\gtrsim 10^{14} M_{\odot}$), it undergoes shocks and adiabatic compression, reaching the typical densities ($\sim 10^{-3}$ cm^{-3}) and temperatures ($\sim 10^{8}$ K) of the ICM. Its enrichment with metals proceeds via the release to the medium of the products, ejected by supernovae explosions, of star formation activity that take place in the member galaxies.

Since, under the ICM conditions, abundances of Fe are more easily measured than those of other elements, they can be derived out to $z > 1$ (see Chapter 2) and provide the strongest current constraints on the evolution of the ICM enrichment. In the light of the results presented in Chapter 2, which provided the first evidence for an evolution with redshift, or cosmic time, in the iron content of the ICM, the chemical enrichment of the ICM can be modelled as a function of time, therefore tracing the star formation history of the cluster galaxies.

In practice, this can be done by comparing the observed iron content of the ICM, with theoretical predictions from the models. The observed iron mass can be easily computed: the iron mass enclosed within a sphere of radius R is given by the radial integral $\int_0^R \rho_{Fe}(r) dV(r)$, where ρ_{Fe} is the iron density by mass and dV is the volume of the considered element, both measured at a distance r from the center. Since the iron abundance is defined as $Z_{Fe} = n_{Fe}/n_H$ (in units of $Z_{\odot}$), where n_{Fe} and n_H are the iron and hydrogen densities (by number) respectively, the total observed iron mass in solar units can be written as:

$$M_{Fe,obs}(< R) = 4\pi A_{Fe} m_H \frac{Z_{\odot}}{M_{\odot}} \int_0^R Z_{Fe}(r)\ n_H(r)\ r^2 dr, \tag{4.1}$$

where A_{Fe} is the atomic weight of iron and m_H is the atomic unit mass.

In this chapter we describe two techniques to interpret the present, and future, data on the chemical enrichment of the ICM. We present two examples taken from the literature, which have made use of our observational constraints on the iron abundance as a function of redshift, to reconstruct the galaxy clusters' star formation history. These two recent works follow different approaches: the first, from Ettori (2005), is a phenomenological model based on the observed SN type Ia rates at high redshift (Sect. 4.1), the second, from Calura et al. (2007) is based on chemical evolution models for galaxies of different morphological type (Sect. 4.2).

4.1 A phenomenological model

The evolution of the iron content of the ICM with redshift can be directly interpreted in terms of the cosmic star formation history. The iron mass accumulated as a function of redshift can be simply computed by using models of SN rates matching the observational constraints on the rates of SNIa and SNcc at high redshifts. In this section we present results obtained by Ettori (2005), who reconstruct the history of metals' accumulation in the ICM, by using models of SNIa and SNcc rates, built in such a way that both are consistent with recent observational constraints at $z \lesssim 1.6$ and can reproduce the measured cosmic star formation rate.

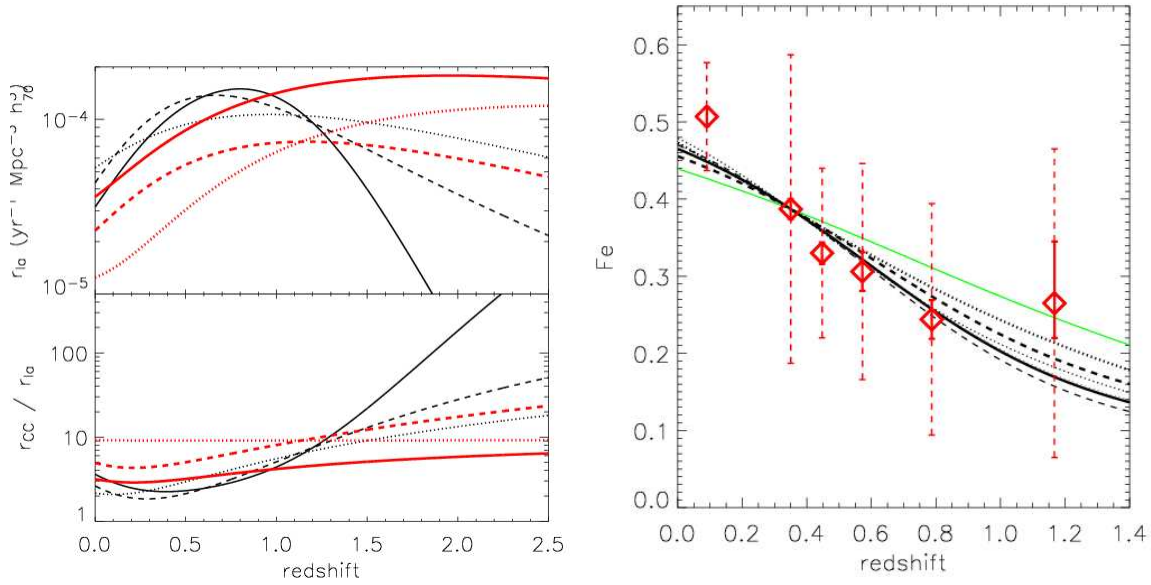

Figure 4.1: *(Left)* SNIa rates *(upper panel)* and number ratio of SNcc to SNIa *(lower panel)* as a function of redshift for different delay time distribution functions: a "narrow" Gaussian with $\tau = 4$ Gyr and $\sigma_{t_d} = 0.2\tau$ *(solid line)*; a "wide" Gaussian with $\tau = 4$ Gyr and $\sigma_{t_d} = 0.5\tau$ *(dashed line)*; an exponential of the form, $\phi(t_d) \propto \exp(-t_d/\tau)$, with $\tau = 5$ Gyr *(dotted line)*. The *solid red line* is the sum of the contribution of two populations of SNIa: "prompt" *(dotted red line)* and "tardy" *(dashed red line)* SNIa explosions (see Mannucci et al. 2006 for the parameterization of this model). Similar models are presented and discussed in Dahlen et al. (2004) and Mannucci et al. (2006). *(Right panel)* Predicted and observed iron abundance as a function of redshift. The *diamonds* refer to the median distribution of ~ 10 iron abundance measurements per redshift bin, as in Balestra et al. (2007). The normalization of the predicted evolution is here fixed equal to the abundance measurement at $z \approx 0.4$. The lines refer to different SN explosion models and delay time distribution functions: a "narrow" Gaussian model *(solid line)*, Woosley & Weaver (1995) SNcc models, case A *(thin dashed line)* and B *(thick dashed line)*, WDD2 SNIa model in Nomoto et al. (1997), wide Gaussian and $e-$folding form (*dotted lines* from thinnest to thickest). The *solid green line* is for the two-population model as in Mannucci et al. (2006).

Such SN rates, in unit of SN number per comoving volume and rest-frame year, provide on average a total amount of iron that is marginally consistent with the value measured in galaxy clusters in the redshift range $0-1$, and an evolution with redshift that is in agreement with our observational constraints up to $z \approx 1.2$ (see Fig. 4.1). All the models favour long delay times in the SNIa explosions, or may suggest the existence of two different populations of progenitors for SNIa: "prompt", which explode soon after their stellar birth and "tardy", which explode with a certain delay, as inferred by Mannucci et al. (2006).

Moreover, the predicted metals to iron ratios reproduce the measurements obtained through X-ray analysis of nearby clusters, implying that (1) about half of the iron mass and $\gtrsim 75\%$ of the nickel mass observed locally are produced by SNIa ejecta, (2) the SNIa contribution to the metal budget decreases steeply with redshift and by $z \approx 1$ is already less than half of the local amount and (3) a transition in the abundance ratios relative to the iron is present between redshifts ~ 0.5 and 1.4, with SNcc products becoming dominant at higher redshifts.

These predictions can be compared to the observational constraints on the abundance ratios relative to Fe at high redshift (up to $z \simeq 0.5$; see the XMM-*Newton* spectral analysis presented in the previous Chapter). At present, our results (see Sect. 3.2.3) indicate that the fraction of SNIa is still large ($> 80\%$) at $0.3 < z < 0.5$ in the inner regions ($< 0.3\, R_{vir}$) of the ICM. However, the relative uncertainties on these abundance ratios can be significantly reduced by enlarging the sample used for the spectral analysis. This will be subject of a future work.

4.2 Chemical evolution models for galaxies

The study of the Fe abundance in the ICM provides strong constraints on the integrated star formation history and SN rate of the cluster galaxies, as well as on the ICM enrichment mechanisms. Calura et al. (2007) have studied the evolution of the Fe content of clusters of galaxies, using chemical evolution models for galaxies of different morphological types (i.e. elliptical and S0). They assume that the ICM Fe enrichment occurs by means of galactic winds arising from elliptical galaxies and from gas stripped from the progenitors of S0 galaxies via external mechanisms, due to the interaction of the inter-stellar medium with the ICM.

In their model they assume that S0 galaxies originate from disc galaxies, in which star formation stops at a late stage owing to massive gas loss by means of some external mechanism, represented by interactions with the ICM, i.e. collisions or tidal stripping (Larson et al. 1980; Boselli & Gavazzi 2006). The model assumes that, as soon as the star formation stops, the galaxy starts to lose enriched gas at a constant rate. At the final stage of its evolution, the S0 galaxy has ejected all of its gas and consists only of a stellar disc. This scenario is supported by several observational evidences, such as the Butcher & Hoemler (1978) effect, i.e. the increase with redshift of the fraction of blue cluster galaxies, which seems strictly connected to the decrease of the fraction of cluster S0 galaxies with redshift (Dressler et al. 1997; Poggianti et al. 1999; van Dokkum et al. 2000; Fasano et al. 2000; Tran et al. 2005).

As shown in Fig. 4.2, the Fe-rich gas ejected by cluster elliptical galaxies through SN-driven galactic winds accounts for the $X_{Fe,ICM}$[1] values observed at $z > 0.5$, whereas the gas stripped from the progenitors of the S0 galaxies accounts for the increase of $X_{Fe,ICM}$ observed at $z < 0.5$. The observed $X_{Fe,ICM}$ is well reproduced assuming E+S0 cluster fractions of $f_{E+S0} = 0.81 - 0.96$, in excellent agreement with the available observations for the central regions of galaxy clusters (Dressler 1980; Dressler et al. 1997; Andreon et al. 1997; Fasano et al. 2000; Biviano et al. 2002). Furthermore, the SNIa rates inferred from the two different scenarios for SNIa progenitors tested in this work are in good agreement with the observed evolution of SNIa rate density in clusters (Gal-Yam et al. 2002; Sharon et al. 2006).

[1] $X_{Fe,ICM}$ is the Fe abundance in the ICM as a function of redshift, calculated as: $X_{Fe,ICM}(z) = \frac{\rho_{Fe,ICM}(z)}{\rho_{ICM,0.3R_{vir}}}$, where $\rho_{ICM,0.3R_{vir}}$ is the ICM mass density within $0.3\,R_{vir}$.

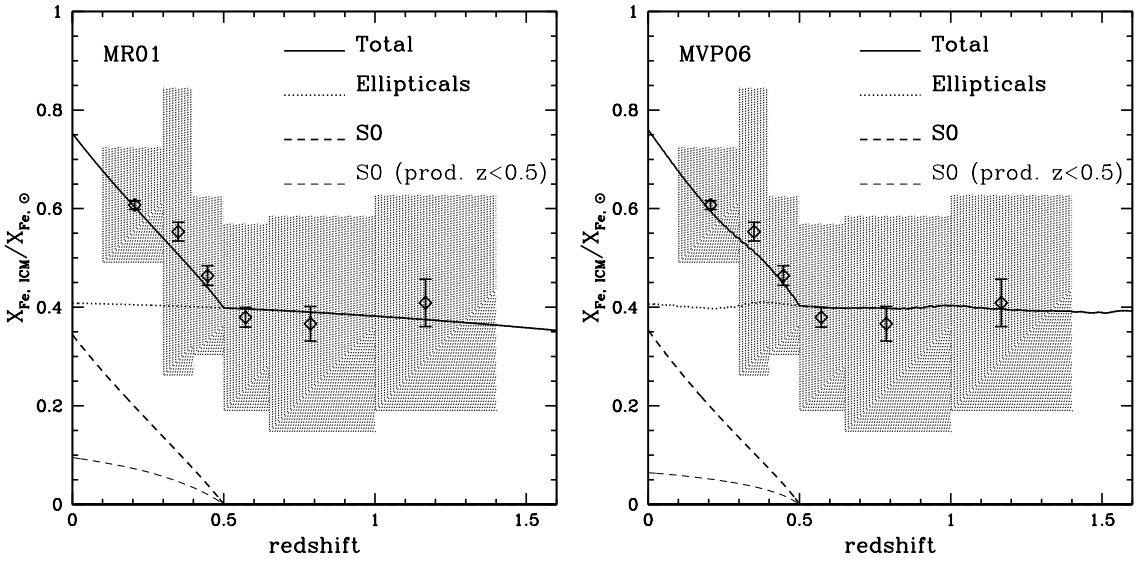

Figure 4.2: Observed and predicted redshift evolution of the Fe abundance in the ICM relative to solar. In both panels, the open diamonds with error bars and the shaded areas show the weighted means and the *rms* dispersion around the weighted means of the Fe abundances in the 6 redshift bins as observed by Balestra et al. (2007), respectively. The Fe abundances by Balestra et al. (2007) have been rescaled by a factor of 1.5, owing to the meteoritic value by Anders & Grevesse (1989). The thick dashed lines, dotted lines and the solid lines are the predicted contributions to the ICM Fe abundance given by S0 galaxies, ellipticals and the total ICM Fe abundance, respectively, calculated assuming for the SNIa rate the formulation by Matteucci & Recchi (2001) (*left panel*) and Mannucci et al. (2006) (*right panel*). The thin dashed lines represent the contribution due to the Fe produced in S0 at $z < 0.5$.

Chapter 5

Metal abundances in Active Galactic Nuclei

5.1 Introduction

The determination of chemical abundances in AGN provides a powerful tool to probe star forming activity in galactic nuclei both at present, and in the early Universe. Most of the studies of metal abundances of AGN in the literature are based on optical/UV observations. Early studies used weak and broad intercombination lines, such as N III] λ1750, N IV] λ1486, and O III] λ1663, to determine metal abundances in the broad-line region (BLR) gas (Shields 1976). These early studies found that BLR metallicity is typically solar, with some luminous quasars reaching super-solar values. Hamann & Ferland (1993) found that emission-line ratios, such as N V λ1240/C IV λ1549 can trace the BLR metallicity across a wide range of luminosities and BLR densities (see also Hamann et al. 2002 for a more detailed model). They also found that BLR metallicity, determined in this way, correlates with luminosity, in what they proposed as the metallicity–luminosity ($Z-L$) relationship in AGNs. Given the well known relationship between AGN luminosity and black hole mass ($M_{\rm BH}$), Hamann & Ferland (1993) suggested that the $Z-L$ relationship can naturally lead to a $Z-M_{\rm BH}$ dependence, in analogy with the mass–metallicity relation observed in some elliptical galaxies (e.g. Trager et al. 2000).

Narrow-line Seyfert 1 galaxies (NLS1), identified by the unusual narrowness of the broad component of their Hβ lines, are AGN that are believed to be powered by super-massive black holes of relatively small masses, with high accretion rates, possibly close to the Eddington limit[1] (e.g. Pounds et al. 1995; Boller et al. 1996). Furthermore, NLS1 have long been known to be characterized by extreme properties of their X-ray emission: a strong soft excess in the *ROSAT* soft band ($0.1-2.4$ keV, Boller et al. 1996), unusually steep X-ray spectra in the hard X-ray band ($2-10$ keV, Brandt et al. 1997; Leighly 1999b; Vaughan et al. 1999), very rapid and large variability (Leighly 1999a).

Shemmer & Netzer (2002) has shown that once NLS1 are introduced to the $Z-L$ diagram, they deviate significantly from the $Z-L$ relation by exhibiting high N V/C IV at low luminosity. A possible explanation is that N V/C IV is not an adequate metallicity indicator for NLS1 (and perhaps other AGN). Otherwise, this implies that at least at low-luminosity, the $Z-L$ relation is more complex and cannot be a simple two-parameter dependence. According to Shemmer & Netzer (2002), BLR metallicity also depends on the width of Hβ, which is perhaps the best accretion rate indicator (in terms of the Eddington ratio: $L_{\rm Bol}/L_{\rm Edd}$), and that this dependence may prevail also at the high-luminosity end.

More recently, Shemmer et al. (2004) used near infrared spectroscopic measurements of the Hβ region for a sample of AGN for which Hβ widths and rest-frame UV measurements of N V λ1240 and C IV λ1549 emission-lines were available, to calculate the N V/C IV emission line ratio, using it as a BLR metallicity indicator. N V/C IV is easier to measure than most other emission lines in a typical spectrum, and was considered by Hamann et al. (2002) as a robust indicator since it minimizes non-abundance effects, such as temperature, and spectral energy distribution. Fig. 5.1 shows the metallicity (N V/C IV) derived by

[1] We remind that the Eddington limit, or Eddington luminosity, represents the luminosity for which the radiation pressure counterbalances the force of gravity. It is defined as $L_{Edd} \equiv \frac{4\pi G c m_p}{\sigma_T} M$, where m_p is the proton mass and σ_T is the Thompson scattering cross section. It can be thought of as the maximum luminosity of a source of mass M that is powered by spherical accretion.

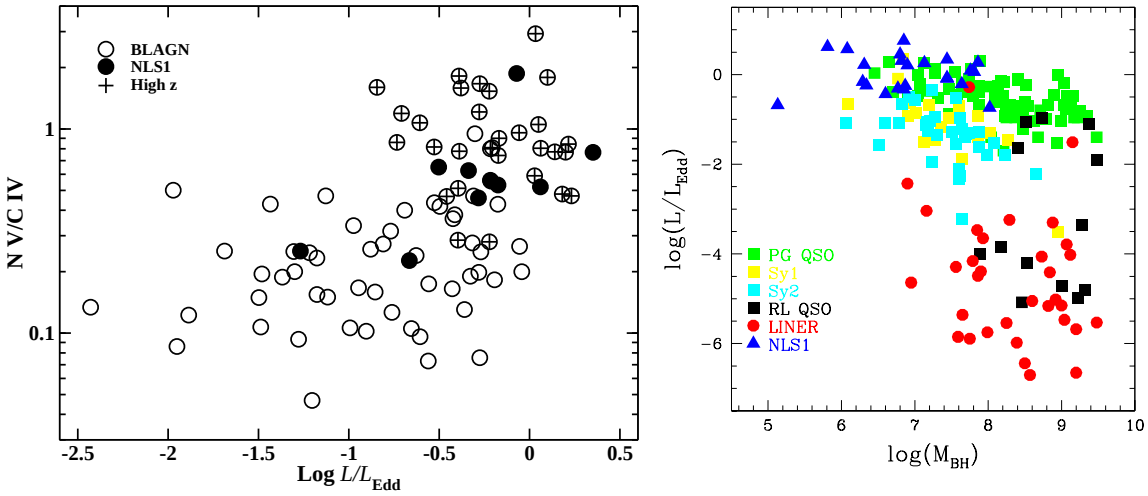

Figure 5.1: *(Left panel)* The metallicity indicator N V/C IV plotted versus the Eddington ratio for a sample of BLAGN, NLS1, and high-z quasars. A strong metallicity–accretion rate correlation is apparent, and most NLS1s are found in the same region of parameter space that is shared by the high-z quasars (see Shemmer et al. 2004). *(Right panel)* Eddington ratio plotted versus black hole mass for a sample of Sy1, Sy2, LINERs, NLS1s, Radio Loud and Radio Quiet Quasars (data from Satyapal et al. 2005; see references therein).

Shemmer et al. (2004) plotted against the Eddington ratio ($L/L_{\rm Edd}$), that is a measure of the accretion rate[2]. The AGN follow a metallicity–accretion rate correlation ($Z-L/L_{\rm Edd}$) with NLS1 being no exception.

In this work, we aim at obtaining estimates of the abundances of metals from X-ray data by means of high resolution X-ray spectroscopy. Under very general assumptions in modelling emission mechanisms (i.e. thermal emission or photoionization models) the fluxes of the most prominent emission lines can be used to infer the relative abundances of the metals responsible for those lines.

Soft X-ray spectra of AGN are expected to be affected by emission and scattering from a medium strongly influenced by the nuclear continuum. However, soft X-rays can also be produced through mechanical heating, as in shocks driven by supernova explosions in nuclear star-forming regions, or shocks created in or by outflowing material. It is also plausible that both effects are important. The spectra could contain a combination of separate components of warm plasma whose emission is predominantly "radiation-driven" (dominated by photoionization and photoexcitation) and hot plasma whose emission is predominantly "collision-driven" (dominated by electron-impact ionizations and excitations at a temperature consistent with the observed line energies). Since the same ionic transitions are expected in both types of plasma, the capability of distinguishing between different emission mechanisms is limited by the CCD spectral resolution and the S/N of the X-ray observations. Therefore, obtaining measurements of metal abundances from X-ray spectra is not an easy task. In the study of X-ray derived AGN metallicities, we are forced to restrict our analysis only to sources having high S/N spectra, either very X-ray bright objects or nearby obscured Seyfert galaxies (i.e. Mrk 3, Sako et al. 2000; NGC 1068, Kinkhabwala et al. 2002), where soft X-ray emission lines are more prominent due to the absorption of the nuclear continuum.

In this work we select the brightest NLS1 observed by XMM-*Newton* to infer their metallicities from the emission lines detected in their RGS spectra and then compare those to the typical metallicities measured in local AGN and distant quasars, in order to assess the trend of increasing metallicities with increasing accretion rates inferred from UV/optical/IR data.

[2]The Eddington ratio represents the accretion rate in units of Eddington luminosity $\frac{L_{bol}}{L_{Edd}} = \frac{\eta \dot{M} c^2}{L_{Edd}} = \dot{m}$.

5.2 Accretion rate versus black hole mass

The plot in Fig. 5.1 shows how the Eddington ratio, that is the ratio of the bolometric luminosity over the Eddington luminosity (L_{bol}/L_{Edd}) and a measure of the accretion rate, varies as a function of the black hole mass (M_{BH}) for a sample of Seyfert 1, Seyfert 2, LINER, NLS1, Radio Loud and Radio Quiet Quasars (see Satyapal et al. 2005 and references therein). This plot clearly shows that bolometric luminosities of NLS1 are typically close to the Eddington limit and the estimated mass of their central black holes are relatively small ($10^5 - 10^8\,M_{\odot}$).

On the other hand, typical accretion rates of LINER are much smaller ($L/L_{Edd} \simeq 10^{-4} - 10^{-5}$), while their nuclear black holes are more massive ($M_{BH} \simeq 10^7 - 10^9\,M_{\odot}$). Interestingly, one third to as many as one half of all galaxies in the local Universe are classified as LINER, displaying narrow optical emission lines of low ionization uncharacteristic of photoionization from normal stars (e.g. Heckman 1980; Ho et al. 1997; Stauffer 1982). Since normal galaxies are now known ubiquitously to host quiescent black holes (Gebhart et al. 2000; Ferrarese & Merritt 2000), the low mass accretion rates inferred for many confirmed accretion-powered LINER may suggest that these objects capture the population of AGN just before accretion onto the black hole "turns off".

A viable model of AGN evolution is that they start off by accreting mass at high rates, when fuel supply is abundant, and then gradually decrease their accretion rates as the fuel supply diminishes.

NLS1 seem to have typically higher metal abundances than AGN accreting mass at lower rates, like high-z AGN and quasars (Shemmer et al. 2004; Fig. 5.1). This suggests that the nuclear regions of these objects are already significantly enriched with metals and, therefore, must have experienced episodes of star formation in the past.

In this work, we aim at probing metallicities in NLS1, that are the class of AGN in the nearby Universe exhibiting the most extreme conditions of mass accretion (i.e. close to the Eddington limit) and that might be in an early stage of nuclear activity, somewhat analogous to the most distant quasars.

5.3 XMM-*Newton* NLS1 sample and data reduction

We considered all the known NLS1 that have been observed on-axis in the imaging mode with the EPIC-PN camera. The high-quality $2.5 - 10$ keV PN spectra of this sample of 28 NLS1, have been analyzed by Gallo (2006).

We selected the three brightest NLS1 (i.e. Mrk 110, Akn 564, and Mrk 335, having $2.5 - 10$ keV fluxes of 2.5, 1.9, and $1.2{\times}10^{-11}$ erg cm^{-2} s^{-1}, respectively) for our analysis in order to have the best possible S/N ratio to search for emission lines in the RGS spectra. For each observation we processed the RGS data starting from the *observation data files*, using SAS V7.0 and the most advanced calibration files available as of 2007 January. Background spectra were generated using blank field event lists, accumulated from different positions on the sky vault along the mission. Each spectrum was systematically searched for the presence of emission lines. We simultaneously fit the spectra of the two RGS cameras, using XSPEC version 11.3.1 (Arnaud 1996). *Local* fits[3] to the data were performed on the unbinned spectra on $\simeq$100 channels wide intervals, using Gaussian profiles to account for any line feature.

Local continua were modeled with power-laws, leaving the spectral index Γ and the continuum normalization free to vary in each fit. No assumption was made *a priori* on the line centroid energies. A line is considered to be detected when its flux is inconsistent with 0 at the 1σ confidence level.

Line luminosities have been corrected for Galactic photoelectric absorption using column densities after Dickey & Lockman (1990).

5.4 Results

In our analysis we only consider emission lines in the RGS spectra, since we aim at constructing a diagnostic for metal abundances that can be applied also to obscured objects, where absorption lines cannot be used. Fig. 5.2 shows the RGS smoothed spectra of the three NLS1 selected for the spectral analysis. From a visual inspection we notice that both the O VIII Ly-α and O VII He-α forbidden lines are present in all the spectra. In addition, several other transition from Ne IX, N VII and C VI are apparent. All the emission lines detected at more than 1σ c.l. for each source are listed in Table 5.1, 5.2, and 5.3. The

[3]By *local* fit we mean a fit that is performed over a small energy band around the emission line energy.

Table 5.1: Akn 564. Best-fit parameters for the emission lines discussed in this work.

Transition	λ_{lab} [ang]	E_{lab} [keV]	E_{obs} [keV]	flux [10^{-5} ph cm^{-2} s^{-1}]	EW [eV]
Ne X Ly-α	12.134	1.01986	–	–	–
Ne IX He-α (r)	13.447	0.92028	–	–	–
Ne IX He-α (i)	13.553	0.91328	–	–	–
Ne IX He-α (f)	13.699	0.90328	$0.9028^{+0.0025}_{-0.0024}$	$4.79^{+3.30}_{-3.40}$	1.020
O VII He-γ	17.768	0.69648	–	–	–
O VII He-β	18.616	0.66475	–	–	–
O VIII Ly-α	18.627	0.65240	$0.6616^{+0.0013}_{-0.0210}$	$5.69^{+4.34}_{-4.37}$	0.465
O VII He-α (r)	21.602	0.57290	–	–	–
O VII He-α (i)	21.803	0.56792	–	–	–
O VII He-α (f)	22.101	0.55993	$0.5593^{+0.0006}_{-0.0005}$	$22.8^{+12.9}_{-11.2}$	1.170
N VII Ly-α	24.782	0.49937	$0.4889^{+0.0220}_{-0.0010}$	$6.06^{+5.80}_{-5.70}$	0.220
N VI He-α (r)	28.787	0.42988	–	–	–
N VI He-α (i)	29.083	0.42551	$0.4266^{+0.0005}_{-0.0004}$	$16.3^{+8.3}_{-8.1}$	0.426
N VI He-α (f)	29.534	0.41901	–	–	–
C VI Ly-α	33.737	0.36682	–	–	–

Notes: '–' indicates either lines not detected, or lines for which no constraints can be obtained. The second and third columns list the laboratory wavelengths and energies, respectively. Errors refer to the 1σ confidence level.

uncertainties on the line fluxes are large: typically $\gtrsim 30\%$. In the case of Akn 564 the errors are too large to derive any meaningful result. Therefore, hereafter we will not further discuss the data of this source.

As already mentioned above, in the unified picture of AGN (Miller & Antonucci 1983; Antonucci & Miller 1985; Antonucci 1993), the soft X-ray spectrum is expected to be dominated by emission and scattering from a medium photoionized by the central continuum radiation. Many AGN, however, harbor regions of intense star formation where soft X-rays are produced through mechanical heating such as shocks generated in young supernova explosions and nuclear jets, which make interpretations in terms of both mechanically heated gas as well as radiatively heated gas physically plausible. When observed with the moderate spectral resolving power currently available, the mechanisms underlying the resulting spectra are, in most cases, also spectroscopically indistinguishable.

One way to distinguish between the two is to measure one of the standard diagnostic ratios $R = f/i$ and $G = (f + i)/r$ (Gabriel & Jordan 1969), where r, i, and f are the resonance, intercombination, and forbidden line fluxes, respectively.

Another way is to detect radiative recombination continua (RRC), which are produced when electrons recombine directly to the ground state of highly-ionized metals. RRC are broad features for hot, collisionally-ionized plasma, but are narrow, prominent features for cooler photoionized plasma.

Unfortunately, both the large uncertainties on the R and G ratios for O VII lines and the lack of a clear detection of RRC in any of the spectra, prevent us from using such diagnostic tools to distinguish between the two emission mechanisms. Therefore, in the following we discuss the results obtained from the spectral analysis of the RGS spectra of Mrk 110 and Mrk 335, under the assumption that the observed soft-X-ray emission lines are produced either by thermal excitation or by photoionization.

5.4.1 Collisionally ionized plasma

Diffuse, optically thin, thermal plasma may be present in star forming regions around the nuclei of galaxies. We try to model the emission lines detected in the RGS spectra of Mrk 110 and of Mrk 335 using a thermal emission model in order to estimate the metal abundances of the plasma. In this case, the abundance of an element can be measured directly from the equivalent width of its corresponding emission line, under the reasonable assumption of collisional equilibrium (see Appendix). Therefore, the shape of the continuum, which depends on the temperature of the plasma, must be modelled together with the emission lines.

We model the continuum of the RGS spectra of Mrk 110 using the best-fit obtained from the analysis of the PN data (see Boller et al. 2007). This model consists of two absorbed power laws with spectral index

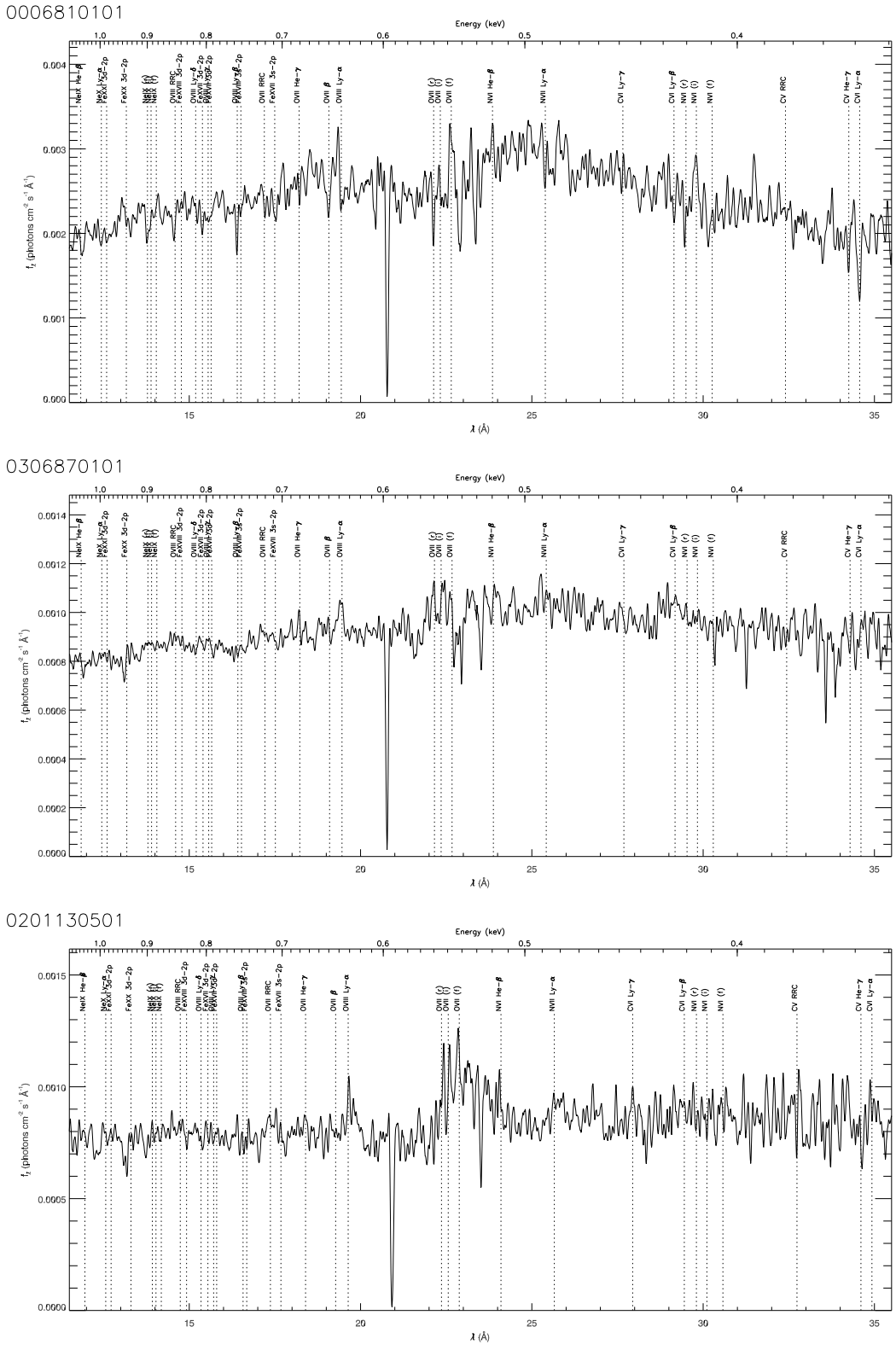

Figure 5.2: RGS spectra for the three galaxies of our sample (*upper panel:* Akn 564; *middle panel:* Mrk 335; *lower panel:* Mrk 110). The spectra of the two RGS cameras have been merged and smoothed with a 5-channels wide triangular kernel for illustration purposes only. The laboratory energies (at the source rest-frame) of the line transitions are labeled.

Table 5.2: Mrk 335. Best-fit parameters for the emission lines discussed in this work.

Transition	λ_{lab} [ang]	E_{lab} [keV]	E_{obs} [keV]	flux [10^{-5} ph cm^{-2} s^{-1}]	EW [eV]
Ne X Ly-α	12.134	1.01986	–	–	–
Ne IX He-α (r)	13.447	0.92028	–	–	–
Ne IX He-α (i)	13.553	0.91328	–	–	–
Ne IX He-α (f)	13.699	0.90328	–	–	–
O VII He-γ	17.768	0.69648	–	–	–
O VII He-β	18.616	0.66475	–	–	–
O VIII Ly-α	18.627	0.65240	$0.6554^{+0.0005}_{-0.0010}$	$2.75^{+0.97}_{-0.95}$	0.727
O VII He-α (r)	21.602	0.57290	$0.5743^{+0.0006}_{-0.0003}$	$4.18^{+1.62}_{-1.55}$	0.745
O VII He-α (i)	21.803	0.56792	$0.5666^{+0.0019}_{-0.0007}$	$4.87^{+1.69}_{-1.69}$	0.845
O VII He-α (f)	22.101	0.55993	$0.5475^{+0.0008}_{-0.0009}$	$4.12^{+1.70}_{-1.63}$	0.662
N VII Ly-α	24.782	0.49937	$0.5033^{+0.0005}_{-0.0003}$	$2.43^{+1.25}_{-1.03}$	0.330
N VI He-α (r)	28.787	0.42988	$0.4356^{+0.0007}_{-0.0006}$	$2.46^{+1.66}_{-1.61}$	0.233
N VI He-α (i)	29.083	0.42551	–	–	–
N VI He-α (f)	29.534	0.41901	–	–	–
C VI Ly-α	33.737	0.36682	$0.3667^{+0.0008}_{-0.0004}$	$3.81^{+2.50}_{-2.43}$	0.231

Notes: '–' indicates either lines not detected, or lines for which no constraints can be obtained. The second and third columns list the laboratory wavelengths and energies, respectively. Errors refer to the 1σ confidence level.

Table 5.3: Mrk 110. Best-fit parameters for the emission lines discussed in this work.

Transition	λ_{lab} [ang]	E_{lab} [keV]	E_{obs} [keV]	flux [10^{-5} ph cm^{-2} s^{-1}]	EW [eV]
Ne X Ly-α	12.134	1.01986	–	–	–
Ne IX He-α (r)	13.447	0.92028	–	–	–
Ne IX He-α (i)	13.553	0.91328	–	–	–
Ne IX He-α (f)	13.699	0.90328	$0.9028^{+0.0025}_{-0.0024}$	$4.79^{+3.30}_{-3.40}$	1.020
O VII He-γ	17.768	0.69648	$0.6981^{+0.0022}_{-0.0019}$	$1.49^{+1.29}_{-1.18}$	0.604
O VII He-β	18.616	0.66475	–	–	–
O VIII Ly-α	18.627	0.65240	$0.6531^{+0.0006}_{-0.0008}$	$3.79^{+1.39}_{-1.35}$	1.330
O VII He-α (r)	21.602	0.57290	$0.5725^{+0.0004}_{-0.0006}$	$4.16^{+2.23}_{-2.08}$	0.956
O VII He-α (i)	21.803	0.56792	$0.5680^{+0.0003}_{-0.0006}$	$4.66^{+2.33}_{-2.17}$	1.040
O VII He-α (f)	22.101	0.55993	$0.5619^{+0.0005}_{-0.0006}$	$6.97^{+3.38}_{-2.95}$	1.490
N VII Ly-α	24.782	0.49937	$0.5008^{+0.0007}_{-0.0055}$	$1.94^{+1.58}_{-1.36}$	0.367
N VI He-α (r)	28.787	0.42988	–	–	–
N VI He-α (i)	29.083	0.42551	–	–	–
N VI He-α (f)	29.534	0.41901	–	–	–
C VI Ly-α	33.737	0.36682	$0.3570^{+0.0004}_{-0.0003}$	$4.35^{+3.34}_{-2.94}$	0.395

Notes: '–' indicates either lines not detected, or lines for which no constraints can be obtained. The second and third columns list the laboratory wavelengths and energies, respectively. Errors refer to the 1σ confidence level.

Table 5.4: Results from the VMEKAL and VAPEC model fits for the RGS spectra of Mrk 110.

Parameter	POWER LAW	POWER LAW
Γ_1	2.5*	2.5*
	POWER LAW	POWER LAW
Γ_2	1.4*	1.4*
	VMEKAL	VAPEC
kT	0.72*	0.72*
C	$1.4^{+0.8}_{-0.7}$	$0.57^{+0.49}_{-0.35}$
N	$1.1^{+0.7}_{-0.6}$	$1.12^{+0.59}_{-0.43}$
O	$0.17^{+0.05}_{-0.04}$	$0.12^{+0.04}_{-0.03}$
Ne	< 0.05	< 0.03
Si	< 2.6	< 1.6
Fe	< 0.2	< 0.1

Notes: * denotes a fixed parameter. Errors refer to the 1σ confidence level. Metal abundances are in solar units following Anders & Grevesse (1989).

fixed to $\Gamma_1 = 2.4$ and $\Gamma_2 = 1.4$ plus a thermal component, having a temperature fixed to $kT = 0.7$ keV (if Γ_1, Γ_2, and kT are left free to vary we find consistent fit results), that we model here with a VMEKAL (or VAPEC) to let the relative abundance of elements free to vary. We fix the Galactic photoelectric absorption to the column density after Dickey & Lockman (1990). The results of the fits are listed in Table 5.4. We find that the abundances of C and N are consistent with solar values, while O is $\sim 1/5$ solar. We can only derive upper limits on Ne, Si, and Fe abundances. However, the Fe abundance inferred here is based only on the weaker L-shell transitions. More precise Fe abundance measurements can be obtained from the PN spectrum, where the K-shell transition at 6.4 keV is detected (see Boller et al. 2007).

We follow the same approach for the spectral analysis of Mrk 335: we use the best-fit model obtained from the analysis of the PN data (see Gondoin et al. 2002). This model consists of a single absorbed power law with spectral index fixed to $\Gamma = 2.5$ plus a thermal component, having a temperature fixed to $kT = 0.27$ keV. We model again the thermal component with a VMEKAL (or VAPEC) and we fix the Galactic absorption following Dickey & Lockman (1990). Unfortunately, we cannot find meaningful constraints on the metal abundances from the spectral fits for this source, probably due to the difficulties in fitting the continuum with the model from Gondoin et al. (2002), which also refers to different calibrations. A more detailed spectral analysis is required in this case. We defer this to a future work.

5.4.2 Photoionized gas

Here, we test the hypothesis that the observed soft-X-ray emission lines are produced by photoionization of a gas surrounding the active nucleus. In this case, the emission from the plasma is predominantly driven by the primary nuclear radiation illuminating it and, therefore, is dominated by photoionization and photoexcitation, with the collisional excitations giving a negligible contribution to the flux of the soft-X-ray emission lines. Therefore, soft-X-ray emission lines ratios provide a temperature-independent diagnostic for metallicities in photoionized gas.

We use the numerical code CLOUDY, version 07.02 (Ferland et al. 1998) to predict emission line ratios for different plasma conditions. We assume a simple plane-parallel geometry for the photoionized gas, which is equivalent to assume that the gas is far enough from the illuminating source so that its own thickness can be neglected. We assume a constant gas density $n_H = 10^5$ cm^{-3} and we model the shape of the incident spectrum with a power law of spectral index $\Gamma = 1.7$. Under these assumptions the emission line ratios still depend on the ionization parameter ($U \equiv f_H/n_H c$, where f_H is the flux of ionizing photons), the absorbing column density toward the observer (N_H), and the metal abundances. In order to evaluate the effect of the metallicities on the emission line ratios for different plasma conditions, we calculate f_{OVII}/f_{OVIII}, f_{NeIX}/f_{OVIII}, f_{NVII}/f_{OVIII}, and f_{CVI}/f_{OVIII} for a grid of U and N_H values (see Fig. 5.3 and 5.4). Using our constraints on these line ratios (see Table 5.4.2), we can define regions of the parameter space that are "permitted" for a given elemental abundance. For example, in the upper panels of Fig. 5.3 and Fig. 5.4 all the abundances are fixed to solar. While the lower panels of Fig. 5.3 and Fig. 5.4 show the same plots in which we double the abundance of Ne for Mrk 110 and N for Mrk 335,

Table 5.5: Ratios of emission lines fluxes from Table 5.4 and 5.4.

Flux ratio	Mrk 110	Mrk 335
$f_{O\,VII}/f_{O\,VIII}$	1.58 ± 0.92	1.29 ± 0.69
$f_{Ne\,IX}/f_{O\,VIII}$	1.75 ± 0.77	–
$f_{N\,VII}/f_{O\,VIII}$	0.39 ± 0.33	0.68 ± 0.40
$f_{C\,VI}/f_{O\,VIII}$	0.65 ± 0.53	0.78 ± 0.58

Notes: Flux ratios are computed for line fluxes in units of erg cm^{-2} s^{-1}. Errors refer to the 1σ confidence level.

respectively.

Despite the large uncertainties, these diagrams can be used as a diagnostic for metallicities. We find that, in the case of Mrk 110, a twice solar abundance of Ne allows for a much larger intersection with the O constraints in the $U - N_H$ parameter space. This indicates either that Ne/O is overabundant in this source or that these elements must originate from different phases of the gas (i.e. differently ionized regions, that is different values of U). However, as it can be seen from Fig. 5.5, Ne and O emission line fluxes peak approximately at the same value of the ionization parameter ($U \simeq 1.4 - 1.5$) for a fixed value of N_H. This seems to point toward a Ne overabundance. For N/O and C/O we find no evidence for a deviation from solar ratios.

In the case of Mrk 335, we find that a larger region of the parameter space explored is allowed, when N/O is fixed to twice solar, which is again indicating either that these elements originate from different phases of the gas or that N must be overabundant. From Fig. 5.5, we notice that the differences in the flux of the N emission line are small between $U = 1.5$ and 2.5, which seems to favour N overabundance. Finally, for C/O we find no evidence for a deviation from solar ratios.

5.5 Discussion

In the case of thermal origin of the soft-X-ray emission lines detected the two NLS1 analyzed here, we are not able to characterize the metallicities, due to the difficulties in constraining the continuum emission. At present we cannot rule out the hypothesis that the observed line fluxes are entirely, or partially, due to some hot gas in star forming regions around the nucleus. However, the photoionization model presented here, which is analogous to the one routinely used in the optical/UV studies for the determination of the BLR metallicities, gives indications for solar or twice solar abundances in both objects analyzed, in agreement with the optical/UV studies of NLS1. A further evidence for oversolar abundances of Fe in NLS1 comes from studies of bright unobscured AGN exhibiting broad relativistic profiles of the Fe lines (see Fabian & Miniutti 2005 and references therein). Furthermore, the soft-X-ray emission produced by photoionization of the gas surrounding the nuclei of obscured AGN has been found to coincide in extension and overall morphology with the optical O III] emission (Bianchi et al. 2006).

It is worth noticing that the NLS1 considered in this work have different values of the Eddington ratios and black hole mass: Mrk 110 has $L/L_{\rm Edd} = 0.01$ and $M_{BH} = 1.4 \times 10^8\,M_\odot$, while Mrk 335 has $L/L_{\rm Edd} = 1.6$ and $M_{BH} = 7.9 \times 10^6\,M_\odot$. Given the $Z - L/L_{\rm Edd}$ dependence claimed by Shemmer et al. (2004), we would expect to measure different metallicities in these two NLS1. However, the present data allows us to find only indications for solar or twice solar abundances in both sources when using photoionization model for the production of the soft-X-ray emission lines. Therefore, in order to probe the metallicities as a function of the accretion rate or the black hole mass we need to study a sample of AGN covering a wide range of $L/L_{\rm Edd}$ and M_{BH}. A sample of absorbed AGN, i.e. bright nearby Seyfert 2, could be appropriate to this aim.

The diagnostic diagrams used in Sect. 5.4.2 can be successfully applied to other bright AGN, in particular obscured ones (i.e. Seyfert 2), where soft-X-ray line fluxes and ratios can be derived with higher accuracy. For instance, we tried to apply the same analysis to the Seyfert 2, NGC 1068, with line ratios following Kinkhabwala et al. (2002). We obtain indications for overabundance of N in this source, in agreement with previous results by Kinkhabwala et al. (2002).

Solar or a few times solar abundances are observed in samples of quasars at high redshift. This supports the idea that both quasars and NLS1 must have experienced an intense star formation activity followed by the release of metals in the inter-galactic medium. As already mentioned in Sect. 5.2, a viable model of AGN evolution is that they start off with high accretion rates, when fuel supply is abundant, and gradually

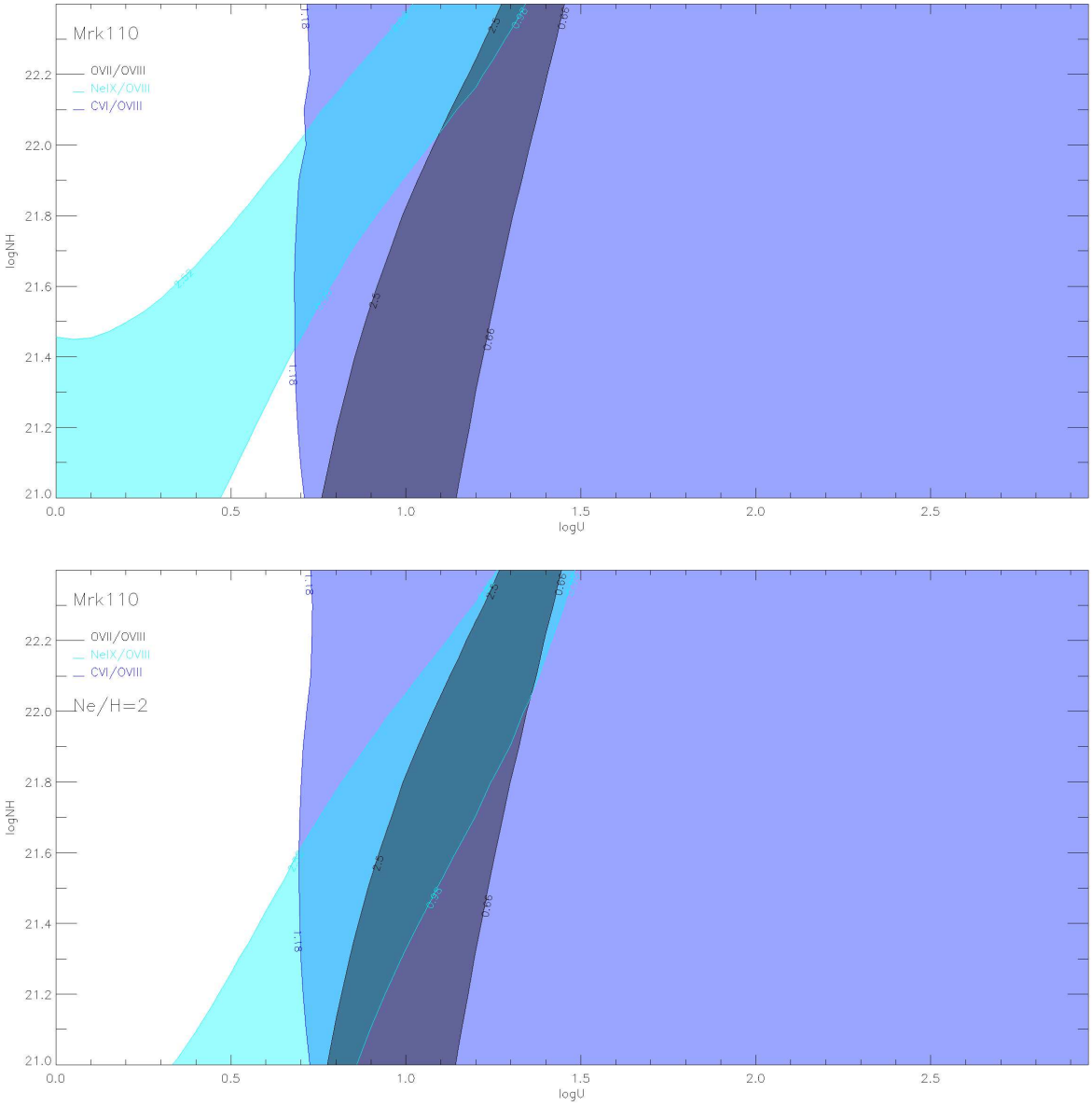

Figure 5.3: Mrk 110: the two diagrams show how the constraints on O VII/O VIII, Ne IX/O VIII, N VII/O VIII, and C VI/O VIII vary as a function of the absorbing column density N_H and the ionization parameter $U \equiv f_H/n_H c$. The model calculations are performed using `CLOUDY`, where we set a spectral index $\Gamma = 1.7$ for the input spectrum, a constant gas density $n_H = 10^5$ cm^{-3}, and solar metal abundances (*upper panel*) and for a twice solar abundance of Ne (*lower panel*). Lines are the 1σ confidence levels from our measurements.

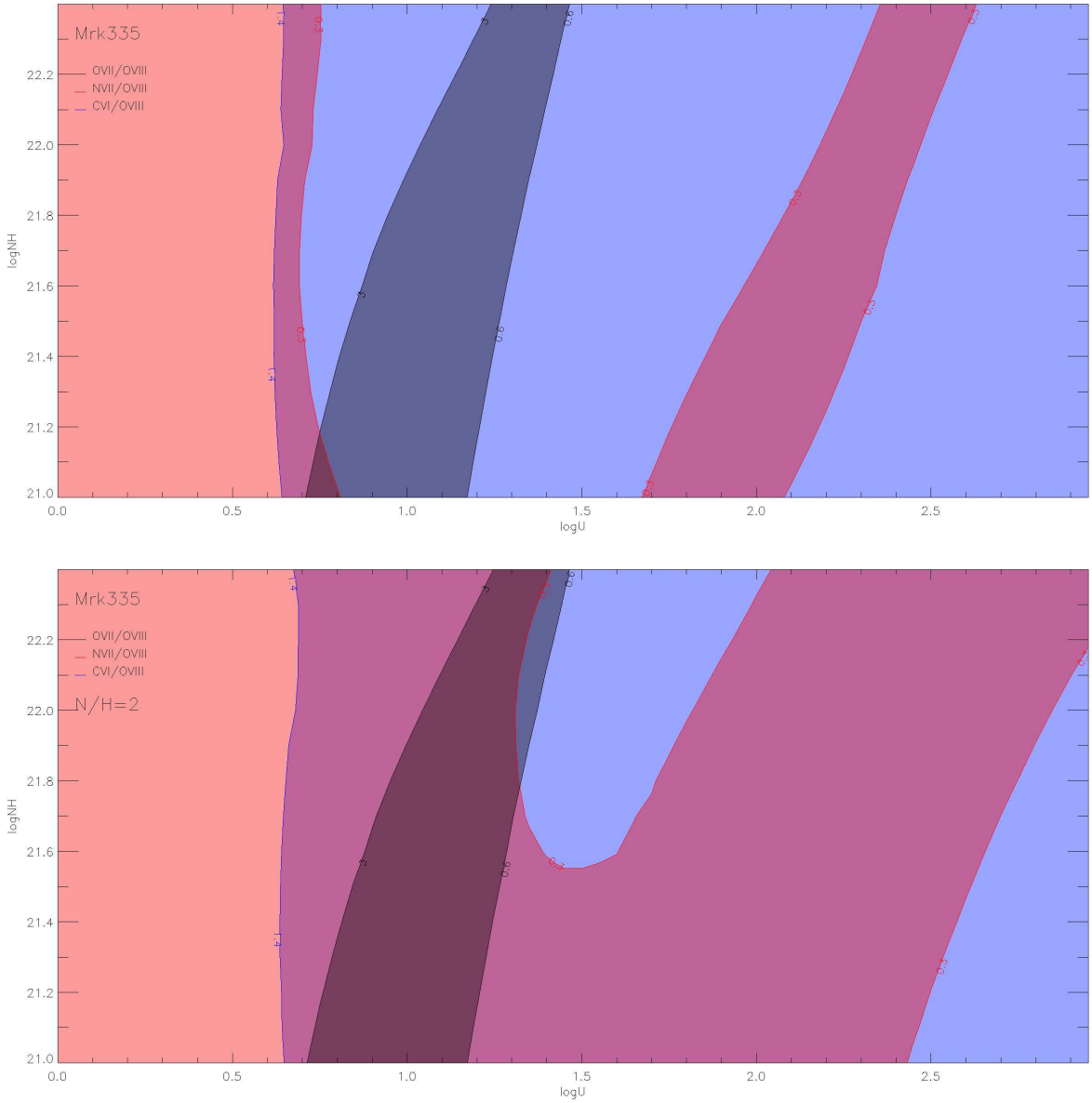

Figure 5.4: Mrk 335: same as Fig. 5.3 but for a twice solar abundance of N (*lower panel*).

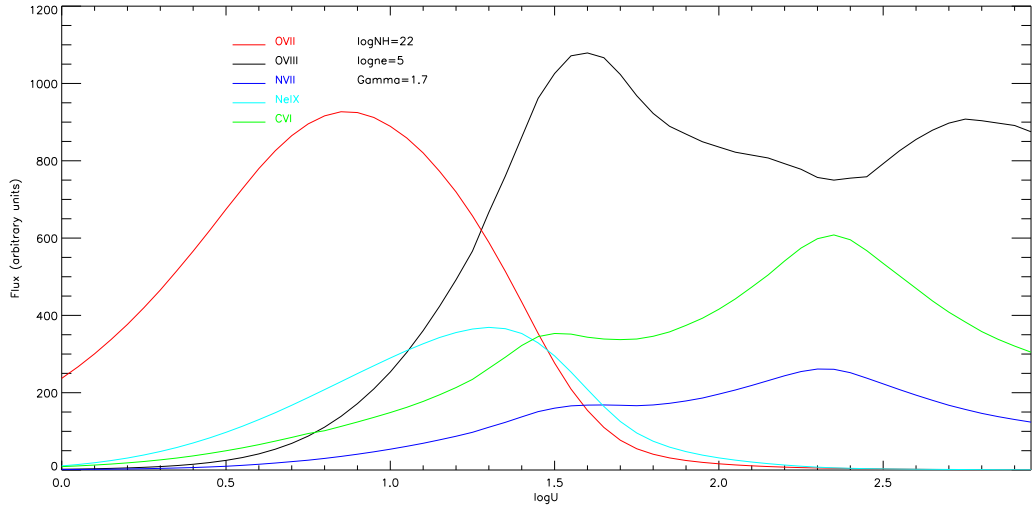

Figure 5.5: Flux of the five emission lines of interest as a function of the ionization parameter U. The model calculation refers to a photoionized gas with $log\, N_H = 22$, $log\, n_H = 5$, and $\Gamma = 1.7$. O VIII and Ne IX line fluxes peak at about the same ionization parameter $U \simeq 1.4 - 1.5$, while the flux of N VII is relatively flat between $U \simeq 1.5$ and 2.5.

move towards lower accretion rates as the fuel supply dwindles. If the metal content of the gas does not change as a consequence of the fuel shortage, one can expect an AGN to move horizontally, from right to left, across the $Z - L/L_{\rm Edd}$ diagram (Fig. 5.1), as a function of time. In other words, similar metallicities may be observed for a range of accretion rates. The dependence on age may be further complicated by the AGN duty cycle (assumed to be $\sim 10^7 - 10^8$ yr), as we do not know the number of cycles each AGN has gone through. If metal enrichment is strongly related to AGN fueling, then a number of active episodes may contribute to metal enrichment provided the metal rich gas is not being depleted or blown out of the nucleus. This can lead to a $Z - L/L_{\rm Edd}$ dependence which is more complicated than assumed here.

The $Z - L/L_{\rm Edd}$ correlation may have important implications for the understanding of black-hole growth in galactic nuclei as well as for the starburst-AGN connection. We find that NLS1s in the nearby Universe, like the luminous quasars at high-redshift, may be experiencing (or have recently experienced) a vigorous star-forming episode, and their black holes are in the stage of rapid growth. In this sense, the NLS1 may be in the early stages of their (current) activity, i.e., relatively "young" systems, as suggested by Mathur (2000). To this respect, studies of metal abundances based on X-ray data are a valuable tool to probe independently the claims for a $Z - L/L_{\rm Edd}$ correlation.

5.6 Conclusions

We analyzed the high resolution X-ray spectrum of three bright NLS1 (i.e. Mrk 110, Mrk 335, and Akn 564), to derive the abundances of several metals (i.e. C, N, O, Ne, Fe). The uncertainties on the fluxes of the emission lines in the spectra allow to derive estimates of the metal abundances only in two of the sources (i.e. Mrk 110 and Mrk 335). We found that:

- in the case that the observed emission lines originate by thermal excitation in a collisionally ionized plasma, which could be associated to star forming regions around the nucleus of the galaxy, the abundance of C and N are close to solar and O is $\sim 1/5$ solar in Mrk 110, while for Mrk 335 we cannot find meaningful constraints on the metal abundances;

- if, instead, the emission lines are produced by photoionization of a gas surrounding the nucleus of the galaxy, the observed line ratios are reproduced if, under reasonable assumptions (i.e. simple geometry of the gas, a density of the gas $n_H = 10^5$ cm^{-3}) the ratios of the abundances of metals are solar, for a wide range of absorbing column densities N_H and a reasonably narrow range of ionization

parameters U. The only exception being the Ne/O for Mrk 110 and N/O for Mrk 335, which seems to point toward a Ne and N overabundance, respectively.

Metal abundances of AGN may be derived from high-resolution X-ray spectroscopy and may be studied as a function of the accretion rate, by applying the analysis technique presented in this work to a sample of bright obscured AGN, where the fluxes of the emission lines are measured with smaller uncertainties. This will be subject of a future work.

Chapter 6

Summary and conclusions

We exploited the different capabilities of two of the currently operating X-ray telescopes (*Chandra*'s superior spatial resolution and the higher throughput of XMM-*Newton*) for the study of elemental abundances of the two most powerful X-ray emitters in the Universe: the hot intra-cluster medium, permeating clusters of galaxies, and active galactic nuclei. In the following we summarize the main results of the thesis.

Summary

In the first part, dedicated to the study of the chemical enrichment of the ICM, we presented the combined spectral analysis of 56 clusters of galaxies at intermediate-to-high redshifts observed by *Chandra* and XMM-*Newton* (see Balestra et al. 2007). Furthermore, we presented the XMM-*Newton* spectral analysis of 17 clusters of galaxies of the same sample, which were observed by both *Chandra* and XMM-*Newton*. The main results can be summarized as follows:

- We determine the average ICM iron abundance with a $\sim 20\%$ uncertainty at $z > 1$ ($Z_{Fe} = 0.27 \pm 0.05\, Z_{\odot}$), thus confirming the presence of a significant amount of iron in high-redshift clusters. Z_{Fe} is constant above $z \simeq 0.5$, the largest variations being measured at lower redshifts.

- We find a significantly higher average iron abundance in clusters with $kT < 5$ keV, in agreement with trends measured in local samples. For $kT > 3$ keV, Z_{Fe} scales with temperature as $Z_{Fe}(T) \simeq 0.88\, T^{-0.47}$.

- We find significant evidence of a decrease in Z_{Fe} as a function of redshift, which can be parameterized by a power law $\langle Z_{Fe} \rangle \simeq Z_{Fe}(0)\,(1+z)^{-\alpha_z}$, with $Z_{Fe}(0) \simeq 0.54 \pm 0.04$ and $\alpha_z \simeq 1.25 \pm 0.15$. This implies an evolution of more than a factor of 2 from $z = 0.4$ to $z = 1.3$.

- We measure the average ICM abundance of iron ($Z_{Fe} = 0.29 \pm 0.02\, Z_{\odot}$), nickel ($Z_{Ni} = 0.46 \pm 0.25\, Z_{\odot}$), oxygen ($Z_O = 0.23 \pm 0.15\, Z_{\odot}$), silicon ($Z_{Si} = 0.16 \pm 0.14\, Z_{\odot}$), and sulphur ($Z_S = 0.12^{+0.14}_{-0.12}\, Z_{\odot}$) at $0.3 < z < 0.5$. These are the first measurements of abundances of elements other than Fe in the ICM at high redshift. From the ratios of O/Fe, Si/Fe, S/Fe, and Ni/Fe we infer that the fraction of supernovae type Ia at $0.3 < z < 0.5$ must be larger than 80%, which is in agreement with several evidences indicating that the dominant contribution to the metal enrichment of the central regions of the ICM is from SNIa.

Precise measurements of the metal content of clusters over large look-back times provide a useful fossil record for the past star formation history of cluster baryons. A significant iron abundance in the ICM up to $z \simeq 1.2$ is consistent with a peak in star formation for proto-cluster regions occurring at redshift $z \simeq 4-5$. On the other hand, a positive evolution of Z_{Fe} with cosmic time in the last 5 Gyrs is expected on the basis of the observed cosmic star formation rate for a set of chemical enrichment models. Our data provide further constraints on the chemical evolution of cosmic baryons in the hot diffuse and cold phases.

In the second part, dedicated to the study of the metallicity of AGN, we analyzed the high resolution X-ray spectra of two bright NLS1 (i.e. Mrk 110 and Mrk 335), to derive the abundances of several metals (i.e. C, N, O, Ne, Fe). The main results can be summarized as follows:

- for soft-X-ray emission lines produced by thermal excitation in a collisionally ionized plasma, which could be associated to star forming regions around the nucleus of the galaxy, Mrk 110 has C and N abundances close to solar and O $\sim 1/5$ solar, while in the case of Mrk 335, we cannot find meaningful constraints on the metal abundances.

- if the soft-X-ray emission lines are produced by photoionization of a gas surrounding the nucleus of the galaxy, the observed line ratios are reproduced if, under reasonable assumptions (i.e. simple geometry of the gas, a density of the gas $n_H = 10^5$ cm^{-3}) the ratios of the abundances of metals are solar, for a wide range of absorbing column densities N_H and a reasonably narrow range of ionization parameters U. The only exception being the Ne/O for Mrk 110 and N/O for Mrk 335, which seems to point toward a Ne and N overabundance, respectively.

The metallicity–accretion rate correlation may have important implications for the understanding of black-hole growth in galactic nuclei as well as for the starburst-AGN connection. We find that NLS1s in the nearby Universe, like the luminous quasars at high-redshift, may be experiencing (or have recently experienced) a vigorous star-forming episode, and their black holes are in the stage of rapid growth. In this sense, the NLS1 may be in the early stages of their (current) activity, i.e., relatively "young" systems, as suggested by Mathur (2000).

The X-ray emission from the two classes of objects considered in this thesis is produced by different physical mechanisms. One must bear this in mind when comparing metal abundance estimates obtained for the ICM and for AGN. The cluster/field dichotomy, therefore, must be taken into account when comparing metal abundance measurements of the ICM and AGN and prevent us from drawing conclusions about the chemical enrichment of the universe as a whole. In fact, for instance, the morphological mix, luminosity function, and star formation history of cluster galaxies are distinct from those of their counterparts in the field, displaying signatures of the effect of the exceptionally dense environments where they form and develop (Kuntschner et al. 2002; Croton et al. 2005; Schindler et al. 2005; Romeo et al. 2005; Steidel et al. 2005).

Another issue of particular relevance in the context of tracing the cosmic evolution of metallicity in these two strong X-ray emitters is their different evolutionary scheme. While clusters of galaxies are formed through subsequent merger of smaller structures following a so called "hierarchical" pattern of structure formation, AGN seem to evolve following an opposite scheme ("anti-hierarchical" pattern), with the more luminous and more massive objects being more numerous at higher redshift (e.g. Ueda et al. 2003; Hasinger et al. 2005).

On one hand, through our study of metal abundances of the intra-cluster medium we were able to retrace the evolution of the iron content of metals with cosmic time inside the hot gas trapped into the deepest gravitational potential wells in the Universe. Our estimates of iron abundance in the ICM as a function of cosmic time provide constraints on the star formation in the cluster galaxies. We have shown how the iron content of the ICM, computed through models of chemical enrichment following different prescriptions for the star formation history in cluster galaxies (i.e. SNIa rates), can be compared to the observation in order to infer, for example, different delay times in the explosions of SNIa, different populations for the progenitors of SNIa, or morphological evolution of the cluster galaxies, with normal spirals converting into S0 after losing their gas.

Interestingly, we found that the iron abundance of the ICM is correlated to its temperature also at high redshift. The observed trend of declining iron abundances with increasing temperature is present at all redshift and even within different regions of the ICM itself. It is, therefore, tentative to conclude that this may be some universal property of the ICM, which, however, still needs to be explained.

On the other hand, metal abundances of quasar and high-redshift AGN also provide information on the chemical history of the gas and, therefore, on the epoch and extent of the star formation near the nuclei of their hosting galaxies. Our study of metal abundances in AGN is focussed on a particular class of objects in the local Universe, i.e. Narrow-Line Seyfert 1 galaxies (NLS1), which are believed to be accreting matter at high rates (close to the Eddington limit) onto super massive black holes of relatively small masses. On the basis of the evidence for a correlation between metallicity and accretion rate, inferred from UV/optical/IR spectroscopy, NLS1 are believed to have higher metallicities, probably due to the presence of regions of enhanced star formation. In the nuclear regions of high-redshift quasars, metals might come from some of the first stars forming in galactic or protogalactic nuclei after the Big Bang. The constraints on star formation and chemical evolution near quasars and AGN are a valuable complement to other studies that use different diagnostics, or probe larger galactic structures, such as Lyman-break

galaxies and damped Lyman-alpha systems (e.g. Lu et al. 1996; Pettini et al. 1997; Steidel et al. 1999; Prochaska et al. 2001 and references therein) or gamma-ray bursts (e.g. Savaglio 2006).

Acknowledgments

I am deeply indebted to Paolo Tozzi and Stefano Bianchi for their invaluable help in the completion of this work. I also thank Günther Hasinger for his support and open-mindedness through the three years of my PhD and I am extremely grateful to all my collaborators and scientists who enriched me with fruitful and enlightening discussions: J. Blaizot, T. Boller, S. Borgani, H. Böhringer, H. Brunner, M. Brusa, V. Burwitz, N. Cappelluti, A. Comastri, E. Costantini, G. De Lucia, S. Ettori, L. Gallo, K. Iwasawa, W. Kollatschny, D. Lutz, V. Mainieri, G. Matt, F. Matteucci, A. Merloni, C. Norman, G. Pratt, A. Renzini, P. Rosati, J. Santos, E. M. Rossi, N. Werner, Y.-Y. Zhang. I acknowledge financial support from the Max-Planck Institut and fundings from the Marie-Curie early stage training through the IMPRS school.

Appendix A

X-ray emission from collisional plasmas

Ionized plasmas produce copious amounts of X-rays. The emission of X-rays has two important consequences. First, it allows us to observe the plasma by detecting those X-rays and, in the case of an optically thin gas, since most of those X-rays do not interact between their emission and their detection in X-ray telescopes, this allows us to study their emission in an unperturbed state. Through X-ray spectroscopy and imaging, we can measure several physical quantities, such as the temperature and density of the plasma at various positions. The second important consequence for an optically thin plasma is that the emission of X-rays will tend to cool it. In the case of clusters of galaxies a significant quantity of energy is carried away by the X-rays as they escape the cluster. In the hot ICM the emission of X-rays was thought to set up a non-linear process of excessive cooling in the cores that was broadly termed a "cooling flow", however, after the lack of detection of the lowest X-ray temperatures expected from cooling flow models (Peterson et al. 2003), the central cooler regions of the ICM are now more generally referred to as "cool cores". In the following, we describe the process of X-ray emission from collisionally-ionized plasmas and show how it relates to the case of ICM (see Peterson & Fabian 2006 for a review).

The intra-cluster medium (ICM) is a plasma that is nearly fully ionized due to the high temperatures created by the deep dark matter gravitational potential. Hydrogen and helium, for example, are fully stripped of their electrons. Heavier elements have retained only a few of their electrons in this hot medium. In addition to free electrons and ions in the plasma, electromagnetic radiation, which is emitted mostly as X-rays, is created by quantum mechanical interactions in the plasma. The radiation emission processes are governed by equations for X-ray emission from a collisionally-ionized plasma.

A.1 Coronal approximation

The emission of X-rays from ionized atoms in a plasma can be quite complex. Fortunately, we can make use of several approximations to simplify the emission processes. The emission of X-rays in the ICM is well-described by the coronal approximation (Elwert & Naturf 1952; Mewe 1999). These approximations describe optically thin plasmas in collisional equilibrium. Collisional equilibrium occurs when electron collisional ionization processes are balanced precisely by recombination processes. The coronal approximation, as the name implies, was originally developed for studies of the Solar Corona, but the condition also applies to gas in clusters of galaxies, as well as hot gas in elliptical, starburst galaxies, and older supernovae remnants. In this approximation, there are three important conditions that specify the thermodynamical state of the free electrons, ions, and photons in the plasma, as well as the electron distribution within each ion.

The first approximation is that the photons are assumed to be free and do not interact with either the electrons or the ions after they are created. This has the importance consequence that photo-ionization processes (ionizing atoms by photons) and photo-excitation processes (raising an electron in an atom to an excited level) are far less frequent than electron collisional ionization and excitation processes. The radiation densities are low enough in clusters of galaxies for this condition to be met, except possibly for resonant scattering in some strong emission lines with high oscillator strength (Gilfanov et al. 1987).

The second approximation is that the atoms can be treated as if their electrons are all in their ground

state rather than having a Boltzmann distribution as is common in LTE (local thermodynamic equilibrium) gases. This is true if there is a low enough electron and radiation density, so that the excitations that are density dependent are less frequent than the radiative decays, which are quite fast for X-ray energies. The radiation density is low as discussed above. This condition is also met for electron densities below 10^{10} cm^{-3} for even slowly decaying metastable states. Densities in clusters are at most 10^{-1} cm^{-3}.

The final approximation is that the plasma is locally relaxed to a Maxwellian distribution around a common electron temperature, T. The free electrons and ions are assumed to have obtained a common temperature. This is only valid if typical dynamical time-scales, such as the time it takes the plasma to cool, is much longer than the time scale for sharing energy between electrons and ions, such as the electron recombination time scale or time scale between Coulomb collisions. If this is true, then collisional equilibrium is achieved in which ionizations are balanced by recombinations. This assumption is valid in the cores of cluster, but may break down in the outer regions of clusters where the density is lower and the plasma may still be in the process of ionizing. One might also worry that this assumption may break down in the cores of clusters if there is a complex multi-phase distribution of plasma temperatures due to thermally unstable pockets of plasma each with their own temperature. Generally if such a situations exists, however, it is likely that each pocket will locally achieve a common temperature. An electron penetrating a cloud of a different temperature will interact and achieve a Maxwellian distribution. It is only with complex and rapidly mixed interfaces that the time scale of injection of a new cloud is much shorter than λ_e/v_e, where v_e is the electron velocity, and λ_e is the electron mean free path, that the collisional equilibrium would be violated.

A.2 Ionization balance

The fraction of atoms at a given charge state is determined by a balance of ionizations and recombinations. The exact balance is fixed by a coupled set of differential equations that relate the ionization and recombination processes between neighboring charge states. The equations are of the form,

$$\frac{dn_i}{dt} = -I_i n_e n_i - R_i n_e n_i + I_{i-1} n_e n_{i-1} + R_{i+1} n_e n_{i+1}. \tag{A.1}$$

where n_e is the electron number density, n_i is the density of atoms in the ith charge state, I_i is the ionization rate out of the ith charge state, and R_i is the recombination rate out of the ith state. We have ignored spatial diffusion of the ionization balance. Note, that it is customary to express the density of a given ion relative to the number density of hydrogen, n_H. We then define a_i as the relative abundance and the fraction of atoms in a given charge state as f_i. Then we have, $n_i = n_H f_i a_i$, where $n_H a_i$ drops out of the above equations. Collisional equilibrium assumes that a steady-state has been achieved, so that the left hand side is set to zero. The equations therefore simplify to equations of the form,

$$0 = -I_i f_i + R_{i+1} f_{i+1} \tag{A.2}$$

Collisional equilibrium will eventually be achieved if a plasma remains undisturbed for a long enough period of time (i.e., the inverse of the recombination rate). Several calculations have been done to determine this ionization balance as a function of the electron temperature (Jordan 1969; Arnaud & Rothenflug 1985; Arnaud & Raymond 1992; Mazzotta et al. 1998). One such calculation is shown in Figure A.1.

Once the ionization balance is determined the X-ray spectrum can be calculated by considering the various radiation processes. The most important processes are bremsstrahlung and the K and L shell transitions for the discrete line emission.

A.3 Bremsstrahlung and other continuum processes

When hydrogen is ionized above temperatures of 2×10^4 K, copious amounts of bremsstrahlung emission are produced. Bremsstrahlung radiation results from the accelerations of the free electrons in the Coulomb field of an ion. The spectrum is roughly independent of energy below the energy equal to kT_e, where T_e is the electron temperature and k is Boltzmann's constant. A rough approximation of the power per energy per volume radiated by bremsstrahlung is given by the equation below,

$$\frac{d^2P}{dV\,dE} \approx 10^{-11}\ n_e\ n_H\ T^{-\frac{1}{2}} e^{-\frac{E}{kT}}\ \text{cm}^{-3}\ \text{s}^{-1} \tag{A.3}$$

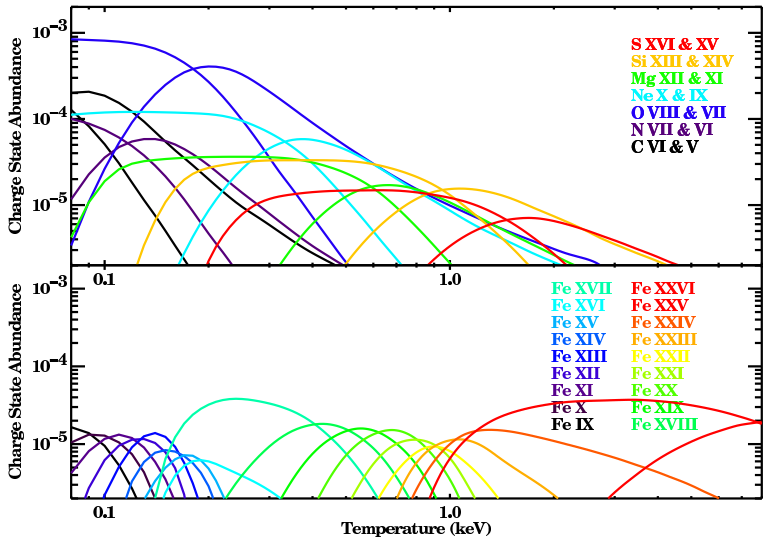

Figure A.1: The charge state abundance (elemental abundance times fraction ionic abundance) of various ions as a function of temperature. The top panel shows He-like and H-like charge states of various low Z atoms. The bottom panel shows iron ions having the outer electron in the K, L, and M shell. The bottom panel indicates how the measurement of various ions in the iron series is a sensitive probe of the plasma temperature. Figure uses data from Arnaud & Raymond (1992)).

where n_e is the electron density, n_H is the hydrogen density, E is the photon energy, k is Boltzmann's constant, and T is the electron temperature in Kelvin. The total power radiated is therefore,

$$\frac{dP}{dV} \approx 10^{-27}\ n_e\ n_H\ T^{\frac{1}{2}}\ \text{ergs cm}^{-3}\ \text{s}^{-1} \tag{A.4}$$

In addition to bremsstrahlung, bound-free emission (the capture of a free electron to a bound state) and two-photon emission (which occurs most frequently following a collisional excitation of Hydrogen to the 2s level) are also significant source of continuum radiation. They both modify the shape of the continuum emission.

A.4 Discrete line emission

Discrete line emission is formed by a number of atomic processes. The most important atomic processes are collisional excitation, radiative recombination, dielectronic recombination, and resonant excitation. Generally, the processes have been incorporated in a number of publically available and well-tested codes that are used to study collisionally-ionized spectra.

The strength of an emission line is determined by the excitation and recombination rates, which are proportional to the integral of the velocity times the cross-section for a particular process over a Maxwellian distribution. The volume emissivity for a given emission line is calculated by equations of the form,

$$\epsilon = n_e n_i \left(C^{II} f_{i-1} + C^E f_i + \alpha^R f_{i+1} \right) \tag{A.5}$$

where C^{II} is the rate of inner shell ionization processes, C^E is the sum of collisional excitation processes, and α^R is the sum of recombination processes. Several well tested codes have been developed to calculate the emergent spectrum by assuming an ionization calculation and including a set of excitation and recombinations rates. These include the Raymond-Smith (Raymond & Smith 1977), MEKA (Mewe et al. 1985; Mewe et al. 1986; Kaastra 1992; Mewe et al. 1995), MEKAL (Liedahl et al. 1995), and APEC codes (Smith et al. 2001). These codes are compilations of the results of more detailed atomic codes, which solve the Dirac equation either by the distorted wave approximation (Bar-Shalom et al. 2001; Gu 2003) or R-matrix methods (Berrington et al. 1994). The number of transitions and the accuracy of the detailed processes limits the results. Extensive laboratory work has been applied to verify wavelengths (Brown et al. 1998; Brown et al. 2002) and cross-sections (Gu et al. 1999; Chen et al. 2005) of the transitions.

Table A.1: Important line transition blends in optically-thin collisionally ionized plasmas.

Ion[a]	Wavelengths [Å]	Energies [keV]	Temperatures [keV][b]
Fe XXVI	1.8	6.97	> 3.0
Fe XXV	1.9, 1.9	6.70, 6.63	$1.0 - 8.0$
Fe XXIV	10.6, 11.2	1.17, 1.11	$0.9 - 4.0$
Fe XXIII	11.0, 11.4, 12.2	1.13, 1.09, 1.02	$0.8 - 2.0$
Fe XXII	11.8, 12.2	1.05, 1.02	$0.6 - 1.5$
Fe XXI	12.2, 12.8	1.02, 0.97	$0.5 - 1.0$
Fe XX	12.8, 13.5	0.97, 0.92	$0.4 - 1.0$
Fe XIX	13.5, 12.8	0.92, 0.97	$0.3 - 0.9$
Fe XVIII	14.2, 16.0	0.87, 0.77	$0.3 - 0.8$
Fe XVII	15.0, 17.1	0.83, 0.73	$0.2 - 0.6$
S XXVI	4.7	2.62	> 1.0
S XXV	5.1, 5.0	2.43, 2.46	$0.3 - 1.0$
Si XIV	6.2	2.00	> 1.0
Si XIII	6.6, 6.7	1.87, 1.84	$0.2 - 1.0$
Mg XII	8.4	1.47	> 0.7
Mg XI	9.2, 9.3	1.35, 1.33	$0.1 - 0.6$
Ne X	12.2	1.02	> 0.4
Ne IX	13.5, 13.7	0.92, 0.90	$0.1 - 0.3$
O VIII	19.0, 16.0	0.64	> 0.2
O VII	21.6, 22.0	0.57, 0.56	$0.1 - 0.2$
N VII	24.8	0.50	> 0.1
C VI	33.7	0.37	> 0.1

[a] The line transition list is somewhat crude since here line blends are tabulated rather than actual transitions. However, it matches well with the quality of the observations.

[b] The temperature ranges are calculated to roughly show where the emissivity of a given ion blend is within an order of magnitude of its peak emissivity.

A number of common spectral transitions occur in most X-ray spectra. In fact, despite the complexity implied by the above discussion there are usually only a couple of dozen strong transitions that are used to determine most of the information that can be extracted from the X-ray spectrum. Several of the important emission line blends are shown in Table A.1.

A.5 X-ray cooling function and emission measure distribution

The X-ray cooling function is calculated by integrating the emission from all processes and weighting by the energy of the photons.

$$\Lambda\left(T, Z_i\right) = \int_0^\infty dE \; E \; \frac{d\alpha}{dE}(E, T, Z_i) \tag{A.6}$$

where $\frac{d\alpha}{dE}$ is the energy dependent line power (or continuum power). The cooling function relates the total amount of energy emitted per volume for a given amount of plasma with a given temperature and emissivity. The cooling function has been compiled in various tables (Böhringer & Hensler 1989; Sutherland & Dopita 1993), some examples are displayed in Fig. A.2.

The relative distribution of plasma at a set of temperatures is often expressed in terms of an emission measure distribution. The differential emission measure, $\frac{dEM}{dT}$ is defined by

$$\frac{d\epsilon}{dE} = \int_0^\infty \frac{dEM}{dT} \; \frac{d\alpha}{dE}(E, T) \; dT \; . \tag{A.7}$$

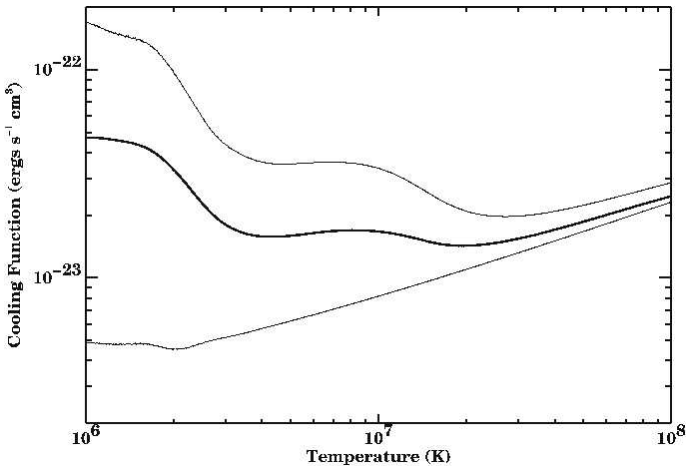

Figure A.2: Radiative cooling function for solar abundances (top curve), one-third solar abundances (middle), and pure Hydrogen and Helium (bottom) as a function of the temperature. The X-ray region from 10^6 to 10^8 K is dominated by bremsstrahlung at high temperatures as well as significant contribution from line emission at lower temperatures. Below 10^6 K, in the UV temperature range, the cooling function rises significantly.

where $\frac{d\epsilon}{dE}$ is the energy-dependent emissivity and the integral is over all temperatures. It is also convenient to express the distribution of plasma temperatures in terms of the differential luminosity, which is defined by

$$\frac{dL}{dT} = \frac{dEM}{dT}\Lambda(T) \ . \tag{A.8}$$

A.6 Cooling time

The cooling time of an optically-thin plasma is the gas enthalpy divided by the energy lost per unit volume of the plasma. The gas enthalpy is $\frac{5}{2}nkT$ and the energy lost per volume is the electron density squared times the cooling function. The cooling time can then be written as,

$$t_{cool} \equiv \frac{\frac{5}{2}nkT}{n^2\Lambda} \approx t_H T_8 \Lambda_{-23}^{-1} n_{-2}^{-1} \tag{A.9}$$

where t_H is the age of the universe ($\sim$ 13.7 Gyr), T_8 is the temperature in units of 10^8 K, Λ_{-23} is the cooling function in units of 10^{-23} ergs cm^3 s^{-1}, and n_{-2} is the density in units of 10^{-2} particles cm^{-3}. We used the gas enthalpy per volume, $\frac{5}{2}nkT$ instead of the thermal energy per volume $\frac{3}{2}nkT$ since the plasma is compressed as it cools which therefore effectively raises its heat capacity by a factor of $\frac{5}{3}$. Therefore, X-ray plasma with gas density above 10^{-2} cm^{-3} has had sufficient time to cool. In the cores of cooling clusters the cooling time approaches cooling times below 5×10^8 yr. If the gas was undisturbed, it would have a chance to cool several times. Note that as gas cools at constant pressure (due to the weight of overlying gas) then the rise in density as the temperature drops means that $t_{\rm cool}$ becomes shorter and shorter.

A.7 Optical depth, resonance scattering, and opacity

The optical depth for photons of a given wavelength, τ, is the product of the column density of a particular ion, N_i and the cross-section of a particular process. The cross-section is a function of the energy. The column density is the line integral of the ion density, n_i, which is a function of the spatial position along the line of sight.

The ICM is, for the most part, optically-thin to its own radiation (i.e. photons escape once they are emitted without interacting again). Photons with energies close to certain resonance transitions, however, can scatter several times before leaving a cluster. The optical depth to a resonance transition is given by

$$\tau = \int dln_i f_i \frac{\pi e^2}{m_e c} \frac{exp^{-\frac{(\lambda-\lambda_i)^2}{2\sigma_i^2}}}{\sqrt{2\pi\sigma_i^2}} \tag{A.10}$$

where n_i is the ion density, f_i is the oscillator strength of the transition, m_e is the electron mass, λ_i is the wavelength of the transition, c is the speed of light, e is the electron charge, and σ_i is the line width given by,

$$\sigma_i = \lambda_i \sqrt{\frac{kT}{\left(\frac{A}{1+\frac{5}{3}M^2\frac{A}{\mu}}\right) m_p c^2}} \tag{A.11}$$

where A is the atomic mass number, μ is the mean mass per particle, M is the Mach number of the turbulence or gas motions in the plasma, k is Boltzmann's constant, and T is the temperature. The above expression includes both the thermal broadening of the line as well as turbulent broadening.

If a significant quantity of lowly ionized matter exists along the line of sight, X-rays can be absorbed and re-emitted at lowly ionized longer wavelengths. This situation occurs frequently for absorption from neutral gas in the Milky Way Galaxy, but could also occur from gas trapped in the cluster potential. We note that understanding the role of absorption often has a significant effect on the interpretation of the soft X-ray spectrum. This is particularly true at low resolution. He K-shell absorption at low energies and O K-shell absorption at 23.5 Å are the largest contributors to the opacity from a neutral absorber and produce absorption edge features in the spectrum.

Appendix B

Analysis of simulated X-ray spectra of clusters

In this section we investigate the presence of a possible bias in the measure of Z_{Fe} in our analysis procedure. In particular, we check whether unresolved gradients in the temperature or in the iron abundance distribution can affect the observed trends, paying particular attention to the low S/N regime of our spectra. We perform several simulations of spectra with different assumptions, as described in detail in the following subsections, and explore the possible conditions that can potentially affect the distribution of best-fit values of kT and, most important, of Z_{Fe}. The median of the distribution of best-fit values and the 16% and 84% percentiles (corresponding to the 1σ confidence level) will finally be compared to the input values of temperature and metallicity.

B.1 Fitting bias in isothermal, constant metallicity, low S/N spectra

A first simple test is to check the accuracy that we can achieve in recovering the input parameters of temperature and metallicity from spectra simulated with the typical S/N, temperatures and redshifts of clusters in our sample, under the assumption of a single-temperature `mekal` model. This may seem a redundant exercise. However a potential problem rises from the fact that upper limits on temperature are typically less constrained than lower limits. This effect increases at high temperatures, when the exponential cut off of the thermal spectrum shifts to energies for which the effective area of the detectors is low. As a consequence, if temperature best-fit values tend to be scattered upwards for low S/N, the estimated continuum may be higher than the actual one, and therefore the measured equivalent width of the iron lines may be underestimated. On the other hand, variations in the best-fit temperatures affect the ion abundances too. Spectral simulations can be used to investigate how these aspects affect the measure of Z_{Fe} at low S/N as a function of redshift.

In principle, the parameter space to explore is fairly wide: input metallicity, input temperature, redshifts, and S/N (measured as $S/N \equiv C_s/\sqrt{C_{tot} + C_{bck}}$, where C_s is the number of net counts from the source, C_{tot} the number of source plus background counts, and C_{bck} the number of estimated background counts in the source area). For simplicity, we have decided to restrict the simulations to a few relevant cases. We chose an input metallicity of $Z_{Fe} = 0.3\,Z_{\odot}$, redshift $z = 0.4$, and temperatures of $kT = 3.5$ and 7 keV. We took the observation of V 1416 as a template: the exposure time is 30 ks and the extraction radius $74''$. The simulations were performed for four different values of S/N (corresponding to 1850, 1000, 500, and 200 net counts). We also run two simulations for $z = 1$. Each combination of parameters was simulated 1000 times. The simulations were performed with XSPEC using a `mekal` model. We analyzed each simulated spectrum by adopting the same input model. In Table B.1 we list the median of the distributions of the best-fit values for temperature and Z_{Fe}. Errors on the median are the 16% and 84% percentiles.

The results are summarized in Fig. B.1. We notice that, as expected, the low S/N spectra tend to have higher median best-fit temperatures compared to the input values. This translates into a slightly higher median of the best-fit Z_{Fe} than the input value, which is always $Z_{Fe} = 0.3\,Z_{\odot}$ for this set of

Table B.1: Results from the spectral simulations described in Appendix A.1.

Sim[a]	net cts[b]	S/N[c]	kT_{inp}[d]	Z_{inp}[e]	z[f]	kT_{fit}[g]	Z_{fit}[h]
s01	1855	34.4	3.5	0.3	0.4	$3.66^{+0.27}_{-0.28}$	$0.33^{+0.15}_{-0.15}$
s02	1000	22	3.5	0.3	0.4	$3.82^{+0.48}_{-0.41}$	$0.36^{+0.31}_{-0.22}$
s03	500	12	3.5	0.3	0.4	$4.15^{+1.01}_{-0.63}$	$0.44^{+0.46}_{-0.42}$
s04	200	5.6	3.5	0.3	0.4	$5.5^{+6.5}_{-1.9}$	$0.44^{+1.52}_{-0.44}$
s05	1920	35.2	7	0.3	0.4	$7.5^{+1.0}_{-0.9}$	$0.32^{+0.18}_{-0.19}$
s06	990	22	7	0.3	0.4	$7.95^{+2.17}_{-2.49}$	$0.32^{+0.31}_{-0.28}$
s07	520	13	7	0.3	0.4	$9.45^{+5.75}_{-2.65}$	$0.40^{+0.61}_{-0.40}$
s08	330	8.9	7	0.3	0.4	$11.8^{+18.7}_{-5.3}$	$0.55^{+1.23}_{-0.55}$
s09	1000	22	7	0.3	1.0	$8.07^{+1.78}_{-1.39}$	$0.29^{+0.27}_{-0.28}$
s10	500	12.7	7	0.3	1.0	$9.0^{+4.0}_{-2.1}$	$0.28^{+0.62}_{-0.28}$

Notes: [a] simulations identification number; [b] net number of counts; [c] signal-to-noise ratio; [d] input temperature; [e] input iron abundance; [f] redshift; [g] median values of the distribution of best-fit temperatures; [h] median values of the distribution of best-fit iron abundances. Lower and upper errors correspond to the 16% and 84% percentiles, respectively.

simulations. However, for $S/N < 20$, the distribution of best-fit values is largely scattered around the input values. At higher redshifts, the situation for a given S/N improves slightly, since the exponential cutoff moves towards the most sensitive energy range of *Chandra*, and both the temperature and the abundance estimates are closer to the input values. We conclude that, under the assumption of a single temperature, single metallicity thermal plasma, the best-fit values of Z_{Fe} are not significantly biased, within the typical S/N and redshift range of our sample.

B.2 Fitting bias in two-temperature, constant-metallicity spectra

Here we intend to investigate whether the presence of substantial temperature structure can affect the measure of the iron abundance when the spectra are analyzed with a single-temperature `mekal` model, as adopted in this work. In some cases in our spectra, we are able to detect the presence of a temperature decrease towards the center; however, we are not able to perform a spatially-resolved spectral analysis for the large majority of clusters in our sample.

Since there are no canonical, physically-motivated, multiphase models of the ICM, we simply assume a double `mekal` model. Again, the free parameter space is wide, therefore here we only explore a few cases. In particular, we performed a set of simulations of a cluster with two temperature components (2 and 7 keV), with an emission measure ratio (EM, the normalization of the `mekal` model) of the cold to the hot component ranging from 0.3 to 0.75. The choice of the temperature range here agrees with the observational evidence that the minimum temperature in cool cores is always equal to or higher than one third of the maximum value of the hot component (see Peterson et al. 2003). The iron abundance is set to $0.3\,Z_{\odot}$ in both components. We simulated 1000 spectra for each case at redshift $z = 0.6$ and $z = 1$. We took the observation of RX J0542 as a template: the exposure time is 50 ks and the extraction radius is $79''$. The results are listed in Table B.2, and shown in Fig. B.2. Obviously, for a given redshift, the best-fit temperature, which is always intermediate between the two input values, moves towards the low value for increasing values of the cold to hot EM ratio. But, for a given EM value, the median of the best-fit temperature moves towards higher values for higher redshifts, since the cold components is redshifted out of the adopted energy range ($0.6 - 8$ keV). We note that, despite a two-temperature structure being fitted with a single-temperature, the fits are acceptable in the selected cases, due to the low number of total net counts (below 2000), representing the typical condition under which the presence of two temperatures cannot be established from the spectral analysis.

As for Z_{Fe}, the median of the distribution of the best-fit values is slightly lower at $z = 1$ than at $z = 0.6$. The effect is a decrement of less than 30% up to $z = 1$. Given the large dispersion of the best-fit values, this effect is probably not playing a dominant role in our observed trend. However, a proper investigation of the effect of a multi-temperature ICM must rely on a physical modelization of the ICM multiphase structure, which is presently missing.

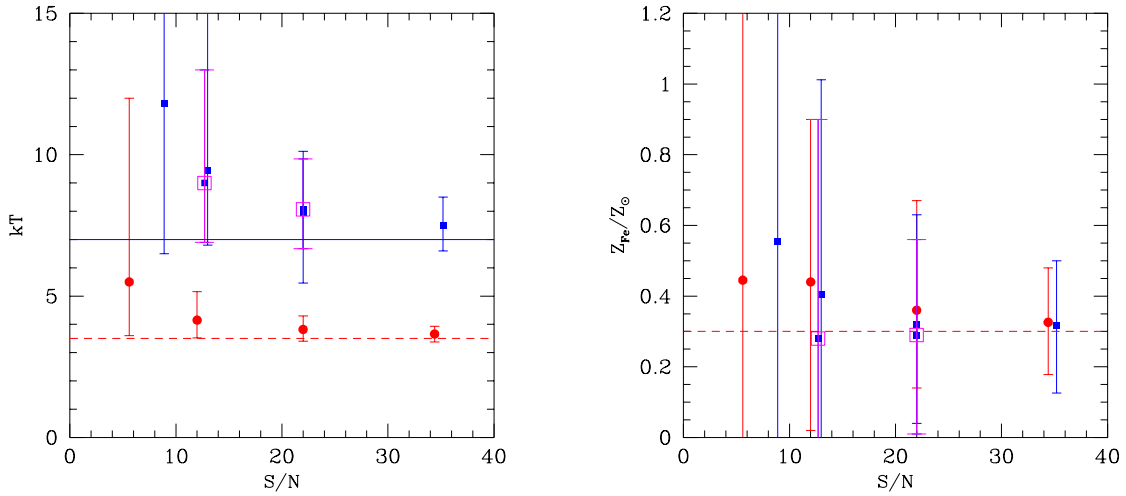

Figure B.1: *(Left panel)* Median of the best-fit temperature distribution as a function of S/N. Red solid circles refer to an input temperature value of 3.5 keV (dashed horizontal line), while blue solid squares to 7 keV (solid horizontal line). Empty squares are for $z = 1$. Lower and upper error bars correspond to the 16% and the 84% percentiles, respectively. *(Right panel)* Median of the best-fit Z_{Fe} distribution as a function of S/N. The input value is always $Z_{Fe} = 0.3\,Z_{\odot}$ (horizontal dashed line). Symbols and error bars are as in the upper panel; magenta empty squares are for $z = 1$.

Table B.2: Results from the spectral simulations of two temperature components, analyzed with a single-temperature `mekal` model, as described in Appendix A.2.

Sim[a]	net counts (H+C)[b]	EM ratio[c]	S/N[d]	kT_{inp}[e]	Z_{inp}[f]	z[g]	kT_{fit}[h]	Z_{fit}[i]
s11	1560+390	0.575	30.3	7+2	0.3	0.6	$4.9^{+0.65}_{-0.5}$	$0.32^{+0.13}_{-0.16}$
s12	1410+540	0.287	30.3	7+2	0.3	0.6	$5.95^{+0.7}_{-0.65}$	$0.29^{+0.16}_{-0.15}$
s13	918+175	0.287	19.1	7+2	0.3	0.6	$6.4^{+1.4}_{-0.9}$	$0.31^{+0.21}_{-0.22}$
s14	870+170	0.34	19.8	7+2	0.3	1.0	$6.75^{+1.45}_{-1.1}$	$0.26^{+0.23}_{-0.19}$
s15	550+105	0.34	12.3	7+2	0.3	1.0	$7.4^{+2.6}_{-1.7}$	$0.25^{+0.27}_{-0.25}$
s16	580+200	0.75	12.7	7+2	0.3	1.0	$6.1^{+1.8}_{-1.4}$	$0.20^{+0.33}_{-0.20}$

Notes: [a] simulations identification number; [b] net number of counts of the hot and cold component; [c] emission measure ratio; [d] signal-to-noise ratio; [e] input temperature of the hot and cold component; [f] input iron abundance; [g] redshift; [h] median values of the distribution of best-fit temperatures; [i] median values of the distribution of best-fit iron abundances. Lower and upper errors correspond to the 16% and 84% percentiles, respectively.

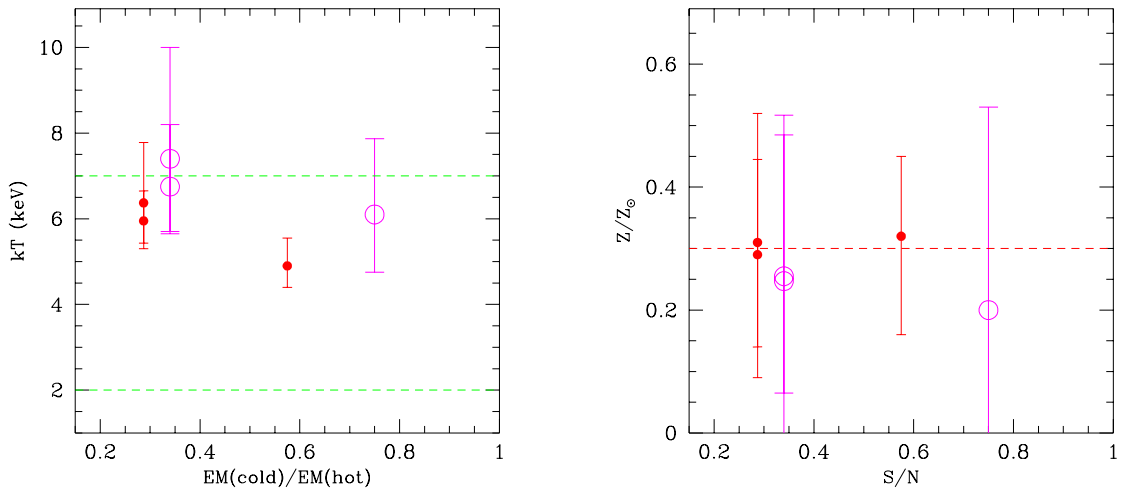

Figure B.2: *(Left panel)* median values of the best-fit temperature distribution as a function of the ratio of the cold and hot emission measure. Input temperatures are 2 and 7 keV (horizontal dashed lines). Filled circles are for $z = 0.6$, while empty circles are for $z = 1$. Lower and upper error bars correspond to the 16% and 84% percentiles, respectively. *(Right panel)* median values of the best-fit Z_{Fe} distribution as a function of the ratio of the cold and hot emission measure. Symbols and errors as in the upper panel.

B.3 Fitting bias in low S/N spectra with temperature and metallicity gradients

We investigate the distribution of best-fit values for Z_{Fe} in the case of an ICM having significant temperature and metallicity structures at the same time. In particular, we investigate the most common case of higher Z_{Fe} associated with lower temperature components, as found in the cool cores. We repeated the simulations performed in Appendix A.2, by assigning an iron abundance of $0.6\,Z_{\odot}$ to the cold component. The results are listed in Table B.3, and shown in Fig. B.3. The best-fit temperature has the same behavior as described in Appendix A.2. For Z_{Fe} as well the situation is analogous to the previous case, with the median values slightly biased towards higher values. From a visual inspection of Figs. B.2 and B.3, we notice that the average best-fit values are lower for $z = 1$ compared with $z = 0.6$, by an amount on the order of 30%. On the basis of this result, we might expect that the presence of cool, metal-rich cores, could mimic the observed negative evolution from $Z_{Fe} \simeq 0.4\,Z_{\odot}$ at $z \sim 0.3$ to $Z_{Fe} \simeq 0.2\,Z_{\odot}$ at $z \sim 1.3$ without an effective decrease in the amount of iron in the central regions. However, this effect would explain only part of the observed trend even in the extreme case in which all the clusters in the sample had strong temperature and metallicity gradients. Therefore, we can conclude that the observed evolution of Z_{Fe} cannot be ascribed entirely to K-correction effects. We also notice that the limited effect of a central cold and metal-rich component in high-z clusters, also implies that the Z_{Fe}-temperature correlation cannot be simply explained by the occurrence of cool cores with temperature below 2 keV in clusters with virial temperatures $kT \leq 5$ keV.

B.4 Fitting bias in isothermal spectra rich in α-element

Finally, we checked whether a non-solar abundance ratio can affect the measure of Z_{Fe}. In particular, we checked whether higher abundances of S, Si and O can artificially yield a higher Z_{Fe}. Therefore, we tried to recover the iron abundance with a `mekal` model, when the metallicity ratio among elements is higher than solar. The simulated spectra have the following input: $Z_{Fe} = 0.3$ and $Z_{\alpha} = 1$ or $Z_{\alpha} = 2$. We recall that these are extreme cases with respect to the abundances of α-elements observed in local X-ray clusters (see Tamura et al. 2004). We simulated 1000 spectra of a $z = 0.4$ cluster with $kT = 3.5$ keV

Table B.3: Results from the spectral simulations of two components with different temperatures and iron abundances, analyzed with a single-temperature `mekal` model, as described in Appendix A.3.

Sim[a]	net counts (H+C)[b]	EM ratio[c]	S/N[d]	kT_{inp}[e]	Z_{inp}[f]	z[g]	kT_{fit}[h]	Z_{fit}[i]
s17	1410+650	0.575	31.6	7+2	0.3+0.6	0.6	$4.41^{+0.46}_{-0.37}$	$0.41^{+0.15}_{-0.14}$
s18	1640+370	0.287	31	7+2	0.3+0.6	0.6	$5.48^{+0.67}_{-0.60}$	$0.35^{+0.15}_{-0.14}$
s19	920+210	0.287	19.5	7+2	0.3+0.6	0.6	$6.0^{+1.2}_{-0.1}$	$0.33^{+0.25}_{-0.21}$
s20	870+200	0.34	18.8	7+2	0.3+0.6	1.0	$6.4^{+1.3}_{-0.9}$	$0.25^{+0.22}_{-0.20}$
s21	550+125	0.34	12.6	7+2	0.3+0.6	1.0	$7.25^{+2.55}_{-1.7}$	$0.26^{+0.35}_{-0.26}$
s22	480+240	0.75	13.3	7+2	0.3+0.6	1.0	$5.51^{+2.5}_{-1.1}$	$0.29^{+0.28}_{-0.28}$

Notes: [a] simulations identification number; [b] net number of counts of the hot and cold component; [c] emission measure ratio; [d] signal-to-noise ratio; [e] input temperature of the hot and cold component; [f] input iron abundance of the hot and cold component; [g] redshift; [h] median values of the distribution of best-fit temperatures; [i] median values of the distribution of best-fit iron abundances. Lower and upper errors correspond to the 16% and 84% percentiles, respectively.

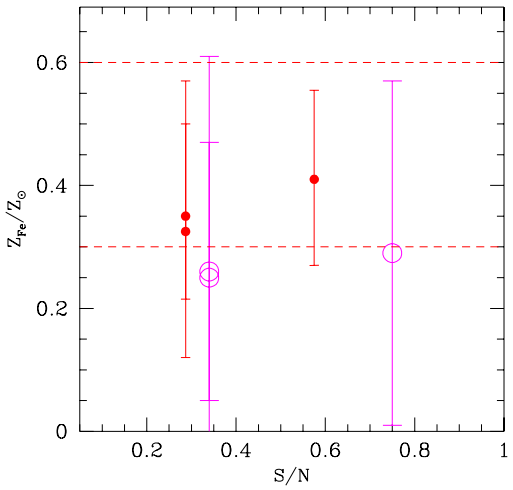

Figure B.3: Median of the best-fit Z_{Fe} distribution as a function of the ratio of the Cold and Hot Emission Measure, for simulations where the cold component has an iron abundance twice higher than the hot component ($0.6\,Z_{\odot}$ vs $0.3\,Z_{\odot}$). Filled circles are for $z = 0.6$, while empty circles are for $z = 1$. Lower and upper error bars correspond to the 16% and the 84% percentiles, respectively.

(2060 net counts expected) and with $kT = 2$ keV (2300 net counts expected), maximizing the presence of lines from α-elements in our energy range (lowest redshift and lowest temperature in our sample). We find that the temperatures are slightly higher that the input values in both cases ($kT = 3.8 \pm 0.29$ and 2.45 ± 0.12 keV), while iron abundances are consistent ($0.30 \pm 0.12\, Z_\odot$ and $Z = 0.25^{+0.13}_{-0.10}\, Z_\odot$ for $kT = 3.5$ and 2 keV, respectively). Therefore no bias is found in the measure of Z_{Fe}, confirming the expectation that the iron abundance is mostly determined by the K-shell complex at $6.7 - 6.9$ keV and is not affected by the L-shell complex below 2 keV, where the iron emission lines are blended to that of Si, O, and Mg.

Appendix C

Images and spectra of high-z clusters

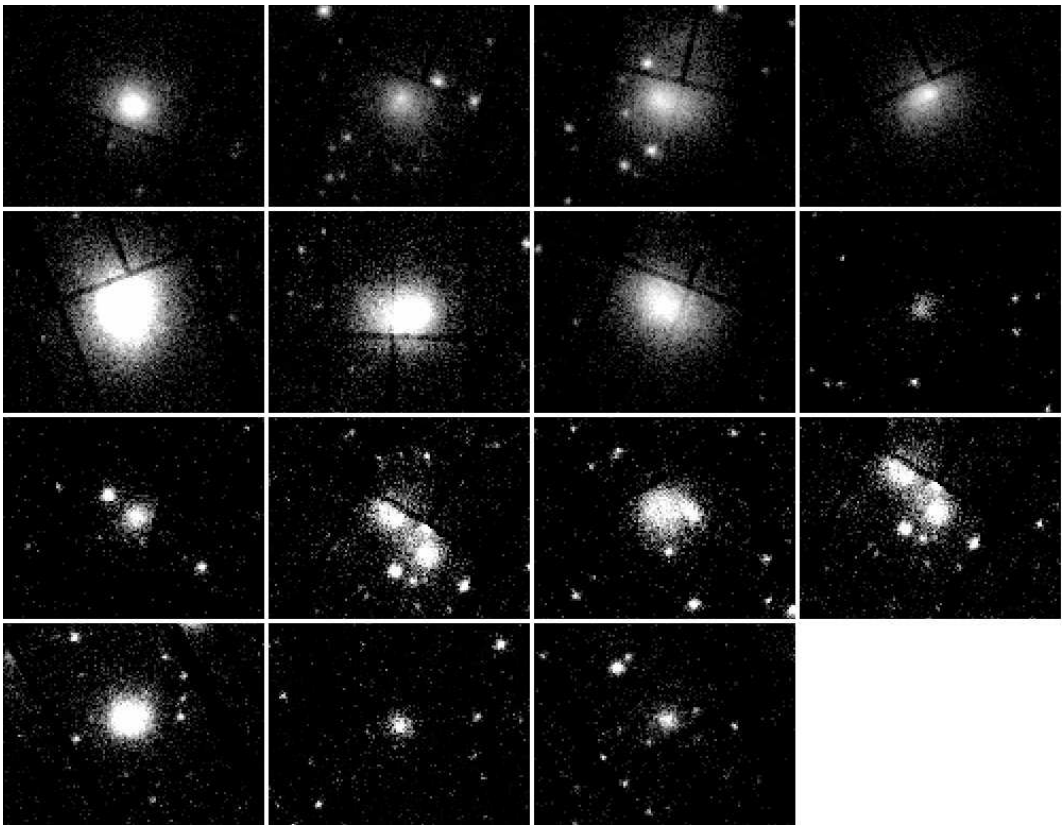

Figure C.1: XMM-*Newton* full band images of the sample analyzed in Chapter 3. Each cut-out has an angular size of $8' \times 6'$. The clusters are sorted by increasing redshift from $z = 0.3$ (*top-left*) to $z = 1.27$ (*bottom-right*).

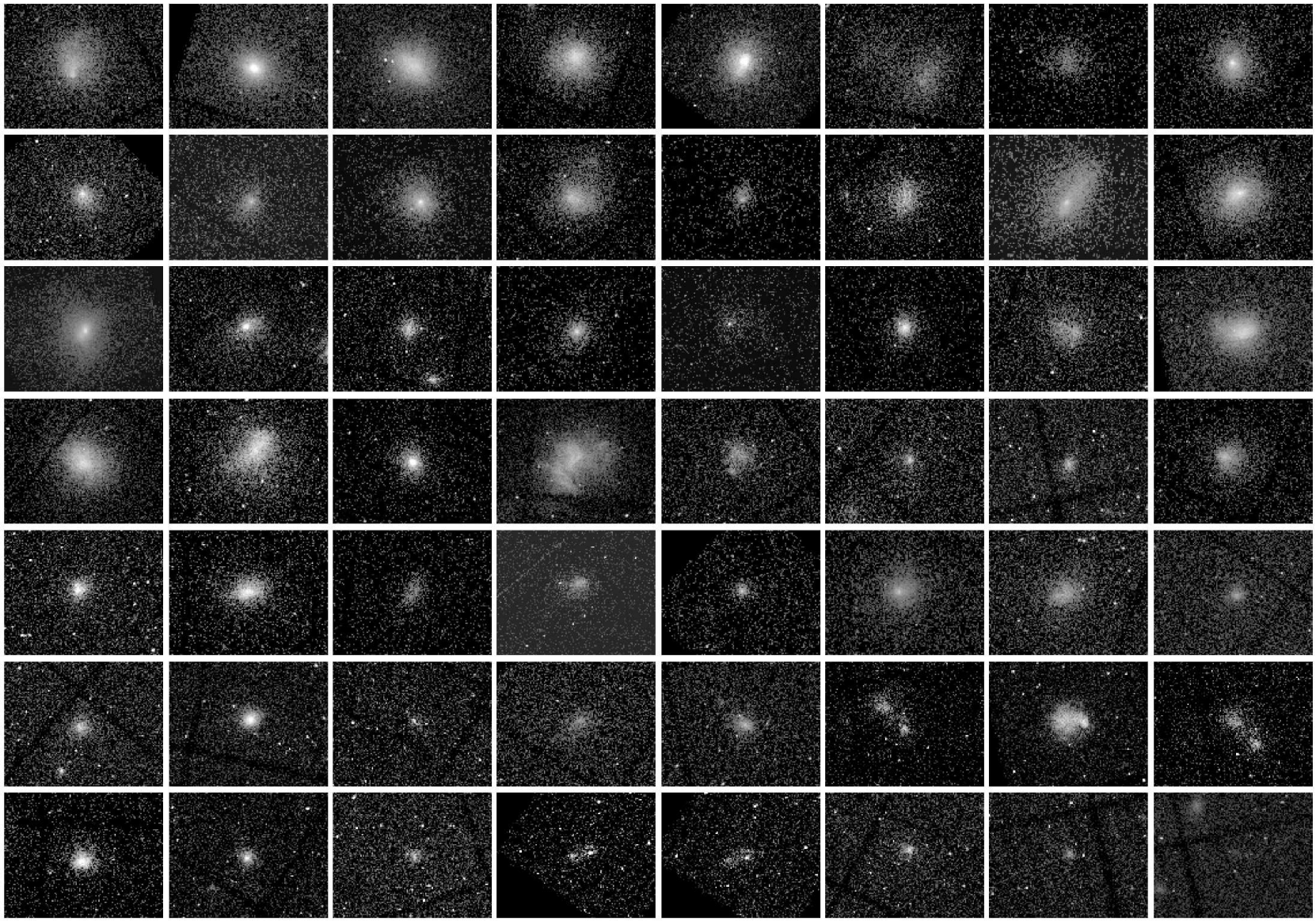

Figure C.2: Chandra full band images of the whole sample. Each cut-out has an angular size of $8' \times 6'$. The clusters are sorted by increasing redshift from $z = 0.3$ (*top-left*) to $z = 1.27$ (*bottom-right*).

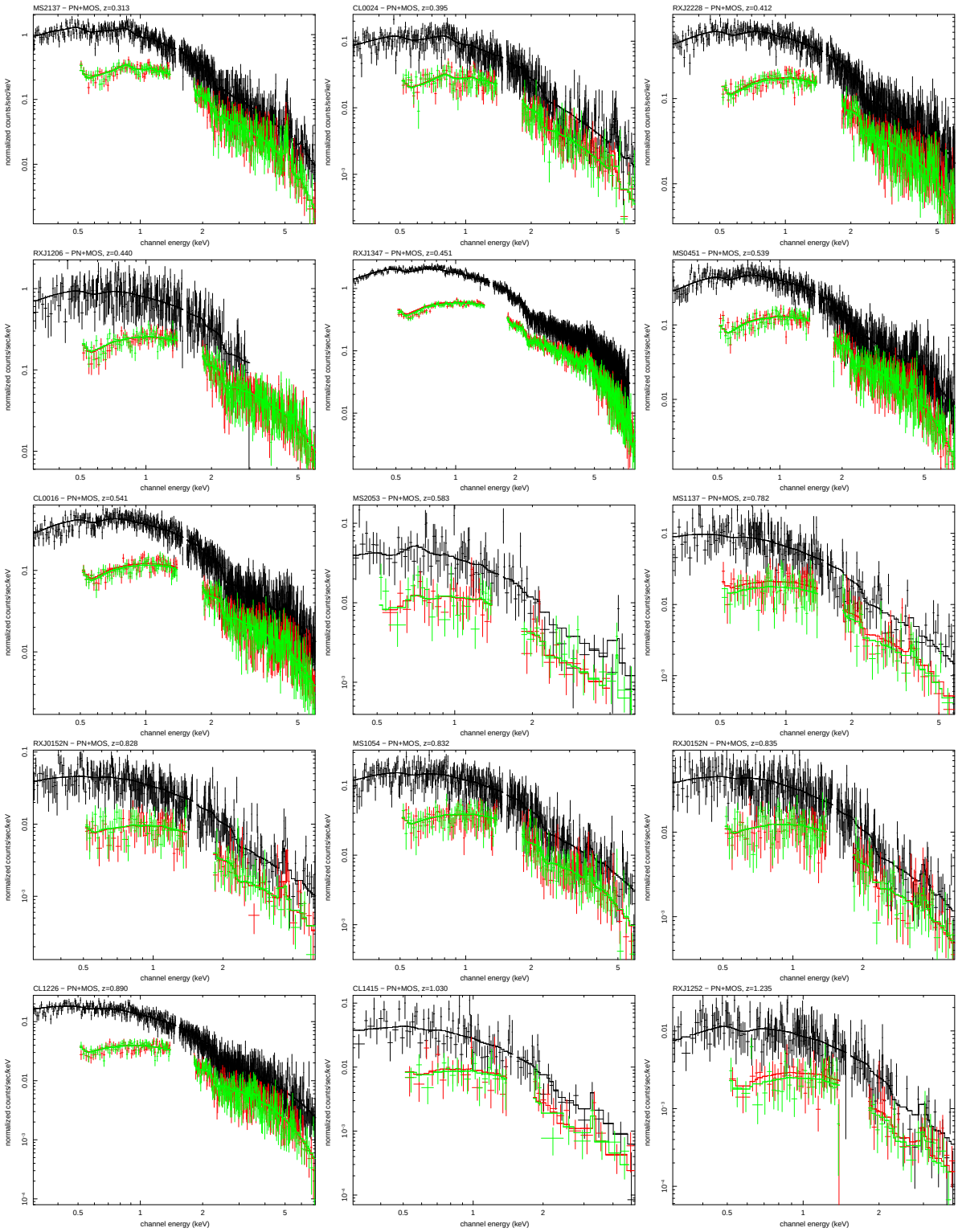

Figure C.3: XMM-*Newton* spectra of the high-z cluster sample presented in Chapter 3 and best-fit obtained with the `MEKAL` model, as described in the text (see Sect. 3.2.1). The PN (*black*), MOS1 (*red*) and MOS2 (*green*) spectra have been re-binned here for illustration purposes.

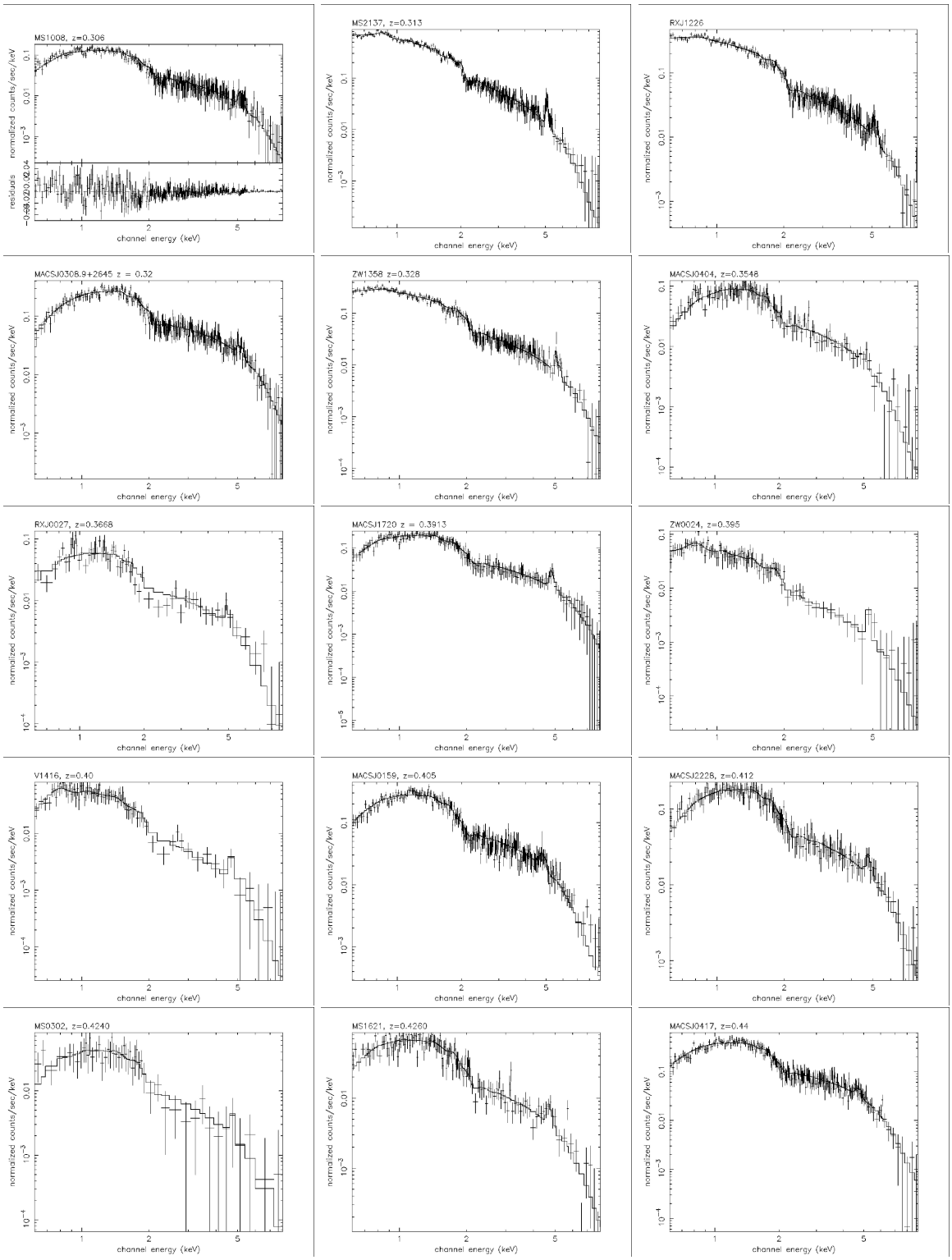

Figure C.4: Chandra spectra of the high-z cluster sample presented in Chapter 2 and best-fit obtained with the `MEKAL` model, as described in the text (see Sect. 2.3.1). The spectra have been re-binned here for illustration purposes.

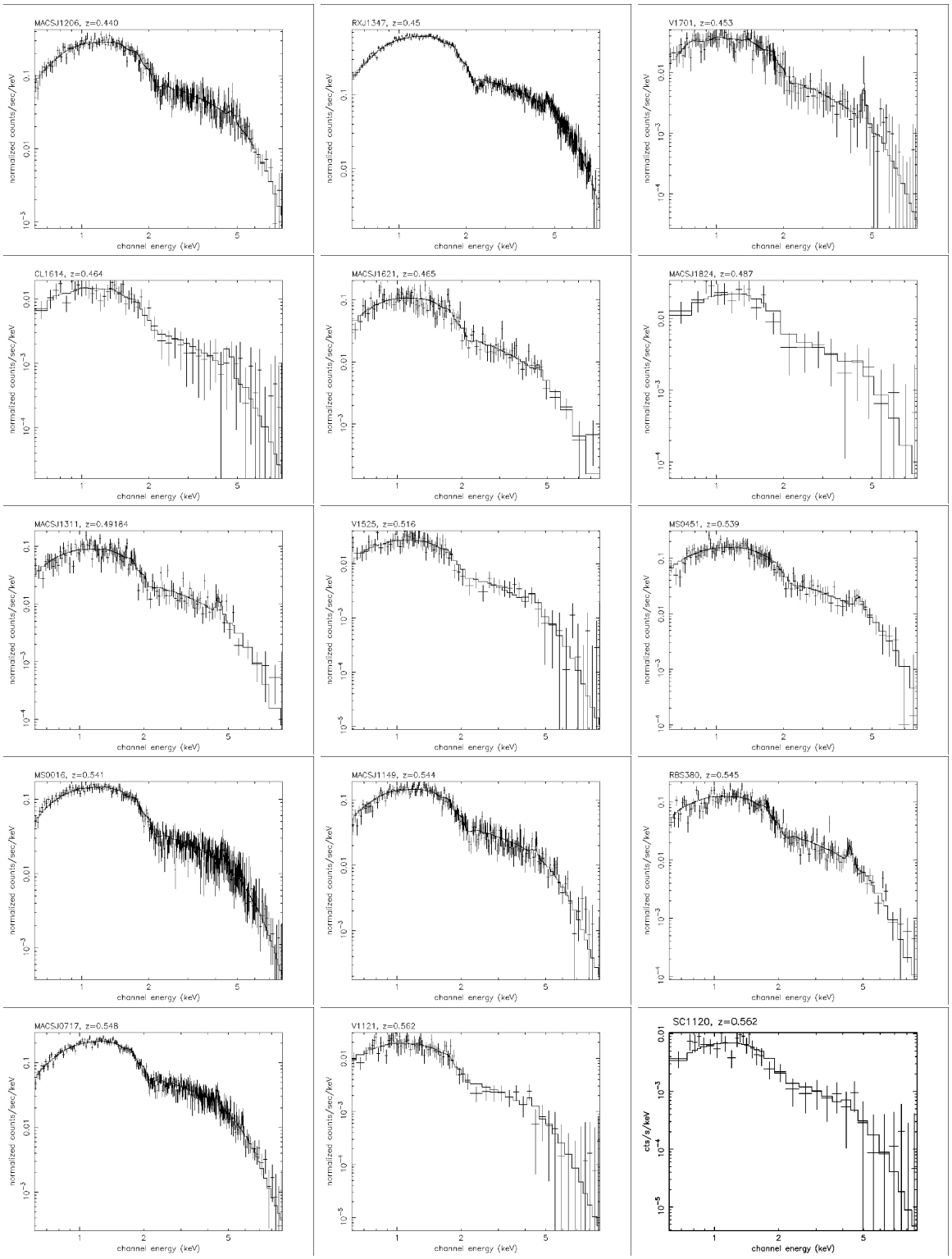

Figure C.5: Chandra spectra of the high-z cluster sample presented in Chapter 2 and best-fit obtained with the `MEKAL` model, as described in the text (see Sect. 2.3.1). The spectra have been re-binned here for illustration purposes.

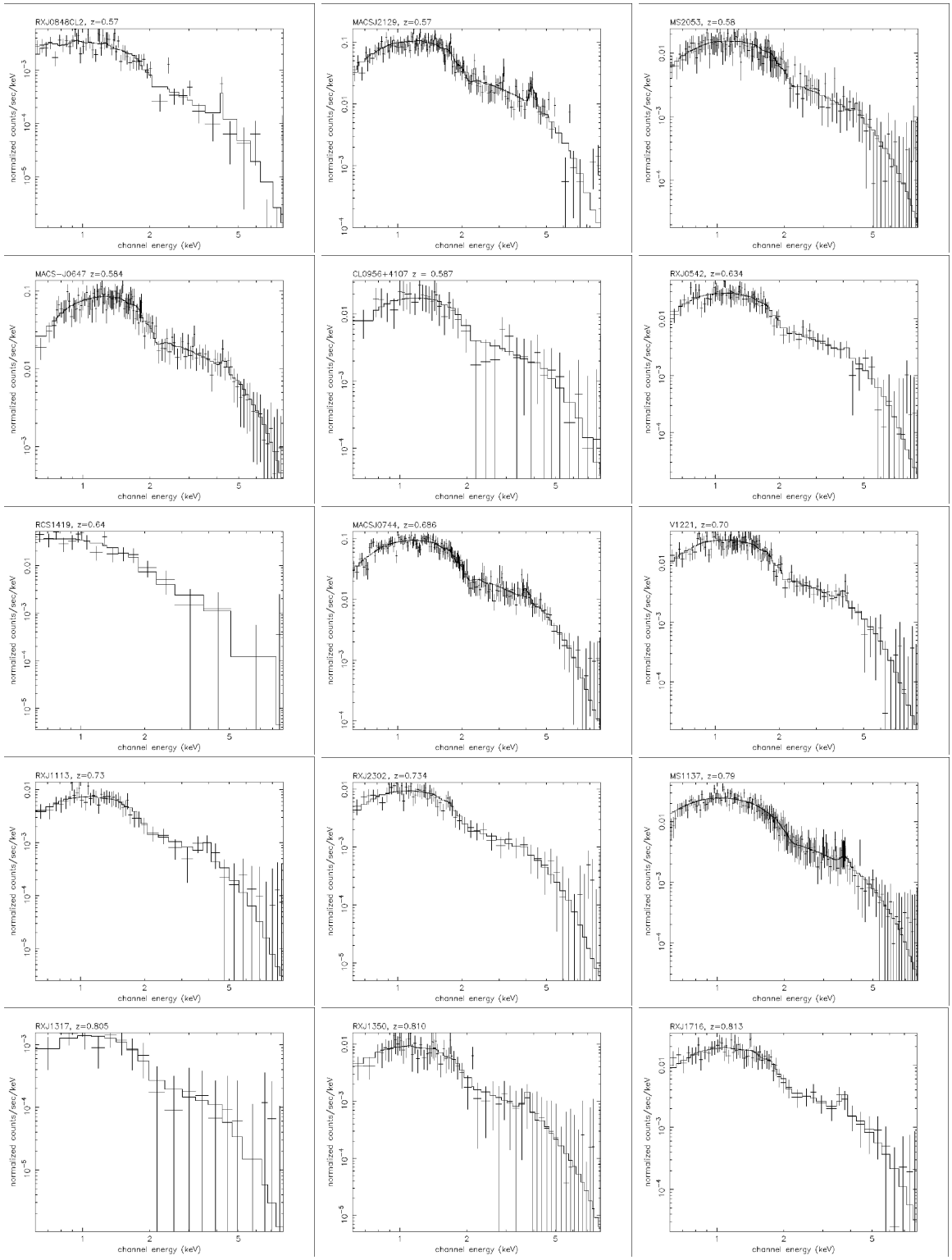

Figure C.6: Chandra spectra of the high-z cluster sample presented in Chapter 2 and best-fit obtained with the `MEKAL` model, as described in the text (see Sect. 2.3.1). The spectra have been re-binned here for illustration purposes.

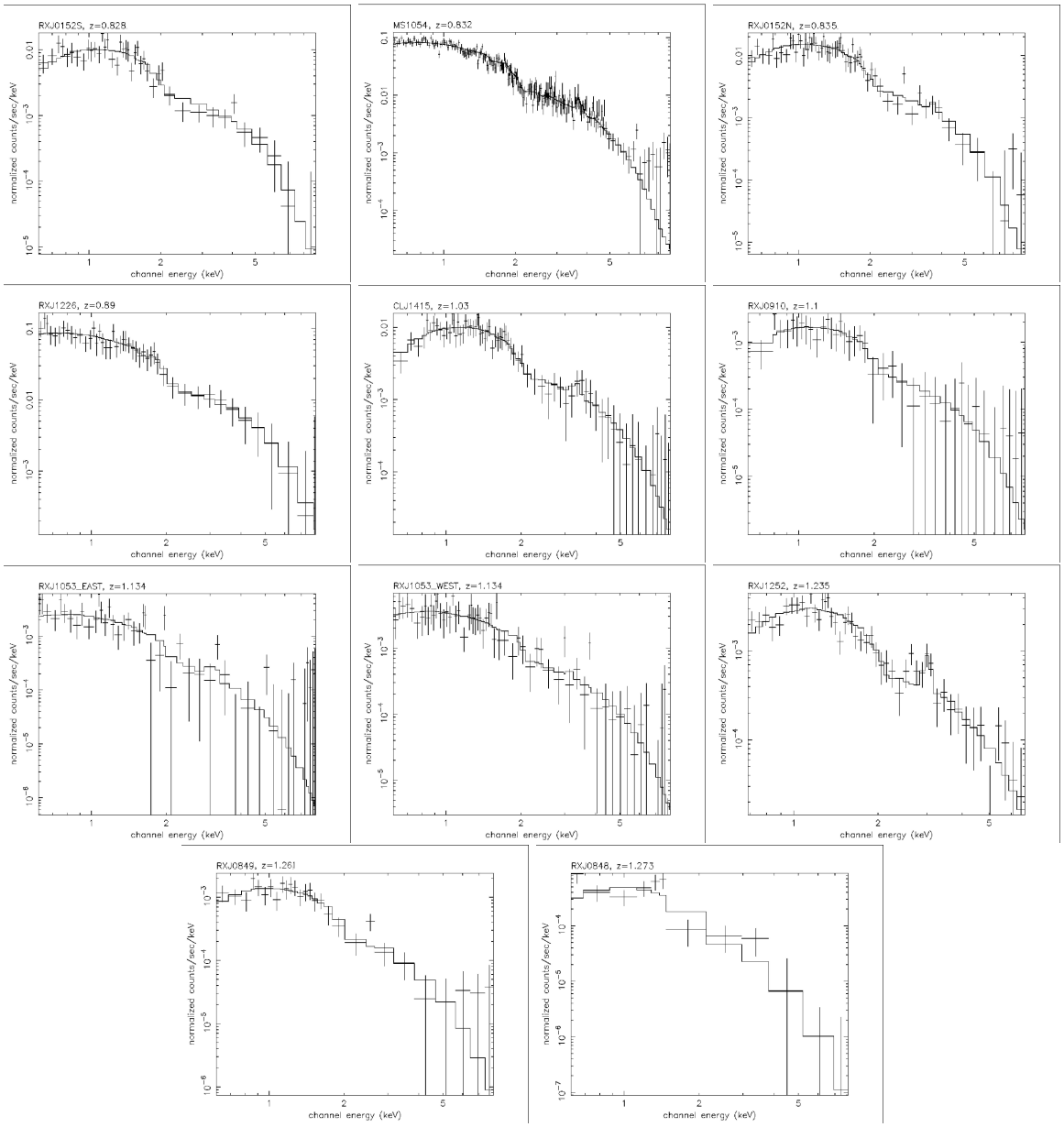

Figure C.7: Chandra spectra of the high-z cluster sample presented in Chapter 2 and best-fit obtained with the `MEKAL` model, as described in the text (see Sect. 2.3.1). The spectra have been re-binned here for illustration purposes.

Bibliography

Anders, E. & Grevesse, N. 1989, Geochim. Cosmochim. Acta, 53, 197

Andreon, S., Davoust, E., & Poulain, P. 1997, A&AS, 126, 67

Antonucci, R. 1993, ARA&A, 31, 473

Antonucci, R. R. J. & Miller, J. S. 1985, ApJ, 297, 621

Arnaud, K. A. 1996, in ASP Conf. Ser. 101: Astronomical Data Analysis Software and Systems V, ed. G. H. Jacoby & J. Barnes, 17–+

Arnaud, M. & Raymond, J. 1992, ApJ, 398, 394

Arnaud, M. & Rothenflug, R. 1985, A&AS, 60, 425

Arnaud, M., Rothenflug, R., Boulade, O., Vigroux, L., & Vangioni-Flam, E. 1992, A&A, 254, 49

Asplund, M., Grevesse, N., & Sauval, A. J. 2005, in ASP Conf. Ser. 336: Cosmic Abundances as Records of Stellar Evolution and Nucleosynthesis, ed. T. G. Barnes & F. N. Bash, 25–+

Baldi, A., Ettori, S., Mazzotta, P., Tozzi, P., & Borgani, S. 2007, ApJ, 666, 835

Balestra, I., Tozzi, P., Ettori, S., et al. 2007, A&A, 462, 429

Bar-Shalom, M., Klapisch, J., S., & Liedhal, D. 2001, Oreg. JQRST, 71, 169

Bauer, F. E., Fabian, A. C., Sanders, J. S., Allen, S. W., & Johnstone, R. M. 2005, MNRAS, 359, 1481

Baumgartner, W. H., Loewenstein, M., Horner, D. J., & Mushotzky, R. F. 2005, ApJ, 620, 680

Berrington, K. A., Eissner, W. B., & Norrington, P. H. 1994, CoPhC, 92, 290

Bianchi, S., Guainazzi, M., & Chiaberge, M. 2006, A&A, 448, 499

Biviano, A., Katgert, P., Thomas, T., & Adami, C. 2002, A&A, 387, 8

Boehringer, H. & Hensler, G. 1989, A&A, 215, 147

Boller, T., Balestra, I., & Kollatschny, W. 2007, A&A, 465, 87

Boller, T., Brandt, W. N., & Fink, H. 1996, A&A, 305, 53

Boselli, A. & Gavazzi, G. 2006, PASP, 118, 517

Brandt, W. N., Fabian, A. C., Takahashi, K., et al. 1997, MNRAS, 290, 617

Brown, G. V., Beiersdorfer, P., Liedahl, D. A., Widmann, K., & Kahn, S. M. 1998, ApJ, 502, 1015

Brown, G. V., Beiersdorfer, P., Liedahl, D. A., et al. 2002, ApJS, 140, 589

Bryan, G. L. & Norman, M. L. 1998, ApJ, 495, 80

Butcher, H. & Oemler, Jr., A. 1978, ApJ, 219, 18

Calura, F., Matteucci, F., & Tozzi, P. 2007, MNRAS, 378, L11

Chen, H., Beiersdorfer, P., Scofield, J. H., et al. 2005, ApJ, 618, 1086

Coles, P. & Lucchin, F. 1995, Cosmology. The origin and evolution of cosmic structure (Chichester, UK: Wiley)

Cora, S. A. 2006, MNRAS, 368, 1540

Croton, D. J., Farrar, G. R., Norberg, P., et al. 2005, MNRAS, 356, 1155

Dahlen, T., Strolger, L.-G., Riess, A. G., et al. 2004, ApJ, 613, 189

De Grandi, S., Ettori, S., Longhetti, M., & Molendi, S. 2004, A&A, 419, 7

de Plaa, J., Werner, N., Bleeker, J. A. M., et al. 2007, A&A, 465, 345

Dickey, J. M. & Lockman, F. J. 1990, ARA&A, 28, 215

Domainko, W., Kapferer, W., Gitti, M., et al. 2004, in Baryons in Dark Matter Halos, ed. R. Dettmar, U. Klein, & P. Salucci

Dressler, A. 1980, ApJ, 236, 351

Dressler, A., Oemler, A. J., Couch, W. J., et al. 1997, ApJ, 490, 577

Dupke, R. A. & Arnaud, K. A. 2001, ApJ, 548, 141

Elwert, G. & Naturf, Z. 1952, 7A, 432, 703

Ettori, S. 2005, MNRAS, 362, 110

Ettori, S., Tozzi, P., Borgani, S., & Rosati, P. 2004, A&A, 417, 13

Ettori, S., Tozzi, P., & Rosati, P. 2003, A&A, 398, 879

Evrard, A. E., Metzler, C. A., & Navarro, J. F. 1996, ApJ, 469, 494

Fabian, A. C. & Miniutti, G. 2005, ArXiv Astrophysics e-prints, astro-ph/0507409

Fasano, G., Poggianti, B. M., Couch, W. J., et al. 2000, ApJ, 542, 673

Ferland, G. J., Korista, K. T., Verner, D. A., et al. 1998, PASP, 110, 761

Ferrarese, L. & Merritt, D. 2000, ApJ, 539, L9

Finoguenov, A., Arnaud, M., & David, L. P. 2001, ApJ, 555, 191

Gabriel, A. H. & Jordan, C. 1969, MNRAS, 145, 241

Gal-Yam, A., Maoz, D., & Sharon, K. 2002, MNRAS, 332, 37

Gallo, L. C. 2006, MNRAS, 368, 479

Gebhardt, K., Bender, R., Bower, G., et al. 2000, ApJ, 539, L13

Gilfanov, M. R., Syunyaev, R. A., & Churazov, E. M. 1987, Soviet Astronomy Letters, 13, 3

Gondoin, P., Orr, A., Lumb, D., & Santos-Lleo, M. 2002, A&A, 388, 74

Grevesse, N. & Sauval, A. J. 1998, Space Science Reviews, 85, 161

Gu, M. F. 2003, ApJ, 582, 1241

Gu, M. F., Kahn, S. M., Savin, D. W., et al. 1999, ApJ, 518, 1002

Hamann, F. & Ferland, G. 1993, ApJ, 418, 11

Hamann, F., Korista, K. T., Ferland, G. J., Warner, C., & Baldwin, J. 2002, ApJ, 564, 592

Hashimoto, Y., Barcons, X., Böhringer, H., et al. 2004, A&A, 417, 819

Hasinger, G., Miyaji, T., & Schmidt, M. 2005, A&A, 441, 417

Heckman, T. M. 1980, A&A, 87, 152

Ho, L. C., Filippenko, A. V., & Sargent, W. L. W. 1997, ApJS, 112, 315

Holden, B. P., Stanford, S. A., Squires, G. K., et al. 2002, AJ, 124, 33

Horner, D. J. 2005, PhD Thesis (http://eud.gsfc.nasa.gov/ Donald.Horner/thesis.html)

Jordan, C. 1969, MNRAS, 142, 501

Kaastra, J. S. 1992, (Internal SRON–Leiden Report, updated version 2.0)

Kinkhabwala, A., Sako, M., Behar, E., et al. 2002, ApJ, 575, 732

Kirsch, M. 2006, http://xmm.vilspa.esa.es/docs/documents/CAL-TN-0018.pdf+

Kuntschner, H., Smith, R. J., Colless, M., et al. 2002, MNRAS, 337, 172

Larson, R. B., Tinsley, B. M., & Caldwell, C. N. 1980, ApJ, 237, 692

Leighly, K. M. 1999a, ApJS, 125, 297

Leighly, K. M. 1999b, ApJS, 125, 317

Liedahl, D. A., Osterheld, A. L., & Goldstein, W. H. 1995, ApJ, 438, L115

Lin, Y.-T., Mohr, J. J., & Stanford, S. A. 2003, ApJ, 591, 749

Loewenstein, M. 2006, ApJ, 648, 230

Lu, L., Sargent, W. L. W., Barlow, T. A., Churchill, C. W., & Vogt, S. S. 1996, ApJS, 107, 475

Mannucci, F., Della Valle, M., & Panagia, N. 2006, MNRAS, 370, 773

Mannucci, F., Della Valle, M., Panagia, N., et al. 2005, A&A, 433, 807

Marshall, H. L., Tennant, A., Grant, C. E., et al. 2004, in X-Ray and Gamma-Ray Instrumentation for Astronomy XIII. Proceedings of the SPIE, ed. K. A. Flanagan & O. H. W. Siegmund, Vol. 5165, 497–508

Mathur, S. 2000, MNRAS, 314, L17

Matteucci, F. & Recchi, S. 2001, ApJ, 558, 351

Matteucci, F. & Vettolani, G. 1988, A&A, 202, 21

Maughan, B. J., Jones, C., Forman, W., & Van Speybroeck, L. 2007, ArXiv Astrophysics e-prints, astro-ph/0703156

Maughan, B. J., Jones, L. R., Ebeling, H., & Scharf, C. 2004, MNRAS, 351, 1193

Maughan, B. J., Jones, L. R., Ebeling, H., & Scharf, C. 2006, MNRAS, 365, 509

Mazzotta, P., Mazzitelli, G., Colafrancesco, S., & Vittorio, N. 1998, A&AS, 133, 403

Mazzotta, P., Rasia, E., Moscardini, L., & Tormen, G. 2004, MNRAS, 354, 10

Mewe, R. 1999, in van Paradijs, Bleeker Eds., X-ray spectroscopy in Astrophysics, Springer, Berlin

Mewe, R., Gronenschild, E. H. B. M., & van den Oord, G. H. J. 1985, A&AS, 62, 197

Mewe, R., Kaastra, J., S., & Liedhal, D. 1995, Legacy Suppl., 6, 16

Mewe, R., Lemen, J. R., & van den Oord, G. H. J. 1986, A&AS, 65, 511

Miller, J. S. & Antonucci, R. R. J. 1983, ApJ, 271, L7

Murante, G., Arnaboldi, M., Gerhard, O., et al. 2004, ApJ, 607, L83

Mushotzky, R. F. & Loewenstein, M. 1997, ApJ, 481, L63+

Nomoto, K., Iwamoto, K., Nakasato, N., et al. 1997, Nuclear Physics A, 621, 467

Nousek, J. A. & Shue, D. R. 1989, ApJ, 342, 1207

Peacock, J. A. 1999, Cosmological Physics (Cambridge, UK: Cambridge University Press)

Peebles, P. J. E. 1993, Principles of physical cosmology (Princeton, NJ: Princeton University Press)

Peterson, J. R. & Fabian, A. C. 2006, to appear in Physics Report (astro-ph/0512549), 427, 1

Peterson, J. R., Kahn, S. M., Paerels, F. B. S., et al. 2003, ApJ, 590, 207

Pettini, M., Smith, L. J., King, D. L., & Hunstead, R. W. 1997, ApJ, 486, 665

Pipino, A., Matteucci, F., Borgani, S., & Biviano, A. 2002, New Astronomy, 7, 227

Poggianti, B. M., Smail, I., Dressler, A., et al. 1999, ApJ, 518, 576

Pounds, K. A., Done, C., & Osborne, J. P. 1995, MNRAS, 277, L5

Pratt, G. W., Arnaud, M., & Pointecouteau, E. 2006, A&A, 446, 429

Prochaska, J. X., Wolfe, A. M., Tytler, D., et al. 2001, ApJS, 137, 21

Raymond, J. C. & Smith, B. W. 1977, ApJS, 35, 419

Renzini, A. 1997, ApJ, 488, 35

Romeo, A. D., Portinari, L., & Sommer-Larsen, J. 2005, MNRAS, 361, 983

Rosati, P., Borgani, S., & Norman, C. 2002, ARA&A, 40, 539

Rosati, P., Tozzi, P., Ettori, S., et al. 2004, AJ, 127, 230

Sako, M., Kahn, S. M., Paerels, F., & Liedahl, D. A. 2000, ApJ, 543, L115

Sanders, J. S., Fabian, A. C., Allen, S. W., & Schmidt, R. W. 2004, MNRAS, 349, 952

Satyapal, S., Dudik, R. P., O'Halloran, B., & Gliozzi, M. 2005, ApJ, 633, 86

Savaglio, S. 2006, New Journal of Physics, 8, 195

Schindler, S., Kapferer, W., Domainko, W., et al. 2005, A&A, 435, L25

Sharon, K., Gal-Yam, A., Maoz, D., Filippenko, A. V., & Guhathakurta, P. 2007, ApJ, 660, 1165

Shemmer, O. & Netzer, H. 2002, ApJ, 567, L19

Shemmer, O., Netzer, H., Maiolino, R., et al. 2004, ApJ, 614, 547

Shields, G. A. 1976, ApJ, 204, 330

Smith, R. K., Brickhouse, N. S., Liedahl, D. A., & Raymond, J. C. 2001, ApJ, 556, L91

Stauffer, J. R. 1982, ApJ, 262, 66

Steidel, C. C., Adelberger, K. L., Giavalisco, M., Dickinson, M., & Pettini, M. 1999, ApJ, 519, 1

Steidel, C. C., Adelberger, K. L., Shapley, A. E., et al. 2005, ApJ, 626, 44

Sutherland, R. S. & Dopita, M. A. 1993, ApJS, 88, 253

Tamura, T., Kaastra, J. S., den Herder, J. W. A., Bleeker, J. A. M., & Peterson, J. R. 2004, A&A, 420, 135

Tornatore, L., Borgani, S., Matteucci, F., Recchi, S., & Tozzi, P. 2004, MNRAS, 349, L19

Tozzi, P., Rosati, P., Ettori, S., et al. 2003, ApJ, 593, 705

Trager, S. C., Faber, S. M., Worthey, G., & González, J. J. 2000, AJ, 120, 165

Tran, K.-V. H., van Dokkum, P., Illingworth, G. D., et al. 2005, ApJ, 619, 134

Ueda, Y., Akiyama, M., Ohta, K., & Miyaji, T. 2003, ApJ, 598, 886

Valdarnini, R. 2003, MNRAS, 339, 1117

van Dokkum, P. G., Franx, M., Fabricant, D., Illingworth, G. D., & Kelson, D. D. 2000, ApJ, 541, 95

Vaughan, S., Reeves, J., Warwick, R., & Edelson, R. 1999, MNRAS, 309, 113

Vikhlinin, A., Markevitch, M., Murray, S. S., et al. 2005, ApJ, 628, 655

Vikhlinin, A., Van Speybroeck, L., Markevitch, M., Forman, W. R., & Grego, L. 2002, ApJ, 578, L107

Voit, G. M. 2005, Reviews of Modern Physics, 77, 207

Wilms, J., Allen, A., & McCray, R. 2000, ApJ, 542, 914

Woosley, S. E. & Weaver, T. A. 1995, ApJS, 101, 181

Zhang, Y.-Y., Böhringer, H., Mellier, Y., Soucail, G., & Forman, W. 2005, A&A, 429, 85